UNIVERSITY OF ALBERTA

ELECTROPLATING OF GOLD-TIN EUTECTIC SOLER

by

Wenzhen Sun ©

A thesis submitted to the Faculty of Graduate Studies and Research in partial fulfillment of the requirement for the degree of Master of Science

in

MATERIALS ENGINEERING

DEPARTMENT OF CHEMICAL AND MATERIALS ENGINEERING

EDMONTON, ALBERTA, CANADA

Fall, 1998

National Library of Canada
Acquisitions and Bibliographic Services
395 Wellington Street
Ottawa ON K1A 0N4
Canada

Bibliothèque nationale du Canada
Acquisitions et services bibliographiques
395, rue Wellington
Ottawa ON K1A 0N4
Canada

Your file Votre référence

Our file Notre référence

The author has granted a non-exclusive licence allowing the National Library of Canada to reproduce, loan, distribute or sell copies of this thesis in microform, paper or electronic formats.

The author retains ownership of the copyright in this thesis. Neither the thesis nor substantial extracts from it may be printed or otherwise reproduced without the author's permission.

L'auteur a accordé une licence non exclusive permettant à la Bibliothèque nationale du Canada de reproduire, prêter, distribuer ou vendre des copies de cette thèse sous la forme de microfiche/film, de reproduction sur papier ou sur format électronique.

L'auteur conserve la propriété du droit d'auteur qui protège cette thèse. Ni la thèse ni des extraits substantiels de celle-ci ne doivent être imprimés ou autrement reproduits sans son autorisation.

0-612-47158-6

Canada

UNIVERSITY OF ALBERTA

Library Release Form

NAME OF AUTHOR: **WENZHEN SUN**

TITLE OF THESIS: **Electroplating of Gold-Tin Eutectic Solder**

DEGREE: **Master of Science**

YEAR THIS DEGREE GRANTED: **1998**

Permission is hereby granted to the University of Alberta Library to reproduce single copies of this thesis and to lend or sell such copies for private, scholarly, or scientific research purposes only.

The author reserves all other publication and other rights in association with the copyright in the thesis, and except as hereinbefore provided, neither the thesis nor any substantial portion thereof may be printed or otherwise reproduced in any material form whatever without the author's prior written permission.

Wenzhen Sun

Wenzhen Sun
c/o. Mr. Jianzhuo Sun
Tong Ji Ju Building, Yanhe Street
Xiaogan, Hubei
P. R. China 432100

Date: Sept. 22, 1998

UNIVERSITY OF ALBERTA

FACULTY OF GRADUATE STUDIES AND RESEARCH

The undersigned certify that they have read, and recommend to the Faculty of Graduate Studies and Research for acceptance, a thesis entitled **ELECTROPLATING OF GOLD-TIN EUTECTIC SOLDER** submitted by **WENZHEN SUN** in partial fulfillment of the requirements for the degree of **MASTER OF SCIENCE** in **MATERIALS ENGINEERING**.

Dr. D. G. Ivey, Supervisor

Dr. J. L. Luo

Dr. A.M. Robinson

DATE: Sept. 15/98

Abstract

Au-Sn eutectic solder, 70at%Au-30at%Sn, has excellent mechanical and thermal properties, which is especially ideal for flip chip techniques and laser bonding in optoelectronic applications. Currently Au-Sn solders are deposited by thin film technologies, which involve expensive equipment. Au-Sn preforms are also commonly used, which are problematic in terms of handling and alignment have poor thickness and bonding area control. This project aimed at developing a cost-effective Au-Sn solder electroplating process. The two main challenges of developing a non-cyanide Au-Sn alloy plating bath are to obtain good bath stability and deposit composition control.

A relatively stable non-cyanide neutral electroplating bath of Au-Sn alloy is developed using gold and tin chloride salts and ammonium citrate as a buffering agent. The effects of the selected chemicals on the bath stability and polarization behavior of the bath are examined. A study on corrosion behavior of InP and GaAs wafers in the developed solutions is also conducted. Pulse current (PC) plating and direct current (DC) plating are performed and compared according to their effects. A detailed investigation on the effects of several PC plating parameters, e.g., ON time, OFF time, and several electrolyte parameters, such as the ratio of Au-Sn content in the bath and total Au-Sn content in the bath, on deposit composition, microstructures, and phase structures. Other tests performed in the project include annealing tests and reproducibility tests.

Acknowledgments

I am deeply indebted to Dr. Douglas Ivey for his supervision, guidance, and encouragement extended throughout my research at University of Alberta.

It is a great pleasure to acknowledge Dr. Jingli Luo for access to electrochemical testing equipment and Dr. D. Joy for providing Monte Carlo simulation software.

Special thanks are extended to Tina Barker and George D Braybrook for SEM analysis, Dr. R. Chi for AFM analysis, Bob Konzuk for designing and making sample holder, and Merali Shiraz for XRD analysis.

I wish to thank Qi Yang, Yufeng Cheng, Ning Cui, and Lijie Qiao for their advice and cooperation in electrochemical measurement.

Thanks most certainly go to everyone in our group for their valuable discussions. The help of Udit Sharma in preparing the plots is greatly appreciated.

Finally, I wish to acknowledge Nortel technology and Natural Science and Engineering Council of Canada for funding this work.

Table of Contents

1.	***Introduction***		1
2.	***Literature Review***		3
2.1	Literature Review		3
	2.1.1	Application of Au-Sn solder in electronic and optoelectronic packaging	3
	2.1.2	Au-Sn metallurgy	4
		2.1.2.1 Au-Sn phase diagram	4
		2.1.2.2 Wetting, oxidation and segregation	5
	2.1.3	Diffusion behavior of Au and Sn	7
	2.1.4	Metallization systems compatible with Au-Sn solder	8
	2.1.5	Fabrication techniques	11
	2.1.6	Bonding using Au-Sn metallurgy	13
		2.1.6.1 Bonding techniques	13
		Reflow-soldering with infrared heating	13
		Pulse heated thermode	13
		Vapor phase reflow	14
		Laser bonding	14
		Low temperature diffusion bonding	14
		2.1.6.2 Evaluation of bonding quality	15
	2.1.7	Problems in application of Au-Sn alloy	16
	2.1.8	Electroplating of Au-Sn solder	17
		2.1.8.1 Sequential electroplating of Au-Sn solders	18
		2.1.8.2 Electroplating of Au-Sn alloy	22
		Cyanide system	23
		Chloride system	24
		Sulfite system	25
2.2	Theory of Electroplating		25

2.2.1 Electroplating of a single metal 25
Electrode reaction 25
Deposition rate and current efficiency 27
Overpotential 27
Electrocrystallization 30
Underpotential plating 31
Current distribution near the cathode 32
2.2.2 Electroplating of metal alloys 36
2.2.3 Pulse plating 39
2.2.3.1 Pulse plating of a single metal 39
Charging and discharging of electrical double layer 39
Mass transport 40
Pulse-limiting current density 41
2.2.3.2 Periodic reverse-current plating (PRC) 42

3. Bath Stability 67
3.1 Introduction 67
3.2 Experimental Methods 69
3.2.1 Solution preparation 69
Starting solutions 69
Preliminary screening test with several non-cyanide stabilizers 69
Bath stability test for various solutions 70
3.2.2 Polarization behavior of the solutions 70
3.2.3 Causticity test of wafers 70
3.3 Results and Discussion 71
3.3.1 Solution preparation 71
Starting solutions 71
Preliminary screening test with several non-cyanide stabilizers 73
Bath stability test for various solutions 75
3.3.2 Polarization behavior 77
3.3.3 Causticity test of wafers 81

3.4 Conclusions 82

4. Electroplating 94

4.1 Introduction 94

4.2 Experimental Methods 98

4.2.1 DC and PC plating 99

4.2.2 Effect of ON time 100

4.2.2.1 Effect of ON time at constant average current density and cycle Period 100

4.2.2.2 Effect of ON time at constant peak current density and OFF time 100

4.2.3 Effect of OFF time 100

4.2.4 Effect of various electrolyte parameters 101

4.3 Results and Discussion 101

4.3.1 DC and PC plating 101

4.3.2 Effect of ON time 105

4.3.2.1 Effect of ON time at constant average current density and cycle period 105

4.3.2.2 Effect of ON time at constant peak current density and OFF time 106

Estimation of current efficiency 106

Composition 108

Microstructure 109

Phase analysis 110

4.3.3 Effect of OFF time 111

Composition 111

Microstructure 112

Phase analysis 113

4.3.4 Effect of various electrolyte parameters 115

4.4. Conclusions 115

5. Annealing Tests and Reproducibility Test 143
5.1 Introduction 143
5.2 Experimental Methods 143
5.2.1 Annealing tests 143
5.2.2 Reproducibility test 144
5.2.2.1 Reproducibility test (I) 144
5.2.2.2 Reproducibility test (II) 144
5.3 Results and Discussion 145
5.3.1 Annealing tests 145
5.3.1.1 Microstructure 145
5.3.1.2 Phase analysis 145
5.3.2 Reproducibility test 146
5.3.2.1 Reproducibility test (I) 146
5.3.2.2 Reproducibility test (II) 147
5.4 Conclusions 150

6. Conclusions and Recommendations 166
6.1 Conclusions 166
6.2 Recommendations 168

References 169

Appendix A: Selected X-ray Diffraction Data for Au, Au_5Sn, AuSn, $AuSn_2$, $AuSn_4$, Sn, InP, Si, Ti, and Mo 176

List of Tables

Table 2.1	Properties of several solder materials [Tan 96].	44
Table 2.2	An overview of the basic difference between several bonding technologies [Kallmayer 95].	44
Table 2.3	Stability constant β_2 and β_4 for gold (I) complexes and gold (III) complexes, respectively [Stanley 87].	45
Table 2.4	An alkaline Au sulfite plating bath [Gemmler 94].	45
Table 2.5	The basic composition and operating conditions of a gold(I) thiosulfate-sulfite bath [Osaka 97].	46
Table 2.6	Solution and plating conditions of an acidic cyanide gold-tin plating Bath [Kuhn 95].	46
Table 2.7	Standard reduction potentials for various reactions involving gold [Stanley 87].	47
Table 3.1	Solution preparation.	83
Table 3.2	Screening test of stabilizer candidates.	84
Table 3.3	Solutions utilized for bath stability tests.	85
Table 3.4	Solutions utilized to test polarization curves.	86
Table 3.5	Causticity test of InP and GaAs wafers in solution.	87
Table 4.1	Solutions and plating conditions utilized for DC and PC plating.	117
Table 4.2	Solutions and pulse plating parameters used in Series 1.	118
Table 4.3	Solutions and pulse plating parameters used in Series 2.	118
Table 4.4	Deposit composition and thickness results at different ON times.	119
Table 4.5	Deposit composition at different OFF times.	119
Table 5.1	Compositional depth profile results for 4 different locations in reproducibility test (II).	152
Table 5.2	Results for Monte Carlo simulations.	152

List of Figures

Fig. 2.1	Au-Sn eutectic solder for InP laser bonding [Ivey 98].	48
Fig. 2.2	Au-Sn phase diagram (a) and (b) Au-rich portion of the Au-Sn diagram [Matijasevic 93].	49
Fig. 2.3	A Schematic presentation of the conceptual design of a bonded device [Katz 94-1].	51
Fig. 2.4	Schematic of intermetallic compound formation and Kirkendall void formation in Au-Sn solder [Zakel 95-2].	51
Fig. 2.5	Binary phase diagram of Pt-Au (a) and Pt-Sn (b) [Katz 94-1].	52
Fig. 2.6	(a) Au-Ni, (b) Ni-Sn, (c) Au-Cr, (d) Cr-Sn, and (e) Au-W phase diagram [Katz 94-1].	53
Fig. 2.7	Flow chart of bumping process by sequential electroplating of Au-Sn [Kallmayer 95-1].	55
Fig. 2.8	Schematic showing vapor phase reflow [Kallmayer 95-1].	56
Fig. 2.9	Schematic of laser bonding [Azdasht 94].	56
Fig. 2.10	Schematic of low temperature diffusion bonding [Lee 92-1].	57
Fig. 2.11	The principal components of an electroplating process [Pletcher 90].	57
Fig. 2.12	Plot of log lil vs. η.	58
Fig. 2.13	A general qualitative description of the relationship between current density and potential. Line **a** is the purely activation-controlled current I_{ac}, line **b** is the actual current which will be measured, having a mass-transport-limited value I_L [Gileadi 93].	58
Fig. 2.14	Microstructure dependence on current density.	59
Fig. 2.15	Underpotential deposition of lead on gold from a solution of 1.0 mM $Pb(ClO_4)_2$ in 1.0 M $HClO_4$. Two underpotential deposition (UPD) and dissolution peaks are shown [Gileadi 93].	59
Fig. 2.16	Equivalent circuit for a two-electrode cell. A single interface is usually represented by the elements inside the dashed	

rectangle. C_{dl}, R_F and R_S represent the double-layer capacitance, the faradaic resistance and the solution resistance, respctively. 60

Fig. 2.17 Influence of diffusion layer thickness on tertiary current distribution. (a) Microprofile: the crests are privileged from the point of view of diffusion; (b) Macroprofile: the current density is uniformly distributed [Puipe 86]. 60

Fig. 2.18 Haring and Blum cell for throwing power testing. 61

Fig. 2.19 Microthrowing power and leveling. (a) Poor microthrowing power; (b) Geometric microthrowing power; (c) True leveling [Tan 93]. 61

Fig. 2.20 Evans diagrams representing the partial currents of alloy components A and B for anomalous codeposition of a binary alloy AB. $E_{rev,A}$ and $E_{rev,B}$ represent the equilibrium potentials of the components. Figures (a) and (b): both partial reactions are charge transfer controlled. Figures (c) and (d): one of the partial reactions is mass transport controlled. The hashed area represents the potential range leading to referential deposition of the less noble component A [Landolt 94]. 62

Fig. 2.21 Schematic presentation of partial anodic and cathodic currents for Cu and Ni and of the total cathodic current during deposition of a Ni-Cu alloy from an electrolyte containing a high Ni and a low Cu concentration [Landolt 94]. 63

Fig. 2.22 Schematic representation and suggested nomenclature for some square-wave-modulated current systems, and definition of related parameters. (a) Pulse, (b) Superimposed pulse, (c) Duplex pulse, (d) Pulsed pulse, (e) Pulse-on-pulse, (f) Pulse reverse, (g) Pulse reverse (with OFF time), (h) Pulsed pulse reverse, (i) Pulse-on-pulse reverse [Puipe 86]. 64

Fig. 2.23 Schematic concentration profiles at the cathode upon

application of (a) a constant current step and (b) a constant potential step [Puipe 86]. 65

Fig. 2.24 Concentration profiles of the two diffusion layers on pulse electrolysis at the end of a pulse. δ_p is the thickness of the pulsating diffusion layer; δ_S is the thickness of the stationary diffusion layer. 66

Fig. 3.1 Cathodic polarization curves for Solutions (a) SAu-1, (b) SAu-2, (c) SAu-3, (d) SAu-4, (e) SAu-5, (f) SAu-6, and (g) SAu-7. The dashed line indicates the approximate potentials of hydrogen evolution. 88

Fig. 3.2 Cathodic polarization curves for Solutions (a) SSn-1, (b) SSn-2, and (c) SSn-3. The dashed lines H_1 and H_2 show the approximate potentials for hydrogen evolution on curve (a), and on curves (b) and (c), respectively. 89

Fig. 3.3 Cathodic polarization curves for Solutions (a) SSn-3, (b) SSn-4, (c) SSn-5, (d) SSn-6, (e) SSn-7, and (f) SSn-8. The dashed line indicates the approximate potentials of hydrogen evolution. 90

Fig. 3.4 Cathodic polarization curves for Solutions (a) Au-Sn (b) SAu-4, and (c) SSn-5. Curve (d) is the sum of curves (b) and (c). The dashed line indicates the approximate potentials of hydrogen evolution for curve (a). 91

Fig. 3.5 AFM images of InP wafer surface before (a) and after (b) the causticity test in Solution S6 92

Fig. 3.6 AFM images of GaAs wafer surface before (a) and after (b) the causticity test in Solution S6. 93

Fig. 4.1 Electroplating setup. 120

Fig. 4.2 Sn content in deposit vs. average current density for DC (a) and PC (b) plating in Solution S4-1. The ON time and OFF time for PC plating are 2 ms and 8 ms, respectively. The error bar corresponds to the standard deviation in the composition

measurements at three different locations for each sample. 120

Fig. 4.3 SEM top view images for PC plated deposits (a-c) and DC plated deposits (d-f). The ON time and OFF time for PC plating are 2 ms and 8 ms, respectively. 121

Fig. 4.4 Edge effects (SEM) in PC plating at current densities of 2.0, 2.8 and 3.2 mA/cm^2. The ON time and OFF time are 2 ms and 8 ms, respectively. 122

Fig. 4.5 Effect of ON time in PC plating on deposit composition at the constant average current density of 2.4 mA/cm^2 and cycle period of 10 ms. The error bar corresponds to the standard deviation in the composition measurements at three different locations for each sample. 123

Fig. 4.6 SEM images for PC deposits at various ON times at the constant average current density of 2.4 mA/cm^2 and cycle period of 10 ms. 124

Fig. 4.7 Three-dimensional AFM images for PC deposits at various ON times at the constant average current density of 2.4 mA/cm^2 and cycle period of 10 ms. 125

Fig. 4.8 The effect of ON time on deposit composition at constant peak current density of 10 mA/cm^2 and OFF time of 8 ms. The error bar corresponds to the standard deviation in the composition measurements at three different locations for each sample. 127

Fig. 4.9 SEM top views of the deposits obtained at ON times of 1, 2, 3,and 4 ms at constant peak current density of 10 mA/cm^2 and OFF time of 8 ms. 128

Fig. 4.10 Cleaved cross-section images of the deposits obtained at different ON times at constant peak current density of 10 mA/cm^2 and OFF time of 8 ms. 129

Fig. 4.11 XRD spectra for the deposits obtained at (a) 0.5, (b) 1, (c) 2, (d) 3, and (e) 4 ms ON times at constant peak current density of 10 mA/cm^2 and OFF time of 8 ms. 130

Fig. 4.12 Deposit composition at different OFF times while the peak current

density is constant at 10 mA/cm^2 and ON time at 2 ms. The error bar corresponds to the standard deviation in the composition measurements at three different locations for each sample. 135

Fig. 4.13 SEM top view images of the deposits obtained at different OFF times while the peak current density is kept constant at 10 mA/cm^2 and the ON time at 2 ms. 136

Fig. 4.14 Cleaved cross section images of the deposits obtained at OFF times of 9.9 ms and 4 ms while the peak current density is kept constant at 10 mA/cm^2 and ON time at 2 ms. 137

Fig. 4.15 XRD spectra for the deposits obtained at OFF times of (a) 8, (b) 6, (c) 4, and (d) 3 ms. 138

Fig. 4.16 Effect of ratio of gold to tin salt content in bath on deposit composition at 1ms of ON time and 9ms of OFF time. R is the content ratio of gold to tin salts. The error bar corresponds to the standard deviation in the composition measurements at three different locations for each sample. 142

Fig. 4.17 Deposit composition curves vs. average current density for selected Solutions at 2ms of ON time and 8ms of OFF time. The value shown in the parentheses is the ratio of gold to tin salt content. The error bar corresponds to the standard deviation in the composition measurements at three different locations for each sample. 142

Fig. 5.1 SE images of the annealed sample at 350°C for 2 min. 153

Fig. 5.2 BSE images of the annealed sample at 350°C for 2 min. 154

Fig. 5.3 Representative EDX spectra for (a) overall sample, (b) light contrast areas, (c) dark contrast areas and (d) eutectic areas of a sample annealed at 350°C for 2 min. 155

Fig. 5.4 XRD spectra of (a) as-deposited sample, (b) sample annealed at 350°C for 2 min, and (c) InP wafer with 25nm Mo/25nm Au metallization. 156

Fig. 5.5 TEM cross section image (a) of the annealed deposit at 350°C for 2

	min and EDX spectra for the Au5Sn (b) and AuSn phases (c).	159
Fig. 5.6	The deposit composition vs. plated area for the sample in Reproducibility Test (I). The error bar corresponds to the standard deviation in the composition measurements at three different locations for each sample.	160
Fig. 5.7	SEM top views of the deposit in Reproducibility test (II).	161
Fig. 5.8	FESEM images of (a) polished and (b), (c) and (d) cleaved cross section images of the deposit in Reproducibility Test (II). The arrow in (d) shows the spot of delamination.	162
Fig. 5.9	BSE images of several selected polished cross section segments of the deposit in Reproducibility Test (II). The InP substrate is to the right of the deposit.	163
Fig. 5.10	Locations of 4 compositional depth profiles in the polished cross section of the deposit for Reproducibility Test (II). The InP substrate is to the left of the deposit.	164
Fig. 5.11	Composition vs. distance from the deposit-wafer interface for the sample regions shown in Fig. 5.10. The error bar is the statistical error of Sn content in EDS analysis.	165

Abbreviations

AAS	Atomic absorption spectroscopy
AC	Alternating current
AES	Auger electron spectroscopy
AFM	Atomic force microscopy
CTE	Coefficient of thermal expansion
DC	Direct current
DPP	Differential pulse polarography
DSC	Differential scanning calorimetry
EDS	Energy dispersive x-ray spectroscopy
FESEM	Field Emission scanning electron microscopy
IC	Ion chromatography
ICP	Inductively coupled plasma emission spectroscopy
ILB	Inner lead bonding
OEP	Optoelectronic packaging
OLB	Outer lead bonding
PC	Pulsed current
PRC	Periodic reverse current plating
RBS	Rutherford backscattered spectroscopy
RDE	Rotating Disc electrode
SCE	Standard Calomel Electrode
SAM	Scanning acoustic microscopy
SCE	Saturated calomel electrode
SEM	Scanning electron microscopy
SMT	Surface mounting technology
TEM	Transmission electron microscopy
TAB	Tape automated bonding
UPD	Underpotential deposition
XRD	X-ray diffraction

Symbols

a	activity
A	molar mass
C	capacitance
C^0	bulk concentration
CE	current efficiency
D	diffusion coefficient
E	electrode potential
E^0	standard electrode potential
E_a, E_c	the equilibrium potentials for the anode and cathode
E_e	equilibrium electrode potential
$E_{rev,A}$, $E_{rev,B}$	equilibrium electrode potential for two species A and B
$f(x,y)$	the height of the surface relative to the center plane
F	faradaic constant
g_{Au}	the total weight of gold in bath
H	height of the solder joint
i	current density
i_0	exchange current density
i_{ac}	the current density under activation control
i_A, i_B	the cathodic partial current density for two species A and B
$i_{0,A}$, $i_{0,B}$	the exchange current density for two species A and B
i_C	the charging current density
i_F	the faradaic current density
i_L	limiting current density
i_{Lm}	the average limiting current density in pulse plating
i_{LP}	limiting peak current density
i_p	peak current density
i_t	total current density
k_0	a constant
K	ratio of distances between the anode and the two cathodes

L	distance between the solder joint and the newtral point of the assembly
L_x, L_y	the dimensions of the surface in x and y direction
n	the number of the electrons transferred in an electrode reaction
M	the ratio of coating thickness on the two cathodes
N_f	fatigue life for a solder joint
Q_{Sn}, Q_{Au}	the charge used for Sn plating and Au plating, respectively
R	gas constant
R_0	a constant
R_a	a resistance
R_a	the mean roughness
R_{cell}	the internal resistance of the cell
R_S	the resistance of the electrolyte
R_p, R_p'	polarization resistance
S	sample area
$s_{c,j}$	the inverse of the cathodic Tafel coefficient for component j
T	temperature
ΔT	range of the temperature
t	time
t_c^*	the charging time assuming that the entire current is capacitive until the double layer is charged
t_c^{**}	the charging time needed to increase the overpotential to 98.2 percent of $\eta_{a,\infty}$
t_{ON}, t_{OFF}	pulse time and OFF time
T.P.	throwing power
V	volume
w	the angular rotation rate of the electrode
Wa	the Wagner number
x	deposit thickness
α_1, α_2	coefficient of thermal expansion (CTE) of the component and the substrate
β	symmetry factor for a single-step electrode reaction
β	stability constant

β_2, β_4	stability constant for gold (I) complexes and gold (III) complexes
δ	the intermetallic compound: AuSn
δ	Nernst diffusion layer thickness
δp	the thickness of the pulsating diffusion layer
ϕ	cathode current efficiency
γ	duty cycle
η	overpotential
η_a	the cathodic overpotential under activation control
$\eta_{a,\infty}$	steady state overpotential
η_c	concentration overpotential
θ	the fractional surface coverage by molecules of the additives
ρ	mass density (g/cm^3)
Δv	shear strain
ν	the kinematic viscosity (= viscosity/density)
τ	transition time
ζ	the gold rich phase with composition extending from 9.1at%Sn to 17.6at% Sn

Chapter 1

Introduction

Au-Sn eutectic solder has excellent mechanical and thermal properties compared with the traditional Pb-Sn solder used in electronic and optoelectronic packaging. It is especially ideal for flip chip techniques and laser bonding in optoelectronic applications. However, it has a very high application cost, including material cost (because Au is a precious metal) and fabrication cost (because Au-Sn eutectic solder is mainly deposited by thin film technology). Metallurgical gold-tin preforms is another commonly used method of fabricating gold-tin solder. Preforms are problematic in terms of handling and alignment and become impractical for fine-pitch and flip chip applications because of poor thickness and bonding area control. Other fabrication methods include solder pastes, which are subject to oxidation and contamination by organic residue. Au-Sn solder is only used under certain situations where the performance and reliability of electronic devices are extremely critical, for example, for military purposes. Lowering cost and improving performance are two continuing themes in new materials application. The objective of the work in this thesis is to investigate the feasibility of electroplating gold-tin solder for microelectronic and optoelectronic application.

The feasibility of electroplating Au-Sn solder is studied based on two considerations. One of these is cost, i.e., compared with thin film technology utilized to deposit Au-Sn solder, electroplating is much cheaper. The other consideration aims at improving bond quality. Currently, Au-Sn solders obtained by the existing techniques have multilayered structures. It is believed that Au-Sn solder obtained by alloy electroplating may be able to minimize the voiding problem which usually occurs in bonding layers using multilayered Au-Sn solders.

The investigational and applicational studies of electroplating Au-Sn alloy described in this thesis include developing a relatively stable plating bath and finding optimum plating conditions. Gold cyanide complex is the most stable complex and most of the gold or gold alloy plating baths are cyanide-based systems. However, it is well known

that cyanide is extremely toxic and environmentally unfavorable. Therefore, this thesis aimed at developing a non-cyanide plating bath, a challenge of improving bath stability. The value of melting point of solders is one of the most important parameters for solders. Because of the steep liquidius line at the Au-rich side of the eutectic point, a small shift in composition from the eutectic point will result in a significant increase in the melting point of the electrodeposited solder. Therefore the compositional control of electrodeposits is another challenge for solder alloy electroplating.

The thesis is divided into 6 chapters. A non-cyanide neutral electroplating bath of Au-Sn alloy is developed in Chapter 3 using chloride gold and tin salts and ammonium citrate as a buffering agent. The effects of the chemicals on the bath stability are examined. It is found that sodium sulfite can effectively extend bath lifetime. The polarization behavior of the developed plating bath is examined to understand the role of the stabilizers and to find the proper range of working current densities. Another prerequisite of application of Au-Sn plating baths is that the bath must be safe enough for the semiconductor wafers which are to be plated with Au-Sn alloy. A study on corrosion behavior of InP and GaAs wafers in the developed solutions is conducted in Chapter 3. No evidence of corrosion is found for these semiconductors.

Among several plating techniques, pulsed current (PC) plating is claimed to be advantageous over direct current (DC) plating for many plating systems. In Chapter 4, PC plating and DC plating are performed and compared for the developed bath according to their effects on deposit composition and microstructures. Chapter 4 also includes detailed investigations on the effects of several PC plating parameters. e.g., peak current density, ON time, OFF time, and several electrolyte parameters, such as the ratio of Au-Sn content in the bath and total Au-Sn content in the bath. on deposit composition, microstructures, and phase structures.

Annealing tests of a sample with deposit composition close to the eutectic point are conducted in Chapter 5 to look at the annealed microstructure and phase structure and confirm the bonding temperature. Reproducibility tests of the bath are carried out to obtain important information about the reproducibility of the bath and provide useful reference for bath replenishment. Finally, the work is concluded and future work is recommended from a practical point of view in Chapter 6.

Chapter 2

Literature Review

2.1 Literature Review

2.1.1 Application of Au-Sn solder in electronic and optoelectronic packaging

Soldering may be defined as 'a process by which metals may be joined via a molten metallic adhesive (the solder) which on solidification forms strong bonds (usually intermetallic compounds) with the adherents' [Plumbridge 96].

In electronic packaging, solders are extensively used to bond semiconductor chips on a substrate or a package. The package together with the die-bonding layer serves the purpose of mechanical support, heat dissipation and sometimes electrical connections. The quality of the bonding is very important because the device could fail or incur early failure without reliable bonding.

The most important solder properties include solderability, melting temperature, Young's modulus, coefficient of thermal expansion, Poisson's ratio, fatigue lifetime, corrosion resistance, and creep rate. Table 2.1 lists some properties of several solder materials [Tan 96]. Commonly used bonding media include hard solder, soft solder, metal-filled epoxy, and metal-filled glass [Matijasevic 90]. Metal-filled glass has poor thermal conductivity and produces high stress on the die backside due to high processing temperature and lack of plastic deformation. Metal-filled epoxies have poor thermal conductivity but do not induce high stresses on the dice because they deform inelastically under stress. However, they are likely to release contaminants due to outgassing. Soft solders such as Sn-Pb alloys have high thermal conductivity but are mechanically weak. Dice bonded using soft solders do not possess high stress because the bonding layers deform plastically to absorb the stress developed. The capability of plastic deformation, however, makes soft solders incur thermal fatigue and creep rupture. The most commonly used hard solders include eutectic Au-Sn, Au-Ge, and Au-Si alloys. They have high thermal conductivity and are free from thermal fatigue because of high strength, which

results in elastic rather than plastic deformation. Because of the lack of plastic deformation, bonding using hard solders produces high stress on the dice. However, if the bonding layers are nearly free of voids, the high stress developed is usually lower than the strength of the dice. Thus the dice do not crack. On the other hand, if large voids exist in the bonding layers near the die edges, they induce high localized stress and consequently increase the probability of die cracking. Accordingly, for highly reliable devices, hard solders are the preferred bonding media provided good bonding can be achieved.

Au-Sn solder has reduced oxidation. Its soldering is a fluxless process, which is desirable for flip-chip assembly. Eutectic Au-Sn soldering using gold bumps and tin-plated leads is used for the inner lead bonding process (ILB) of TAB-tapes [Zakel 92-2]. Its applications on green tape ceramic substrates and on flexible circuits have been reported [Zakel 95-1, Zakel 95-2]. Au-Sn solder has been widely used in optoelectronic applications due to its high, but practical, melting temperature, and excellent creep resistance, which allows for efficient bonding of devices that also contain temperature-sensitive elements such as Au-based contacts, AlGaAs/GaAs and GaInAsP/InP laser diode chips, and other III-V compound devices. The self-alignment effect of Au-Sn bumps meets the critical requirement of laser chip bonding with precise alignment between laser chip and optical fibers. An example of the application of Au-Sn solder in optoelectronic packaging is given in Fig. 2.1 [Ivey 98].

Since the quality of a bonding structure depends on the appropriate selection of the solder metallurgical system, the barrier metallization scheme and the bonding process, a literature review on these aspects is given below.

2.1.2 Au-Sn metallurgy

2.1.2.1 Au-Sn phase diagram

Bonding with an alloy requires a deep understanding of the reactions present in this alloy as well as the different phases of the system.

In the Au/Sn phase diagram, there exist four different stable intermetallic compounds,

as well as two eutectic and at least three peritectic points. A great deal of work has been performed to establish a complete Au-Sn phase diagram and to study the characteristics of the many phases identified, but the properties and boundaries of several phases are still not completely determined. Work is still being conducted on the refinement of the phase diagram, especially in the Au-rich region. Important properties of the phases themselves are also not well understood.

Recent work has modified this portion of the phase diagram shown in Fig. 2.2 [Matijasevic 93]. The eutectic that forms at 278°C is suitable for soldering and bonding because of its mechanical properties, while the lower melting eutectic (Sn-rich) at 217°C is known to be brittle.

The eutectic reaction occurs at 278°C at 29.5at% Sn, responding to a composition of 20wt% Sn and 80wt% Au. This eutectic composition is defined by steep liquidus lines on both sides of the eutectic melting point, particularly the Au side. This means that, for example, enriching the eutectic composition by 1wt% of Au leads to an approximately 30°C increase in the melting temperature. Thus, it suggests that the Au-Sn solder system requires very accurate process control of both the solder composition and the bonding temperature to permit successful bonding. The eutectic alloy has the ζ and δ phases as its constituents at equilibrium state.

The ζ phase has been found to extend from at least 9.1at% Sn at 521°C to 17.6at% Sn at 280°C, and has a Mg-type c.p.h. lattice [Matijasevic 93]. The δ phase is the AuSn intermetallic compound with a melting point of 419.3°C. This silver-gray material is more brittle than Au and harder than either Au or Sn. This non-stoichiometric compound has a homogeneity range between 50.0 and 50.5at% Sn. The AuSn phase is a subtractional solid solution of a limited range that can be designated as $Au_{1-x}Sn$ ($0.00 \leq x \leq 0.02$). It has been confirmed that the subtraction of Au atoms from the AuSn lattice occurs. The structure of the AuSn lattice is NiAs-type hexagonal with two molecules of AuSn associated with the unit cell. AuSn is quite stable.

2.1.2.2 Wetting, oxidation and segregation

Wettability is one of the most important properties of solder. Although Au-Sn

eutectic solder has reaction energies as the driving force for wetting and its shear viscosity is very low, a scrubbing motion or static pressure needs to be used to achieve complete wetting of the surfaces because of the oxide film that prevents contact with the bonding surface. Electron spectroscopy for chemical analysis (ESCA) studies performed on eutectic alloy preforms before and after melting have shown that most of Sn on the surface of eutectic alloy is in oxide form [Matijasevic 93]. Apart from the fact that the surface of the melted preform is completely oxidized, a significantly smaller Au composition on the surface was identified compared with the eutectic preform scan.

In addition to a substantial amount of carbon and oxygen, it was found that the relative concentration of Sn and Au are not as they should be in the eutectic alloy [Johnson 91]. The Sn composition was 57.4at% rather than the eutectic composition of 29.5at%. As the preforms were melted and heated to higher temperature, the Sn composition in the surface layer increased. An increase in oxygen content was also noted. This observation suggests that, in the melting process, Sn segregates to the surface of the alloy. Even samples cleaned with ion bombardment and then melted and solidified still had 42at% Sn on the surface. An oxidized preform that was subsequently melted and re-solidified exhibited an even greater Sn segregation with a concentration of 68.4at%. The Sn oxidized on the surface even though the melting process was performed in an H_2 environment. The significant amount of C identified was caused by surface contamination.

Tin segregates to the surface of the Au-Sn alloys because it has a smaller surface free energy than Au (0.6 Jm^{-2} for Sn vs. 1.4 Jm^{-2} for Au at just below their melting points). The driving force for segregation is thus the heat of adsorption (also known as heat of segregation), which represents the enthalpy change, that results when an atom of Sn in the bulk phase exchanges positions with an atom of Au lying in the surface phase. The relative size of the two atoms play a role as does the strain energy associated with a solute atom in a solid solution of the solvent atom. Alloy parameters such as atomic size ratio, surface tension ratio and bond strength ratio can also be used to predict successfully the segregating component to be Sn. In addition, chemisorption of O_2 tends to increase the surface concentration of Sn because of the higher stability of tin oxide.

Studies performed on Sn oxidation do not agree on the form of the Sn oxide. A recent

study using selected area diffraction identified SnO_2 as the oxide formed. Using standard thermodynamic principles the equilibrium partial pressure of oxygen for solder oxidation can be calculated. For Sn oxidation at 300°C, which is used for melting the Au-Sn eutectic alloy, the calculation gives a value of 5×10^{-40} atm (5×10^{-43}MPa). This indicates that a very small amount of O_2 present will cause Sn oxidation.

2.1.3 Diffusion behavior of Au and Sn

Currently, the most advantageous Au-Sn solder fabrication process is sequential deposition of multiple Au and Sn layers on a wafer. A schematic presentation of a conceptual design of a bonded device is shown in Fig. 2.3. The interdiffusion behavior between Au and Sn layers influences the bonded microstructure. Some low-temperature bonding techniques are based on the fast interdiffusion between Au and Sn layers. Diffusion between Au-Sn solder and metallic leads on substrates can be a critical failure mechanism. Therefore, the diffusion behavior of Au and Sn has been extensively studied [Buene 80-1, Buene 80-2, Gregersen 81, Hugsted 82, Marinkovic 88].

Au-Sn couples or multilayered structures have been shown to form compounds corresponding to different portions of the phase diagram. X-ray diffractometry studies performed on Au-Sn thin film couples indicated that alloys could be formed without melting, i.e., by solid state diffusion.

Study of diffusion of Au in Sn single crystals revealed that very rapid Au diffusion was attributed to an interstitial mechanism. This diffusion is 3~4 orders of magnitude faster than self-diffusion of Sn. With the use of a diffusion marker and depth profiling by Rutherford Backscattering Spectroscopy (RBS), it was found that Au diffuses very rapidly both interstitially and along the grain boundaries of Sn. Within the investigated temperature range of 55°C to 125°C, a tin layer of a few microns in thickness is consumed within only a few hours. From the grain boundaries, Au diffuses into the grains by an interstitial mechanism and is included in the grains by the formation of an intermetallic phase. The diffusion along the grain boundaries and into the grains is very rapid and phase formation becomes the limiting process. Sn diffusion along Au grain

boundaries was also found, but it is slower than Au diffusion along the Sn grain boundaries. It was found that AuSn is the first compound to form during interdiffusion. In addition to AuSn, $AuSn_4$ compound formation in the initial stage has also been observed. While AuSn formation occurs at the interface, $AuSn_4$ formation occurs within the Sn film and is due to fast grain boundary diffusion of Au into Sn. Phase formation at later stages of interdiffusion involves the decomposition of one of these phases. If there is a high concentration of Au in the overall alloy, the $AuSn_4$ phase disappears, whereas, for a Sn-rich film couple, AuSn eventually consumes all the Sn and transforms to $AuSn_2$ and $AuSn_4$. Fig. 2.4 shows the scheme of intermetallic compound formation and Kirkendall void formation [Zakel 95-2]. In general the brittle intermetallic compounds $AuSn_4$, $AuSn_2$ and AuSn are critical for the mechanical properties of solder materials. A more critical effect for reliability is the formation of Kirkendall voids. Kirkendall pore formation was investigated by Nakahara [Nakahara 80].

Since AuSn compound formation at the interface was found to be a diffusion-controlled planar growth process, the kinetics of phase growth shows a parabolic time dependence.

The publications on the metallurgy of OLB-contacts in TAB-technology show that the presence of the Au-Sn intermetallics in the solder fillet does not necessarily reduce the reliability of the solder joints [Zakel 94-2]. The formation of Kirkendall-voids was identified as a critical failure mechanism in this case. Due to diffusion, voids are formed at the interface between the copper lead and the Au-Sn alloy during high temperature storage if a critical Au-concentration (10wt%) in the solder fillet is exceeded.

2.1.4 Metallization systems compatible with Au-Sn solder

It has been reported [Wada 92] that Sn could deteriorate GaAs-based lasers through its persistent penetration into the GaAs bulk. The most disturbing effect of the consumption of the Sn from the solder overlayer is the formation of an Au-rich solder layer, resulting in elevation of the solder melting temperature and premature freezing during the bonding cycle. Therefore, it is extremely important to develop a metallization

system by combining solder and a thin, stable barrier metal. This metallization system should also provide excellent adhesion properties at both the barrier/substrate interface and solder/barrier interface.

The commonly used adhesion-barrier metallization in III-VI based system is Ti/Pt. Ti is introduced typically as an adhesion layer adjacent to substrate and Pt acts as a barrier layer. Although Ti/Pt is the industry standard, only a narrow bonding processing window is available because of its relatively unstable properties. It has been reported that a Ti/Pt/AuSn metallization system undergoes rapid and extensive metallurgical interaction between Pt and Sn to form intermetallics, such as PtSn. The Pt-Sn and Pt-Au phase diagrams are presented in Fig. 2.5 [Katz 94-1].

The reaction may lead to mechanical deterioration of the bonded assembly, resulting in delamination of the metal and failure of the bond. The Pt layer and an appreciable amount of Sn are consumed, leading to the dissolution of the Ti adhesion layer after the disappearance of the barrier layer and premature solidification of the solder during the bonding cycle. In order to improve the thermodynamic stability of the bonding system and to achieve a more robust bonding process, Katz and his co-workers systematically explored potential metal alternatives, such as Ni, W, Cr and some of their alloys, for the barrier metals [Katz 94, Lee 94, Wada 91]. Katz [Katz 94-1] thoroughly reviewed their studies on proposed new metallurgical systems used for bonding high-power laser devices onto submounts, and in particular onto CVD-diamond submounts, and evaluated their quality based on wetting performance, thermodynamic stability and lack of premature freezing of the molten solder.

The thermodynamic stability of the solder was judged by both the surface and the global freezing times of the solder, as well as the adhesion of the molten and solidified Au-Sn solder to the various barrier metals. A minimum interaction between the Au-Sn solder and the barrier metals is required to eliminate solder deterioration, and thus allow for a long solder non-freezing period. The applied metallization should, however, undergo some interaction with the solder in order to promote sufficient adhesion of the barrier metals to the solder. The microstructure of the various metallization systems, as deposited and after reflow in both N_2 ambient and in liquid flux, were studied in detail, and correlations between it and the solder refreezing time were evaluated.

The first set of systems tested contained a conceptually similar structure; 0.1μm of Ti as an adhesion layer adjacent to the submount, capped with 0.2μm of barrier metal, onto which 3μm of AuSn solder was deposited. Ni, Cr and W were deposited separately as barrier layer metals. The binary phase diagrams for Au-Ni, Ni-Sn, Au-W, Au-Cr and Cr-Sn are shown in Fig. 2.6 [Katz 94-1]. All these metals were found to be less reactive with the Au-Sn solder than Pt. W was found to be absolutely inert. Surface local freezing and global freezing phenomena were not observed during reflow in forming gas or flux, but the solder dewetted from the W layer, reflecting insufficient interaction and adhesion of solder to the W layer.

Therefore it was concluded that in order to obtain good stability and adhesion of the solder on the barrier metal, a more complicated system had to be applied.

The first multilayer that was studied was the Ti/W/W-Au/AuSn system. The adhesion of the solder was improved somewhat by introducing a W-Au co-deposited layer between the solder and the W layer. By reflowing the sample under forming gas at 320°C, good integrity of the solder to the W layer was achieved. However, dewetting still occurred at the higher reflow temperature of 350°C. Reflowing the sample in a liquid flux resulted in complete delamination of the solder from the W layer, even at the lower temperature of 320°C.

The second studied multilayer was a Ti/W/W(AuSn)/AuSn system. Introducing an improved ternary wetting layer between the Au-Sn solder and the W layer resulted in complete elimination of solder delamination from the W layer during reflowing at 320°C. Occasional dewetting of the solder from the W layer was still observed during the reflowing of the sample at higher temperature. The improved stability led to an extension of the solder local freezing time to about 25s, and more than 500s was required for complete solidification of the solder.

Final modification and optimization of the barrier metallization were achieved by adding a second wetting layer between the adhesion layer and the solder. The composition of the entire scheme was Ti/W/W(Ni_3Sn_4)/Ni_3Sn_4/AuSn. This system showed excellent thermal stability at all treatment temperatures. Surface local freezing time was longer than 200s and the global freezing time was found to be longer than 60 minutes. No dewetting was observed in the reflow samples, regardless of the ambient.

Thus it was concluded that this five-layered barrier system provided the best bonding metallization scheme of all the systems that had been studied.

2.1.5 Fabrication techniques

Traditionally, solder preforms, pastes or sequentially deposited solders and sequentially electroplated deposits have been used to bond microelectronic and photonic devices onto submounts.

In order to produce a foil preform of Au-20wt%Sn, a chill-block melting-spinning technique is utilized, which involves forming a molten charge through a small hole onto a rapidly spinning, water-cooled copper wheel. The high rate of heat extraction obtained by this process causes the metal to solidify almost instantaneously on striking the wheel, resulting in the formation of a thin strip of the alloy with an amorphous or micro-crystalline structure. For details of this technique, see reference [Jones 82]. Gold-tin preforms suffer from a number of disadvantages. They are subjected to oxidation prior to the initiation of the bonding cycle. The handling and alignment of thousands of preforms is problematic and requires expensive 'pick and place' robotics. Usually a solder perform is 20~50μm thick. It is difficult to fabricate thinner solder layers. For many applications, the preforms are thicker than required, which can cause bridging and shortages for fine-pitch applications. In addition, when the dimensions of the bond areas decrease below 100μm through the introduction of the flip-chip concept, dealing with preforms becomes impractical.

Solder paste screen printing is a simple process with low operating cost, but paste consists of fine Au-Sn powder and organic adhesives. Not only are solder particles very vulnerable to oxidation, but residue from organic decomposition during bonding contaminates the solder.

Solder can be deposited by various thin film deposition technologies, such as vapor deposition using patterned thick photoresist or a shadow mask and electron-beam evaporation using a shadow mask or patterned photoresist. Electron-beam evaporation is the most commonly used method to sequentially produce Au-Sn solder in a multilayer

manner [Katz 94-1, Pittroff 95, Lee 91]. Resistance-heated evaporation has also been employed to carry out deposition of Au and Sn to a total thickness of about 2.5μm [Dohle 96, Wada 92].

Au-Sn solder layers have been produced through sequential electroplating [Kallmayer 95-1, Kallmayer 95-2, Zakel 95-1]. The flow chart of the bumping process by electroplating Au-Sn is shown in Fig. 2.7 [Kallmayer 95-1]. First a plating base of Ti:W and Au is sputtered on the silicon wafer with Al pads. The Au layer is the necessary starting base for electroplating. The sputtering step is followed by spinning on a photoresist layer, which is structured in a photolithographic step. After electroplating gold and tin, the photoresist is removed. In a final step the plating base is selectively removed by etching. The realization of extremely fine pitch bumps (~10μm) is possible and is shown with this bumping process. The electroplating allowed different tin heights to be fabricated in order to meet the needs of different soldering processes. For the formation of an eutectic solder composition, 1μm of tin dissolves 1.5μm of gold. For flip-chip assembly, typically a tin thickness of 5 to 10μm is chosen on an Au pedestal of 25 to 50μm, whereas in TAB technology 3 to 4μm of Sn is typically used. Commercial Au bump and Sn bump electroplating baths are available.

Co-evaporation of Au-Sn solder has been reported [Ivey 97]. The co-evaporated eutectic solder had much lower porosity than solders obtained by a sequential evaporation process.

Comparing these fabrication processes, deposited solder provides significant advantages over preforms and solder pastes, such as decreased oxide formation prior to the bonding cycle and more accurate control of the bonding media thickness and volume [Lee 91]. Electroplating is a low-cost fabrication process relative to evaporation. It is believed that it has better thickness and positional control of solder and less oxidation than preforms. In addition, it has the potential to minimize the voiding problem in bonding layers. Currently no commercial bath for Au-Sn alloy plating is available.

2.1.6 Bonding using Au-Sn metallurgy

2.1.6.1 Bonding techniques

A flexible application of Au/Sn solder is dependent on its bonding condition. The already feasible methods include reflow soldering in an infrared oven and thermode bonding on a pulse heated thermode. Vapor phase soldering and laser bonding of Au/Sn bumped chips are the relatively new approaches to fluxless flip chip process. An overview of the basic differences between the technologies treated here is given in Table 2.2 [Kallmayer 95].

Reflow-soldering with infrared heating

Self-alignment is the main advantage provided by reflow soldering in an infrared oven under an active atmosphere. This is a technique used to achieve high accuracy using only simple equipment. Still the heating rate of the infrared oven has to be high. The advantages already mentioned are especially important in the assembly of optical components. The assembly of optical components using the self-alignment of layered Au-Sn bumps soldered in an active atmosphere was reported by R. D. Deshmukh *et al.* [Deshmukh 92]. Results on self-alignment using electroplated Au-Sn bumps have also been published [Kallmayer 95-3].

Pulse heated thermode

Pulse heated thermode is a new application of Au-Sn metallurgy, which is most important for reliability. The reliability of flip chip assemblies, especially with larger chips, depends largely on the underfill material and its adhesion to the substrate. Flux residues might affect the reliability by reducing the adhesion of the underfiller. Bonding using a pulse-heated thermode requires special equipment as the Au-Sn solder demands a high heating rate that can not be achieved by a flip chip bonder with IR-heated thermodes. The use of a pulse-heated thermode offers the possibility of FC-bonding on a flexible substrate with Au-Sn solder in spite of the high temperature necessary [Kallmayer 95-2]. These low cost substrates are particularly interesting for portable

consumer applications as three dimensional shapes of electronic circuits can be realized and adapted to the individual product.

Vapor phase reflow

Vapor phase reflow technique uses a condensing inert vapor as the heat-transfer medium, offering the advantage of self-alignment as with soldering in an infrared oven (see Fig. 2.8) [Kallmayer 95-1]. Liquids are available for the vapor phase with boiling points at temperatures up to 300°C. The vapor phase provides an inert atmosphere with very low residual oxygen without the need of nitrogen or active atmosphere during the soldering process. There are no parameters to be changed except the duration of the different steps, which makes the process easy to handle.

Laser bonding

The use of a laser as an alternative bonding method was investigated in order to avoid the heating of the flexible circuit during the collective flip chip assembly with the thermode. Azdasht *et al* [Azdasht 94] showed that the FPC (Fiber Push Connection) was a suitable laser connection method offering several solutions to the mentioned problems. In this system the laser beam is transported by a glass fiber to the contact parts. The end piece of the fiber serves at the same time as a push unit (see Fig. 2.9). By pressing the connecting parts with the tip of the fiber, an optimal thermal coupling is achieved. The essential advantage of this method compared with contactless laser applications lies in the fact that a part of the laser energy is transformed into heat at the end surface of the fiber, due to its attenuation properties. This single point bonding only heats the flexible circuit locally. By avoiding the thermal expansion of the whole circuit higher alignment accuracy is achieved, which is beneficial for the assembly of flexible circuits with large dimensions and fine pitches.

Low temperature diffusion bonding

Conventional bonding techniques using Au-Sn preforms or paste usually require a process temperature near 320°C to ensure complete melting of the preforms. However, a 320°C process temperature is too high for many devices such as AlGaAs/GaAs and

GaInAsP/InP laser diode chips. Thus a lower temperature bonding process is desirable. Multilayer bonding using Au-Sn solders at a temperature below the eutectic temperature has been accomplished by Lee *et al* [Lee 92]. The technique needs only 260°C to produce nearly eutectic Au-Sn bonding. It utilizes the unique property of the Au-Sn alloy system in that the 232°C tin melting point is significantly lower than the 280°C eutectic point. Moreover, the Au-Sn system is known to be a rapid, solid-state interdiffusion system.

The bonding medium/Au-Sn multilayer composite was deposited directly on the object to be bonded (see Fig. 2.10). The bonding was performed by heating the sample at 260°C for 10 minutes in a hydrogen atmosphere with a static pressure of 0.276MPa ($40lbin^{-2}$). No bonding degradation and die cracking were observed by a scanning acoustic microscope (SAM).

This technique is particularly useful for bonding electronic and optical devices, which cannot take a temperature above 260°C.

2.1.6.2 Evaluation of bond quality

Mechanical testing is conducted to obtain bonding strength data. The usual methods include tensile testing (e.g. MIL-STD 883C, Method 2027 [MIL 77]) and shear testing.

Fatigue behavior is tested through thermal cycling, e.g., between -196°C (liquid nitrogen) and 160°C (boiling cyclohexanoe)[Lee 92].

Thermal impedance is a particularly important property in the channels of the ridge waveguide structure, where the bonding solder is close to the active region of the laser.

A reliable measurement technique, as described by Paoli [Paoli 75], involves using the wavelength of an individual Fabry-Perot mode to monitor changes in the junction temperature. Thermal impedance testing methods are being further developed.

Thermal stability of eutectic solder can be tested by differential scanning calorimetry (DSC) analysis [Katz 94].

In understanding the bonding mechanism and observing bonding structures, a large group of characterization tools are employed. The characterization includes morphology observation (by scanning electron microscopy (SEM), transmission electron microscopy (TEM)) and void detection (by X-ray radiography, and scanning acoustic microscopy

(SAM)). Auger electron spectroscopy (AES) is used for surface analysis and Au-Sn compositional profiles. Rutherford backscattered spectroscopy (RBS) is effective in measuring the solder composition and thickness in as-deposited and annealed layer structures. Phase determination is performed by x-ray diffraction (XRD) and energy dispersive x-ray spectroscopy (EDS). Bulk composition of the solder preform can be determined by inductively coupled plasma spectroscopy (ICP).

2.1.7 Problems in application of Au-Sn alloy

A major problem affecting bond quality of Au-Sn solders is voiding in bonding layers. One of the causes is the segregation and formation of materials such as oxides, carbon and silicon on the molten solder solution [Matijasevic 93]. These materials form a solid film on the solder solution, which prevents the solution from achieving bonds with the die and the package. The oxide layer, which exists on the surface of the as-fabricated solder preform, is further enhanced in the bonding processes when the preform melts. To break down the oxide film, it is common to use scrubbing in the process. While the scrubbing action does break down the oxide film, it may also induce voids and inhomogeneity in the bonding layer. A technique using controlled scrubbing has been reported to produce good quality bonding of GaAs dice with an Au-Sn alloy [Nishiguchi 90]. Matijasevic *et al* [Matijasevic 90] have also achieved good bonding, utilizing a static pressure of around 0.14MPa (20lb/in^2) rather than scrubbing action to break down the surface film.

Other sources of pores in Au-Sn alloys include Kirkendall void formation due to the rapid interdiffusion in the Au-Sn multilayer system [Nakahara 80, Zakel 94] and gas trapping during the Au-Sn fabrication process [Ivey 97].

The fatigue behavior of Au-Sn solder depends on the type of the intermetallics in the solder [Tan 96]. The following equations can be used to estimate the fatigue life (number of thermal cycles to failure) for a solder joint.

$$\text{Shear strain} = \Delta\nu = L(\alpha_1-\alpha_2)\Delta T/h \qquad (2.1)$$

$$\text{Fatigue life} = N_f = 0.5(\Delta v/0.65)^{-2.26} \quad (2.2)$$

where

L = distance between the solder joint and the neutral point of the assembly;

α_1 and α_2 = coefficient of thermal expansion (CTE) of the component and the substrate;

ΔT = range of the temperature;

h = height of solder joint.

From the equations it can be seen that fatigue behavior is strongly depend on the CTE of the solder material. Therefore the composition of intermetallic compounds in a Au-Sn alloy plays an important role in the fatigue behavior, since different intermetallic compounds have different CTEs.

The cost of bonding using Au-Sn is another problem in its application. Besides the high cost of the precious materials, Au-Sn solder fabrication often involves expensive thin-film deposition equipment. Much work is being done to lower the overall cost by introducing low-cost fabrication processes or low-cost bonding processes.

2.1.8 Electroplating of Au-Sn solder

Electroplating processes have long been used in the electronics industry. Early application of electroplating with semiconductors includes the deposition on the die backside for attachment and more recently on the die frontside for electrical contact. The most commonly used Pb-Sn solders and gold bumps are usually obtained by electroplating [Catonne 84]. There are many potential uses for electroplating as well as cost reduction, such as electroplated copper wiring on IC chips [Andricacos 98] and electroplating of nanoscale and nanophase materials [Switzer 98].

2.1.8.1 Sequential electroplating of Au-Sn solders

Sequential electrodeposition of Au-Sn solder has been employed to form Au-Sn bumps on an Au starting base [Kallmayer 95-1]. Commercial baths are available for generating gold bumps and tin capping layers.

The electrodeposition of soft gold on electronic devices and components is generally performed using a bath containing cyanoaurate(I) ions, because gold cyanide complexes have the highest stability coefficient values. The stability coefficients for several gold complexes are shown in Table 2.3 [Stanley 87]. The free cyanide ions are generated as a result of the gold deposition reactions. Because they attack the interface between the resist film and the substrate, lifting the resist and depositing extraneous gold under the resist [Honma 95], they are incompatible with positive photoresists generally employed to produce circuit patterns. Thus more and more research has focused on developing a non-cyanide bath. Most intensively studied non-cyanide gold baths are in the form of Au(I) sulfite complexes. In contrast to cyanide baths, Au sulfite baths have better compatibility toward comparable resists. Moreover, they have increased throwing power and yield deposits exhibiting more uniform thicknesses [Traut 90]. However, the Au(I) sulfite complex itself is subject to a disproportionation reaction to form Au(III) and metallic Au, which causes the bath to decompose spontaneously on standing.

$$3[Au(SO_3)_2]^{3-} = 2Au + [Au(SO_3)_4]^{5-} + 2SO_3^{2-} \qquad (2.3)$$

To prevent the decomposition, therefore, a suitable stabilizing additive must be used. The first commercial sulfite gold plating solutions were developed in the early to middle 1960s. The sulfite ion is itself in equilibrium with sulfur dioxide according to

$$SO_3^{2-} + H_2O \leftrightarrow SO_2(g) + 2OH^- \qquad (2.4)$$

Because reaction (2.4) forms hydroxyl ions, the equilibrium is pH-dependent. As originally configured, sulfite gold plating solutions operated at pH values above ~9.5. Most commercially available solutions still do so. Table 2.4 lists an example of such a

plating bath [Gemmler 94]. There have been numerous attempts to reduce the operating pH of the gold sulfite solutions to lower than neutral, as, for example, in plating on circuitry defined using alkaline-developable photoresists [Gemmler 94, Morrissey 94, Morrissey 93, Osaka 97]. In addition, when gold is plated out of the solution at alkaline pH, the excess sulfite remains and can become oxidized to sulfate at the anode. If a sulfite gold plating solution could be operated under stable control at pH values below about 6.5, the controlled evolution of sulfur dioxide could be used to remove a portion of the excess sulfite in a manner analogous to that by which excess cyanide is volatilized from the acid gold cyanide electroplating system. Meyer and co-workers first reported that in the presence of organic polyamines, notably ethylenediamine, gold sulfite solutions could be operated at a pH as low as 6.5 [Meyer 69]. Laude *et al.* claimed that even in the absence of polyamines, solutions based on ammonium gold sulfite could be operated at pH 6 - 8 [Laude 80]. A sulfite gold plating solution capable of stable operation at pH as low as 4.0 using an organic polyamine or mixture of polyamines of molecular weight from 60 - 50,000, and an aromatic organic nitro compound, was developed by Morrissey [Morrissey 94, Morrissey 93].

One of the advantages of the gold sulfite process is that the deposits are bright, hard and very ductile, whereas the cyanide based acid electrolytes yield deposits of limited ductility. Another advantage is the good throwing power. The structures of the sulfite gold electrodeposits are amorphous.

Phosphate, carbonate, acetate, citrate, etc. are the commonly used buffering and conducting salts for a gold plating bath. The brightening additives that can be used in a alkaline gold sulfite plating bath include brightening metal additives (Cd, Ti, Mo, W, Pb, Zn, Fe, In, Ni, Co, Sn, Cu, Mn, V) at 1 - 5000 mg/L or brightening semi-metal additives (Sb, As, Se, Te) at 1 - 400 mg/L [Foulke 74]. In alkaline gold plating electrolytes, arsenic species exist in the form of polyarsenite $[As(OH)_3]_x$. The part of polyarsenite that preliminarily remains soluble acts as a leveling and grain-refining agent ($polyarsenite_{active}$). The alloying elements for gold sulfite electrolytes can be Cd, Pb, Sb, Zn, Fe, In, Ni, Co, Sn, Cu, and Mn at 0.5 - 5 g/L [Foulke 74].

One of the problems of gold sulfite plating solutions lies in its stability. Although a high, free sulfite concentration in the electrolyte can improve its stability, a gradual

precipitation of gold can occur. Gold precipitation is explained as the result of a locally exaggerated concentration of uncomplexed Au(I)-ions in the solution (e.g., by anodic oxidation of sulfite to sulfate or by its oxidation at the liquid/air phase boundary). Controlling the anode potential and minimizing the extension of the liquid/air phase boundary will hinder gold precipitation. Dithionite formed from sulfite at the cathode and subsequently transported to the bulk electrolyte reduces aurous ions to gold. By using a stabilizer, the formation of dithionite is restrained.

The possibility of electroplating soft gold from a non-cyanide bath containing both thiosulfate and sulfite as complexing agents, specifically for formation of bumps by electroplating, has been explored [Osaka 97]. The thiosulfate-sulfite mixed system has recently been used successfully for formulating non-cyanide electroless gold baths yielding good bath stability and deposit properties [Inooue 95, Kato 95]. The basic composition and operating conditions of gold(I) thiosulfate-sulfite baths are shown in Table 2.5. The bath is stable, but no data for bath stability were reported. Three different gold complexes can exist in this system:

$$Au^{+} + 2SO_3^{2-} \rightarrow [Au(SO_3)_2]^{3-}, \qquad \beta = 10^{10} \qquad (2.5)$$

$$Au^{+} + 2S_2O_3^{2-} \rightarrow [Au(S_2O_3)_2]^{3-}, \qquad \beta = 10^{26} \qquad (2.6)$$

$$Au^{+} + SO_3^{2-} + S_2O_3^{2-} \rightarrow [Au(SO_3)\,(S_2O_3)]^{3-}, \qquad \beta = \text{unknown} \qquad (2.7)$$

where β is stability coefficient for the gold complex. Thallium(I) ions were added in the form of Tl_2SO_4 as a 'grain refiner'. Tl and Pb ions decrease the grain size and improve the surface morphology of the deposit. It is well established that these ions undergo so-called underpotential deposition (UPD) on gold, and that the addition of these ions to the plating bath significantly depolarizes the gold electrode or shifts the gold deposition potential in the positive direction. The depolarization effect of thallium in the thiosulfate-sulfite system can be attributed to the catalytic effect of adsorbed Tl formed by UPD (reaction (2.8)), reacting with $[Au(S_2O_3)_2]^{3-}$ to form Au by the galvanic displacement reaction represented by reaction (2.9).

$$Tl^{+} + e \rightarrow Tl_{ads} \quad (2.8)$$

$$Tl_{ads} + Au(S_2O_3)_2^{3-} \rightarrow Au + 2(S_2O_3)^{2-} + Tl^{+} \quad (2.9)$$

with the overall reaction given by

$$Au(S_2O_3)_2^{3-} + e \rightarrow Au + 2(S_2O_3)^{2-} \quad (2.10)$$

Nodules and pits are the characteristic deposit defects during bump plating. According to the description of the primary current distributions at cathodes, both with adjacent conductive and non-conductive particles, the modification of the current field around adsorbed particles is characteristically evident. In compliance with the current distributions, pits can form due to the residues in the resist opening or the incorporation of dragged-in resist or other non-conductive particles; nodules can grow from conductive gold particles.

There are two types of tin plating solutions: alkaline and acid [Tan 93]. Alkaline solutions are based on sodium or potassium stannate. Hydrogen peroxide or sodium perborate are used to oxidize any stannite (bivalent tin) to the stannate form. Alkaline baths are superior to the acid baths in throwing power. All acid tin baths contain the tin in bivalent (II) form. The metal salts are sulfates, fluoborates and fluosilicates. Among these salts, the first two are the most commonly used anions in the tin plating system. The electrodeposition of tin from a stannous tin solution has the obvious advantage of consuming less electricity, 2.214 g of tin per Ahr at 100% efficiency, compared with only half this amount, 1.107 g, from a stannate bath. The problems of an acid tin plating bath include poor covering power and solution instability, tending to precipitate basic tin compounds on standing. Various additives have been tried to overcome the poor plating quality. These include gelatin, glue, cresol sulphonic acid, and an aromatic hydroxyl compound (such as nonyl phenol), or a combination of some of these items. Commercially formulated additives are available and the additives are included as part of the total package. When an acid bath ages, the bath may change its color to darker yellow and the bath turns turbid. The actual chemistry of this change is relatively poorly

understood. It is attributed to the formation of stannic compounds when the stannous tin salt is oxidized to stannic in the presence of dissolved air and elevated temperature. The stannic compounds are in colloid form, and are very difficult to remove. The turbid bath should not be of much concern, except that it consumes more electricity and when the grain size is large the plating chemical residues are easily trapped. Several ways to minimize the oxidation of stannous tin include maintaining the bath at 20 - 25°C, using an airtight plating setup and adding a suitable anti-oxidant such as a phenol compound. The additive formulation in most tin and solder alloy plating systems contains an anti-oxidant to minimize the oxidation of stannous (Sn^{2+}) to stannic (Sn^{4+}). Steinbicker and coworkers [Steinbicker 78] found that the oxidation of bivalent tin ion in an acid halogen electrotinning bath, containing bivalent tin ions, can be greatly suppressed or in most cases virtually eliminated by adding a quantity of at least one organic ring compound, which has a radical group such as NH_2 or NO_2 attached in the ortho or para position. Organic ring compounds which can be used are acetanilides, such as para-aminoacetanilide or para-nitroacetanilide. These ring compounds are maintained at a concentration of between 0.01 and 4.0 g/L of solution in the bath. Para-aminophenylacetic acid and 4-aminoantipyrine can be added to the bath and, in the presence of sodium ferrocyanide, reduce the rate of oxidation of bivalent tin ion.

2.1.8.2 Electroplating of Au-Sn alloys

The available information concerning the electrodeposition of Au-Sn alloys is virtually confined to the patent literature. One of the difficulties with Au-Sn alloy plating baths is preventing the oxidation of tin (II) to tin (IV) [Mason 74]. While such oxidation can be limited by using soluble tin anodes, gold is deposited on these anodes unless they are isolated by semi-permeable diaphragms. These aspects of Au-Sn alloy deposition have restricted commercial development of these alloys, despite their attractive properties.

An early report by Raub and Bihlmaier stated that Au-Sn alloys containing up to 30 at% Sn could be deposited from baths containing no free cyanide, and containing the tin as its stannate complex formed with KOH [Raub 37]. Later claims concerning Au-Sn

alloy plating, however, have been based upon the use of both alkaline and acid cyanide electrolytes, in which the tin has at times been incorporated more with the object of obtaining brightening effects than producing deposits containing significant amounts of tin.

Several recent reports on gold-tin cyanide, chloride and sulfite electroplating systems are reviewed in the following [Kubota 84, Matsumoto 86, Morrissey 92, Tanabe 83].

Cyanide systems

Frey and Hempel developed a bright Au-Sn alloy plating bath with a pH of 3 - 14 [Frey 95]. The bath is comprised of 1 - 40 g/L potassium dicyanoaurate, 1 - 100 g/L soluble Sn (IV), 0 - 20 g/L potassium hydroxide, 50 - 100 g/L potassium salt of gluconic, glucaric and/or glucuronic acid, 5 -100 g/L conductivity salt, 1 - 6 g/L piperazine and 1 - 100 ppm arsenic. This bath can be used to plate small parts, especially plug contacts with an Au-Sn alloy containing 75 - 95 wt% Au. The bath produces bright deposits that remain bright at large thickness (more than 0.1μm) and has long term stability without the use of soluble tin anodes.

Another patent gave a solution for Au-Sn alloy electroplating which yields a ~5 μm Au-8wt% Sn alloy [Kuhn 95]. The solution formula and plating condition are listed in Table 2.6.

Au-Sn alloy codeposition from a cyanide system using pyrophosphate as a buffering agent was studied by Kubota *et al.* The basic formula consists of $K_4P_2O_7$, $KAu(CN)_2$, and $SnCl_2.2H_2O$. The bath makeup, electrolytic conditions, and the composition and current efficiency of alloy deposits have been studied [Kubota 83]. The mass transfer was investigated to clarify reaction mechanisms between monovalent gold or bivalent tin and pyrophosphate ions, by measuring conductivity, kinematic viscosity and limiting current density of bath components [Kubota 84]. The conductivity of the bath was measured by a conductivity meter using a cell with a constant of 10 cm^{-1}. Kinematic viscosity, ν, was calculated from measurements with a Cannon-Fenske viscometer. It was found that two pyrophosphate ions are complexed with one stannous ion. The excess pyrophosphate functions as a supporting constituent.

Tanabe *et al.* [Tanabe 83] obtained various Au-Sn alloys by electrodeposition from

cyanide baths containing $HAuCl_4.4H_2O$, $K_2SnO_3.3H_2O$, KCN and KOH. Although a linear relationship was not found between the Sn content in the bath and the Sn content in the alloy formed, a relationship was found between the two that allows formation of a desired alloy. It was also found that the alloy composition of the electrodeposited Au-Sn was shifted by about 10 at% to the Sn side in comparison with the alloys at thermal equilibrium, thus exhibiting the ζ phase in the 25 - 29 at% Sn range. The intermetallic compounds of AuSn, $AuSn_2$, and $AuSn_4$ were electrodeposited.

Chloride systems

Gold chloride electrolytes were used in the early days in the plating of gold, but today they are applied almost exclusively in the electrochemical refining of gold. An extensive investigation [Nicol 76-1, Nicol 76-2] of the cathodic behavior of gold in chloride solutions has shown that the quality of the cathode deposit is strongly influenced by the relative amounts of gold (I) and gold (III) present in the solution. Table 2.7 lists the standard reduction potentials for various reactions of gold [Stanley 87]. The reduction of gold (III) chloride to the metal can be expected to involve the formation of gold (I) as an intermediate species. Under plating conditions, gold will be deposited from both the gold (III) and gold (I) species. Since gold (I) has a more positive plating potential, 1.154V, than gold (III), 1.002V, a limiting current density for gold(I) will be reached first and it can be expected that the deposits are generally of poor quality, in that they tend to be bulky and porous. Gold fines will be present in the solution as a result of the disproportionation reaction:

$$3AuCl_2^- \leftrightarrow 2Au + AuCl_4^- + 2Cl^- \qquad (2.11)$$

Detailed studies of the anodic and cathodic reactions have shown that the use of low temperatures and periodic interruption of the current are major factors that can contribute to reduced gold (I) concentration.

A recent patent [Matsumoto 86] reported a pH 3 - 7 Au-Sn alloy plating bath containing 2 -50 g/L $KAuCl_4$, 2 - 50 g/L $SnCl_2$, 5 - 500 g/L triammonium citrate, ~30 g/L L-ascorbic acid, 1 g/L $NiCl_2$ and 5 g/L peptone. A 7μm Au-Sn alloy layer was plated on a

50-mm diameter Si semiconductor wafer at 20°C and a current density of 0.6 A/dm^2 in 30 min using a Pt-Ti anode. The alloy contained 20 ±2 wt% Sn.

Sulfite systems

The development of a non-cyanide sulfite Au-Sn alloy plating bath depends on the development of gold sulfite plating baths. In a recent patent [Morrissey 94], it was claimed that in a gold sulfite plating bath containing an organic polyamine, or mixture of polyamines and an aromatic organic nitro compound wherein the pH of the solutions is below about 6.5, tetravalent tin may be added as sodium or potassium stannate. However, no examples or plating results were given about the bath stability and alloy composition in the patent.

2.2 Theory of Electroplating

2.2.1 Electroplating of a single metal

Electrode reaction

The principle components of an electroplating process are shown schematically in Fig. 2.11 [Pletcher 90, Gileadi 93].

The object to be plated is made the cathode in an electrolyte bath. A cathode reaction is

$$M^{n+} + ne^- \rightarrow M \qquad (2.12)$$

where n is the number of electrons a metal ion obtains to reduce to an atom.

In the general case, M^{n+} may be a simple aquo ion such as hygrated Cu^{2+} or it may represent a metal complex such as $[Au(CN)_2]^-$. The most common secondary reaction at the cathode is hydrogen evolution, which has reaction (2.13) in acid solutions and reaction (2.14) in neutral and basic media:

$$2H^+ + 2e^- \rightarrow H_2\uparrow \quad (2.13)$$

$$2H_2O + 2e^- \rightarrow H_2\uparrow + 2OH^- \quad (2.14)$$

The ease of hydrogen evolution depends on the pH of the solution according to the equation

$$E_{(reaction)} = E^0 + (RT/F)\ln(a)$$

where E^0 is the standard potential, R is gas constant, F is faradaic constant, and a is activity, being a_{H^+} and $a_{(OH)^-}$, respectively for Equation (2.13) and (2.14).

Where possible, the preferred anode reaction is the dissolution of the same metal to its precursor in solution.

$$M - ne^- \rightarrow M^{n+} \quad (2.15)$$

When an inert anode is employed, the main anode reaction is oxygen evolution. In an acidic electrolyte, the anode reaction is

$$2H_2O - 4e^- \rightarrow O_2\uparrow + 4H^+ \quad (2.16)$$

while in an alkaline electrolyte, the anode reaction is

$$4OH^- - 4e^- \rightarrow O_2\uparrow + 2H_2O \quad (2.17)$$

The equilibrium electrode potential between a metal and a solution of its ions ($M^{n+} + ne^- \rightarrow M$) is given by the Nernst equation:

$$E = E^0 + (0.059/n)\log(M^{n+}) \quad (2.18)$$

The value of E depends on the concentration of the metal ions to be plated. Addition of

complexing agents can significantly change the concentration of metal ions. The existing theory of deposition from complex ions is that metal is deposited by direct discharge, from the complex ion, without further dissociation of the complex ion to give a metal ion [Gileadi 93, Tan 93]. The metal ion is stripped from its distorted sheath as it passes through the double layer (charged layer at metal solution interface), is neutralized by accepting electrons and deposited on the cathode.

Deposition rate and current efficiency

The averaged rate of deposition may be estimated on a thickness x basis by assuming or measurement of a mass density value ρ for the plated metal:

$$\frac{x}{t} = \frac{\phi i A}{\rho n F} \tag{2.19}$$

where A is the molar mass of metal, i is the current density, and $\phi(\leq 1)$ is the cathode current efficiency for metal deposition. A/nF is traditionally called the 'electrochemical equivalent'. Cathode current efficiency is the proportion of the total cathode current which is used in deposition of the metal concerned. Hydrogen evolution at the cathode will lower the current efficiency.

Overpotential

If a current flows through a cell, the electrode potential deviates from its equilibrium value. The difference between the actual electrode potential and the equillibrium potential is the overpotential η. Activation overpotential refers to the energy needed to move ions across the interface between electrolyte and electrode and to build the discharged atom (adatom) into the crystal structure of the cathode deposit. The current in an activation-controlled process responds to the electrode potential according to the Butler-Volmer equation:

$$i = i_0 \left[\exp\left(\frac{\beta n F}{RT} \eta \right) - \exp\left(-\frac{(1-\beta) n F}{RT} \eta \right) \right] \tag{2.20}$$

where $$i_0 = nFk_0 C \exp\left(\frac{\beta nF}{RT} E_e\right). \quad (2.21)$$

In the above equations, k_0 is a constant; i_0 is the exchange current density; C is the bulk concentration of the metal ions and E_e is the equilibrium potential of the electrode. β is the symmetry factor defined in terms of the ratio between the effect of potential on the electrochemical free energy of activation and its effect on the electrochemical free energy of the reaction. To describe a multi-step process, β must be replaced by an experimental parameter, α, which is called the transfer coefficient.

Equation (2.20) retains a form which emphasizes that the measured current density at a certain overpotential is the sum of the partial cathodic and anodic current densities. When η is very low, say, $\eta<10$ mV, a limiting form of current density can be obtained

$$i = i_0 (nF/RT)\eta \quad (2.22)$$

Equation (2.22) shows that i depends linearly on η. Another limiting form is when $\eta<$ -52 mV and the first term in the Butler-Volmer equation becomes negligible compared with the second. The equation applying to this region can be written as:

$$\log(-i) = \log i_0 - \frac{\beta nF}{2.3RT}\eta \quad (2.23)$$

which is known as the cathodic Tafel equation. Similarly, positive overpotentials greater than 52 mV lead to the anodic Tafel equation. Fig. 2.12 shows a log |i| vs. η curve for a solution and the exchange current density and transfer coefficients are obtained from the intercepts and slopes.

Under the condition of mass transport control, the electrode reaction rate is determined by the diffusion rate of the electroactive species. The concentration of the electroactive species near the cathode is lower than that in the bulk solution. The concentration overpotential is expressed as follows:

$$\eta_c = 2.3(RT/nF) \log (1- i/i_L) \quad (2.24)$$

where i_L is the limiting current density.

A fundamental limiting current density can theoretically be reached if the current density is further raised, resulting in no metal at the cathode surface. But before this point is reached, alternative electrode reactions such as the discharge of hydrogen at the cathode, called hydrogen overpotential, take place. The limiting current i_L that is independent of potential is given by

$$i_L = nFDC^0/\delta \tag{2.25}$$

where D is the diffusion coefficient, C^0 is the bulk concentration, and δ is the Nernst diffusion layer thickness and depends on the diffusion and convection conditions in the bath. In quiescent solutions δ is given by

$$\delta = (\pi Dt)^{1/2} \tag{2.26}$$

and for a rotating-disc electrode, δ is given by

$$\delta = 1.61\nu^{1/6} D^{1/3} w^{-1/2} \tag{2.27}$$

where ν is the kinematic viscosity (=viscosity/density) of the solution and w in radians per second is the angular rotation rate of the electrode.

The essence of mass transport is the quantity δ. Decreasing δ can increase i_L. Stirring the solution will decrease the effective value of δ.

When the process is a mixed control, the activation and mass-transport processes always occur in series and they combine to determine the overall rate. Since current density represents the reaction rate, the reciprocal of the current represents the resistance for the process. The overall resistance is equal to the sum of the resistance of every step in series as follows

$$1/i = 1/i_{ac} + 1/i_L \tag{2.28}$$

where i is the current density under mixed control, i_{ac} is the current density under activation control and i_L is the limiting current density controlled by mass transport. Therefore the smaller of the two current densities dominates the overall current. A general qualitative description of the relationship between current density and potential is shown in Fig. 2.13 [Gileadi 93].

An input of energy is also essential to drive the migration process and leads to a potential drop iR_{cell} (where R_{cell} is the internal resistance of the cell, a function of electrolyte properties, the form of the electrodes and cell design) within the cell. The cell voltage required to observe a current density i in a real cell is given by

$$E_{cell} = E_c - E_a - \Sigma |\eta| - iR_{cell} \qquad (2.29)$$

where E_c and E_a are the equilibrium potentials for the cathode and anode, respectively.

Electrocrystallization

Electrocrystallization has two competing processes: nucleation and grain growth. If a deposition starts on an electrode surface of a different material, that of the object to be plated, the first step will be the formation of nuclei of the new phase and their growth into crystals with the characteristic lattice. Then, once the electrode surface is fully covered by a few atomic layers of this metal, the layer is thickened into a macroscopic deposit. Nucleation is an improbable event and is achieved at an electrode surface by the application of a large overpotential. The nuclei, once formed, grow quite rapidly at comparatively low potentials, and in constant-current operation, the potential will decrease substantially once nucleation has occurred. The growth of the crystals occurs by incorporation of the individual metal atoms into the crystal lattice. Of the sites which are possible in a perfect crystal lattice, incorporation will be most favorable at a kink (where the atom can interact with three neighbors), although some incorporation takes place at edge sites (two neighbors). Adatoms (one neighbor) are likely to diffuse to more favorable sites or to redissolve, although a very small number will expand into new nuclei.

The structure of the growing layer is determined largely by the relative rates of

electron transfer to form an adatom and diffusion of the adatom across the surface into a position in the lattice, and the electrolysis conditions, including bath additives which may radically modify the electrocrystallization process. At low current density, the surface diffusion is fast compared with electron transfer and the adatom is likely to end up in a favored site in the lattice. At higher current densities, surface diffusion is no longer fast compared with electron transfer and further nuclei must form; the layer will be less ordered.

During the thickening stage a key parameter is the current density. At low current densities, surface diffusion is fast compared with electron transfer and both the crystal lattice and structures such as screw dislocations can be well formed. The predominant orientations of surface planes can also be determined using electron diffraction. At high current densities, adatoms no longer reach their equilibrium position in the lattice and nucleation of additional growth centers remains a more frequent event. Hence the lattice formed will be less ordered and macroscale features, such as steps, ridges and polycrystalline block growth become more likely. With further increase in current density, outward growth of the layer becomes of increasing importance and problems arising from mass transport control in solution can arise, e.g., dendrites. Once this form of growth commences, it predominates because of the enhanced rate of mass transport to the tip and the iR drop to the tip is also a minimum as this is the closest point to the anode. A powdered texture usually results in the completely mass-transport-controlled potential region. The way in which the structure depends on current density is summarized in Fig. 2.14.

Underpotential plating

When a metal is deposited on a different metal substrate, cathodic current, corresponding to the metal deposition, may occur at less-negative potentials than the equilibrium potential for the metal in its own solution. This phenomenon is called underpotential deposition. An example of underpotential deposition of lead on gold in a $Pb(ClO_4)_2/HClO_4$ solution is shown in Fig. 2.15 [Gileadi 93]. The area under the peaks UPD-1 and UPD-2 represents the charge corresponding to the deposition of a single monolayer of lead on gold. The equilibrium potential for lead deposition refers to the free

energy change in the reaction

$$Pb^{2+} + 2e \rightarrow Pb\text{-}Pb_{crys} \qquad (2.30)$$

where $Pb\text{-}Pb_{crys}$ means that the lead ion is discharged and becomes part of the lead crystal lattice. The free energy change and the corresponding equilibrium potential refer to the formation of a bond between the deposited lead atom and atoms of the same metal on the surface.

Underpotential deposition can be represented by the reaction

$$Pb^{2+} + 2e + Au_{crys} \rightarrow Pb\text{-}Au_{crys} \qquad (2.31)$$

The fact that lead can be deposited on gold at a less negative potential than on lead shows that the $Pb\text{-}Au_{crys}$ bond is more stable than the $Pb\text{-}Pb_{crys}$ bond. The potential difference has been related to the difference in the electronic work function of the two metals concerned, although this correlation does not always hold strictly. As might be expected, the underpotential deposition peaks occur at different potentials, e.g., UPD-1 and UPD-2, on different crystal faces of the same metal. Bulk deposition of lead on gold (which already has an underpotential deposited layer of lead) starts at a more negative potential than on a lead substrate. The difference is referred to as the crystallization overpotential and related to the difference in crystal lattice dimensions, or perhaps to the difference in surface free energy of gold and lead. Likely the underpotential-deposited layer forms an epitaxial layer (taking on the crystal dimensions of the underlying substrate).

Current distribution near the cathode

In metal deposition the current distribution determines the variation of the deposit thickness on the cathode surface. It is thus closely associated with concepts of practical importance, such as throwing power or leveling.

In electrochemical processes the potential difference across the solution-electrode interface as well as the local current density vary in general along the electrode surface. It is common experience that the current density is usually higher on protruding parts of an

electrode, or at its edges. Potential and current distribution are governed by phenomena related to charge transport in the electrodes and to charge and mass transport in the electrolyte. Therefore, a general theoretical treatment involves the integration of the fundamental equations of mass and charge transport. An illustrative picture of the problem of current distribution can be obtained with a resistance model (Fig. 2.16). R_S is the resistance of the electrolyte and depends on geometric factors and on the specific conductivity of the electrolyte. R_p and R_p' are polarization resistances due to the slowness of the electrode reactions and are given by the slope of the overvoltage-current density curve:

$$R_p = d\eta / di \tag{2.32}$$

Due to very complex mathematical problems, solutions have been obtained mainly for special cases: In a primary current distribution where $R_p << R_S$ and $R_p' << R_S$, the influence of any kind of overpotential at the electrode is neglected and the current density is governed by the anode-cathode distance. In a secondary current distribution where R_S can be neglected, the influence of activation overpotential is taken into account. Consequently the current will be more evenly distributed between the peaks and recesses. This means the influence of overpotentials makes the current distribution more uniform. The transition from these two limiting cases is a tertiary current distribution, which is characterized by a dimensionless number called the Wagner number. The Wagner number is defined as the ratio of the polarization resistance to that of the electrolyte.

$$Wa = \frac{d\eta / di}{\rho_e L} \tag{2.33}$$

where ρ_e is the electrolyte resistivity and L is a characteristic length for the system. The characteristic length may be the length of the electrode being plated, the spacing between the cathode and anode, or the dimension of the irregularity of the cathode surface to be plated. In practice, a system is said to be under primary current distribution if $Wa<0.1$ and under secondary current distribution if $Wa>10$.

From the schematic current-voltage curve shown in Fig. 2.12, in the linear Tafel region where the reaction takes place under activation control, the current –voltage relation is

$$\eta_a \propto \log i \tag{2.34}$$

Then the polarization `resistance is

$$(d\eta_a/di) \propto i^{-1} \tag{2.35}$$

The secondary current distribution tends to become less uniform at higher current density. However, at higher overpotentials we have

$$\eta_c \propto \log(1-i/i_L) \tag{2.36}$$

Its derivative increases with i for a given limiting current density i_L:

$$(d\eta_C/di) \propto (1- i/i_L)^{-1} \tag{2.37}$$

Equation (2.37) shows that the exchange current density has no effect on the current distribution in this region, which is unreasonable. Therefore a modified Wagner number is given by replacing the differential polarization resistance ($d\eta/di$) by the integral resistance (η/i). Then the Wagner number is proportional to $-\log i_0$ in the linear Tafel region. Since the deposition reaction is controlled by mass transport, the tertiary current distribution depends mainly on the uniformity of the diffusion layer thickness. The diffusion layer thickness grows initially with the square root of time and reaches steady state after a short time compared to the time of plating. Typical values of diffusion layer thickness may range from 10 - 50μm. Geometrical influences and hydrodynamics are therefore involved in tertiary current distribution. There are two distinguished cases as far as geometrical factors are concerned. One is when the characteristic dimension of a cathode surface h is smaller than the thickness of the diffusion layer, which is called a

microprofile (Fig. 2.17a). The peaks are more accessible to diffusion than the recesses due to a peak effect analogous to that in the primary distribution. The microscopic throwing power is poor. The other case is when the characteristic dimension of a cathode surface h is larger than the thickness of the diffusion layer, which is called a macroprofile (Fig. 2.17b). In this figure a constant thickness of the diffusion layer is considered and a perfect geometric throwing power at the limiting current is achieved, where the deposit follows the profile of the substrate surface. The diffusion layer thickness can vary along a macroprofile not for geometrical but for hydrodynamic reasons.

The macrothrowing power of a bath is a measure of its ability to produce electroplated coatings of uniform thickness on samples having complex geometries. The characteristic length, L, can be chosen as the difference between the shortest and the longest distance between the two electrodes, and L is on the order of several millimeters to several centimeters. A quantitative measure of this property can be defined in terms of the so-called Haring and Blum cell shown in Fig. 2.18. The throwing power (T. P.) is defined as:

$$T.P. = \left[\frac{K - M}{K}\right] \times 100 \qquad (2.38)$$

where K is the ratio of distances between the anode and the two cathodes (taken as 5) and M is the ratio of coating thickness on the two cathodes. Based on above discussion about current distribution, increasing the conductivity of the solution, and decreasing the exchange current density i_0 by using complexed metal ions, can obviously improve the throwing power. Generally, hydrogen evolution can increase the throwing power if the current efficiency of the metal plating decreases with increasing current density. Electrodeposition of a metal from a negative complex ion can also influence the throwing power in other ways. Where the local current density is higher, the potential on the solution side of the interface is more negative; this causes a local decrease in the concentration of the negative ions, which slows the reactions.

When the appearance of the surface, particularly its brightness, is considered, the characteristic length is on the order of magnitude of the wavelength of visible light,

namely, in the range of 0.4 - 0.8μm. The ability of a plating bath to form uniform coatings on this scale of roughness is called microthrowing power. It is also referred to as leveling. A poor microthrowing power means that the deposit layer may be thicker over the peaks than in the valleys (Fig. 2.19a). The reverse case is known as leveling (Fig. 2.19b), where the deposit is thicker in the valleys than on the peaks and the deposits are smoother than the original work. In electroplating, roughness of the deposit usually increases with thickness because of a positive feedback mechanism when the plating process is at least partially controlled by mass transport.

Additives in a plating system play a vital role in producing smooth and bright deposits, which is of great commercial interest. The mechanism by which they operate is easy to understand. Molecules of the additive adsorbed on the surface prevent or inhibit metal deposition. The rate of metal deposition is approximately proportional to $(1-\theta)$, where θ is the fractional surface coverage by molecules of the additive. Generally the concentration of the additive is small and the rate of adsorption is diffusion controlled. Therefore the leveling effect occurs because of lower fractional coverage in recessed areas. There is an optimum range of concentration over which each additive is most active. At very low concentrations when there is hardly any coverage anywhere, additives do not work. Neither do they work in concentrated solutions, where coverage everywhere is at their saturation value during plating. Colloids, such as bone or hide glue, are a common type of additive for Sn plating.

2.2.2 Electroplating of metal alloys

A wide variety of binary and ternary alloy coatings are produced industrially by electrodeposition, the most important being zinc alloys, tin alloys, nickel alloys and noble metal alloys. As pointed out by Brenner [Brenner 63], the composition of electrodeposited alloys depends on many factors and differs from that of the electrolyte. Brenner distinguishes 'normal' and 'abnormal' codeposition behavior. In the first case, the relative proportions of the metals in the electrodeposited alloy can be qualitatively determined on the basis of the equilibrium potentials of the metals against the solution.

Normal codeposition is further subdivided into 'regular' codeposition (diffusion control), 'irregular' codeposition (activation control) and 'equilibrium' codeposition. In abnormal codeposition, according to Brenner, the deposit composition differs from that expected from equilibrium considerations. This type of behavior includes 'anomalous' and 'induced' codeposition. In anomalous codeposition the less noble component deposits preferentially and its relative concentration in the alloy is higher than in the electrolyte. Induced codeposition means that a given element can be codeposited to form an alloy, but cannot be deposited in pure form. W and Mo are examples. Brenner's classification is based essentially on thermodynamic considerations. It does not sufficiently take into account charge transfer kinetics and mass transport.

An approach based on mixed potential theory was proposed first by Wagner and Traud [Wagner 38], and developed by Landolt [Landolt 94]. The mixed potential theory states that the measured current in an electrochemical system is equal to the sum of the partial anodic and cathodic currents. Thus, the chemical composition of an alloy will generally depend as much on kinetics as on thermodynamic quantities. Following Tafel kinetics, the logarithm of the ratio of cathodic partial current densities for two species A and B is given by Equation (2.39).

$$\ln(i_A/i_B) = R_0 - (s_{c,A} - s_{c,B})\, E \qquad (2.39)$$

$$R_0 = \ln (i_{0,A} /i_{0,B}) + (s_{c,A}\, E_{rev,A} - s_{c,B}\, E_{rev,B}). \qquad (2.40)$$

Here $s_{c,j}$ is the inverse of the cathodic Tafel coefficient and $i_{0,j}$ is the exchange current density. Equation (2.39) demonstrates that a potential independent alloy composition is obtained only if $s_{c,A} = s_{c,B}$. The importance of the exchange current density ratio is illustrated by Equation (2.40). This explains that a less noble metal A may deposit more readily than a more noble metal B if the exchange current density of the latter is small. Fig. 2.20 schematically illustrates four possible situations where a thermodynamically less noble component A deposits preferentially in a given potential range indicated by the gray zone in the figure.

In alloy plating, because of possible interactions between partial reactions, it may not

simply be assumed that the behavior of the mixed system can be predicted from a knowledge of the individual kinetics of the components. There are three distinguished types of codeposition behavior: non-interactive codeposition, charge transfer coupled codeposition and mass transport coupled codeposition.

In non-interactive systems, the alloy composition can be predicted from the kinetics of the pure metals. Ni-Cu alloys and Sn-Pb alloys correspond to this behavior. The partial current densities of Cu and Ni for a citrate electrolyte containing an excess of Ni and only a small concentration of Cu are schematically presented in Fig. 2.21. It indicates that Ni deposition and dissolution is charge transfer controlled, while Cu deposition is mass transfer controlled. At the open circuit the overall current density i is zero. However, because Cu is nobler than Ni, a displacement reaction may occur leading to selective Ni dissolution and corresponding Cu deposition. The rate of selective Ni dissolution is expected to be equal to the limiting current for copper deposition.

For charge-transfer-coupled systems the value of the partial current of a given alloy component differs from that observed during deposition of the component in its pure state. For example, during deposition of a Zn-Ni alloy from a sulfate electrolyte the deposition rate of Ni is slowed down drastically by the presence of Zn. The partial current density for Ni during alloy deposition is much lower than the current density measured during deposition of the pure metal. This result might be related to competitive adsorption of reaction intermediates influencing the surface coverage of Ni. In some cases, a given metal may have a catalytic effect on a codepositing alloy component. Ni-Mo alloy plating from a citrate electrolyte is such an example. Alloys of quite high molybdenum content (~50%) can be produced, in spite of the fact that pure Mo cannot be deposited from aqueous solution. Some authors [Chassaing 89] proposed that deposition involves a mixed Ni-Mo oxide intermediate which permits Mo reduction.

Mass-transport-coupled codeposition refers to situations where the rate of codeposition of a given alloy component depends on the mass transport of a species being consumed or produced at the cathode due to codeposition of another component. For example, concurrent hydrogen formation can lead to an increase of pH in the cathodic diffusion layer which may change metal deposition kinetics. The extent of depletion of H^+ or accumulation of OH^- depends on mass transport conditions and on the buffering

capacity of the electrolyte. A change in local pH can influence the relative deposition rate of alloy components and hence the resulting alloy composition. Another example is that cations of different components may compete for the same ligands to form complexes. So far no systematic study of coupling effects has been undertaken.

2.2.3 Pulse plating

2.2.3.1 Pulse plating of a single metal

The application of pulsed electrolysis to the electroplating of pure metals and alloys has attracted considerable attention since the early 1970s. Typical waveforms are shown in Fig. 2.22 [Puipe 86]. It has been claimed that pulse plating can be used for the purpose of improvement of deposit porosity, electrical conductivity, roughness, ductility and deposition of alloys with compositions and structures not obtainable with DC plating. Therefore, pulse plating allows the use of simpler solutions and fewer additives.

Studies on pulse plating are making a useful contribution to the scientific basis of electroplating. Cheh [Cheh 71] defined the concept of limiting current density and adopted a Nernst diffusion model to estimate the rate of mass transfer in pulse and periodic reverse plating. Ibl [Ibl 80] developed approximate models to describe the pulsating diffusion layer. Cheh *et al.* [Cheh 83] reported their investigation on both theoretical modeling and experimental studies in complex plating systems which include processes with gas evolution and alloy deposition. More recently, mathematical models for periodic electrodeposition of multicomponent alloys have been developed, taking into consideration transient, convective mass transfer to a rotating disk electrode, Butler-Volmer kinetics and individual component activities in the electrodeposits [Verbrugge 85, Ruffoni 88, Schultz 98].

Charging and discharging of electrical double layer in pulse plating

Charging and discharging times of the double layer are a function of a number of electrical parameters, including the exchange current density, capacitance, and pulse

current density. The total applied current i, in a transient process is a sum of the nonfaradic i_C and the faradic current i_F. i_C is responsible for the charging and discharging the electrical double layer, and i_F represents the rate of the electrochemical reaction. For a transient process of the electrical double layer with capacitance of C,

$$i_C = C\, d\eta / dt \tag{2.41}$$

Since a constant-current pulse is considered, $di_t = 0$ and $di_F = -di_C$, where i_t is the total current density. Assuming that the entire current is capacitive until the double layer is charged, then the charging time

$$t_C^{*} = C\eta_{a\infty} / i_p \tag{2.42}$$

where $\eta_{a\infty}$ is the steady state overpotential. If the charging time is the time needed to increase the potential η_a to 98.2 percent of $\eta_{a\infty}$, then for a resistance R_a and capacity C in parallel,

$$t_C^{**} = 4\, R_a C \tag{2.43}$$

Mass transport

Mass transport limits the maximum rate of deposition. For mass transport in pulse plating, the most important quantity is the pulse-limiting current density i_p. It plays a similar role as the limiting current density in DC electrolysis.

In a single current step, the constant current density is higher than the steady-state-limiting current density. A constant gradient is imposed at the cathode according to Equation (2.44) and the surface concentration of the reacting species decreases with time until it reaches zero at $t = \tau$. Fig. 2.23(a) shows qualitatively the expected behavior. The time is called the transition time. It manifests itself experimentally by a sudden increase in the electrode potential which leads to the onset of an additional cathodic discharge reaction such as hydrogen evolution. For $t > \tau$, the part of the total current which is carried

by reaction of the metal diminishes because the gradient at the electrode surface decreases. Eventually it reaches the steady state value for DC:

$$i = -nFD\,(dC/dx)_{x=0} \qquad (2.44)$$

The situation is quite different in a single potential step. The electrode potential fixes the surface concentration of the reacting species which, therefore, is constant. This leads to very high initial concentration gradients at the cathode, but as the region near the surface becomes depleted, the gradient and hence the current density decreases and eventually reaches a steady state as shown in Fig. 2.23(b). If the applied potential was less negative than that necessary to reach zero concentration at the surface, a finite surface concentration value C would be established and the steady state current at infinitely long times would be below the DC limiting current.

The mathematical treatment of the described behavior involves solving Fick's second law of diffusion within the Nernst diffusion layer:

$$\frac{\partial C}{\partial t} = D\frac{\partial^2 C}{\partial x^2} \qquad (2.45)$$

Solving the equation with boundary conditions, one gets for general cases $(D\tau/\delta^2)<0.1$,

$$\tau\, i^2 = (\pi D n^2 F^2/4)C^2 \qquad (2.46)$$

Pulse-limiting current density

The most important quantity is the pulse-limiting current density i_{Lp} at which the surface concentration reaches zero at the end of a pulse. This definition implies that the value of i_{Lp} depends on the choice of pulse parameters. The mathematical calculation of i_{Lp} involves solving equation (2.45) with the boundary conditions where a number of pulses are applied. It has been shown that after only a few current pulses the concentration fluctuations at the cathode become independent of the number of pulses

applied. A simple approximate model of the mass transport processes in constant-current pulse electrolysis was developed by Ibl [Ibl 80]. In the model, the diffusion layer is considered to consist of a pulsating and a stationary part as shown in Fig. 2.24. Assuming linear concentration profiles in each part one obtains

$$\delta_P = \sqrt{\frac{4}{\pi} D t_{ON} (1-\gamma)} \tag{2.47}$$

and

$$i_{LP} = i_L \left[\sqrt{\frac{4}{\pi} \frac{D t_{ON}}{\delta^2}} (1-\gamma)^{1.5} + \gamma \right]^{-1} \tag{2.48}$$

where δ_p is the thickness of the pulsating diffusion layer, γ is the duty cycle given by equation (2.49) and t_{ON} and t_{OFF} are the pulse time and OFF time.

$$\gamma = \frac{t_{ON}}{t_{ON} + t_{OFF}} \tag{2.49}$$

The average limiting current density in pulse plating is given by

$$i_{Lm} = \gamma\, i_{Lp} \tag{2.50}$$

2.2.3.2 Periodic reverse-current plating (PRC)

There have been claims that PRC plating can improve deposit thickness distribution and reduce internal stress by periodic inversion of polarity [Puipe 86]. The square wave ratio of forward-to-reverse current was about 30:1. For Au-Sn PRC plating, Sn will be apparently dissolved preferentially.

The advantages include polarization effects that are at least partially reduced, bath impurities which may have attached themselves to the plated surface are dislodged, and

electropolishing conditions may be established. However, periodic reverse current plating is also subject to lower current efficiencies, if forward-to-reverse current ratios are not kept high.

Table 2.1 Properties of several solder materials [Tan 96].

Solder alloy	$T_{melting}$ (°C)	Young's Modulus (GPa)	CTE (10^{-6}/ °C)	Poisson's ratio	Relative fatigue life*1	Relative creep rate*2
63Sn-37Pb Eutectic	183	30	21	0.4	10	2
90Pb-10Sn	268	20	29	0.4	1	1
95Pb-5Sn	310	24	26	0.37	1	0.5
80Au-20Sn Eutectic	281	68	~14	0.4	Poor	No creep
50In-50Pb	180		27		3	0.5
100In	157	7	31	0.46	20	Soft
97Sn-3Cu	227	41	19	0.33	5	0.01

*1 and *2: the fatigue life and creep rate related to 90Pb-10Sn solder alloy.

Table 2.2 An overview of the basic difference between several bonding technologies [Kallmayer 95].

	Vapor phase	IR-heating	Pulse heated thermode
Atmosphere	Inert	Active	N_2 or forming gas possible
Self-alignment	Yes	Yes	No
Equipment costs	Low	Medium	High
Temperature distribution	Constant	Fast heating	Very fast heating
Heat transfer	Condensation	Radiation	Heat conduction
Batch process	Yes	Yes	No (Single chip)

Table 2.3. Stability constants β_2 and β_4 for gold (I) complexes and gold (III) complexes, respectively [Stanley 87].

Gold (I)	β_2	Gold (III)	β_4
$Au(CN)_2^-$	2×10^{38}	$Au(CN)_4^-$	$\sim10^{56}$
$Au(S_2O_3)_2^{3-}$	5×10^{28}	AuI_4^-	5×10^{47}
$Au(CS(NH_2)_2)_2^+$	2×10^{23}	$Au(SCN)_4^-$	10^{42}
AuI_2^-	4×10^{19}	$AuBr_4^-$	10^{32}
$Au(SCN)_2^-$	1.3×10^{17}	$AuCl_4^-$	10^{26}
$AuBr_2^-$	10^{12}		
$[Au(SO_3)_2]^{3-}$	10^{10}		
$AuCl_2^-$	10^9		

Table 2.4 An alkaline sulfite Au plating bath [Gemmler 94].

Temperature	47 ±1°C
pH	9.0 ± 0.2
Current density	0.25 - 0.3 A/dm^2
Anode material	Platinated titanium
Plating rate	0.16 – 0.18 μm/hr (at 0.3 A/dm^2)
Agitation mode	Mechanical stirring
Gold (I) cyanide	10 ± 1 g/L
Leveller/Grain refiner	1.5 – 3.5 mg/L
Sulfite	26 g/L
Sulfate	21 g/L
Chloride	1.7 g/L
EDTA	15 g/L

Table 2.5 The basic composition and operating conditions of a gold (I) thiosulfate-sulfite bath [Osaka 97].

Chemicals	Concentration
$NaAuCl_4.2H_2O$	0.06M
Na_2SO_3	0.42M
$Na_2S_2O_3.5H_2O$	0.42M
Na_2HPO_4	0.30M
pH	6.0
Temperature	60°C
Current density	$5mA/cm^2$
RDE rotation speed	500 rpm

Table 2.6 Solution and plating conditions of an acidic cyanide gold-tin plating bath [Kuhn 95].

Solution formula	K dicyanoaurate	~20 g/L
	$SnCl_4.5H_2O$	~30 g/L
	KOH	10 g/L
	K D-gluconate	6 g/L
	Citric acid	10 g/L
	K citrate	50 g/L
	Piperazine	4 g/L
	As_2O_3	20 mg/L
Plating conditions	Anode	Platinized Titanium
	pH	4
	Temperature	45°C
	Current density	$2 A/dm^2$

Table 2.7 Standard reduction potentials for various reactions involving gold [Stanley 87].

Reaction	E° (V)
$Au^- + e = Au$	1.69
$AuCl_2^- + e = Au + 2Cl^-$	1.154
$Au(SCN)_2^- + e = Au + 2SCN^-$	0.662
$Au(CS(NH_2)_2)_2^- + e = Au + 2CS(NH_2)_2$	0.352
$Au(S_2O_3)_2^{3-} + e = Au + 2S_2O_3^{2-}$	0.15
$Au(CN)_2^- + e = Au + 2CN^-$	-0.57
$Au^{3-} + 3e = Au$	1.50
$AuCl_4^- + 3e = Au + 4Cl^-$	1.002
$Au(SCN)_4^- + 3e = Au + 4SCN^-$	0.623
$Au^{3-} + 2e = Au^-$	1.40
$Au(SCN)_4^- + 2e = Au(SCN)_2^- + 2SCN^-$	0.604
$AuCl_4^- + 2e = AuCl_2^- + 2Cl^-$	0.926

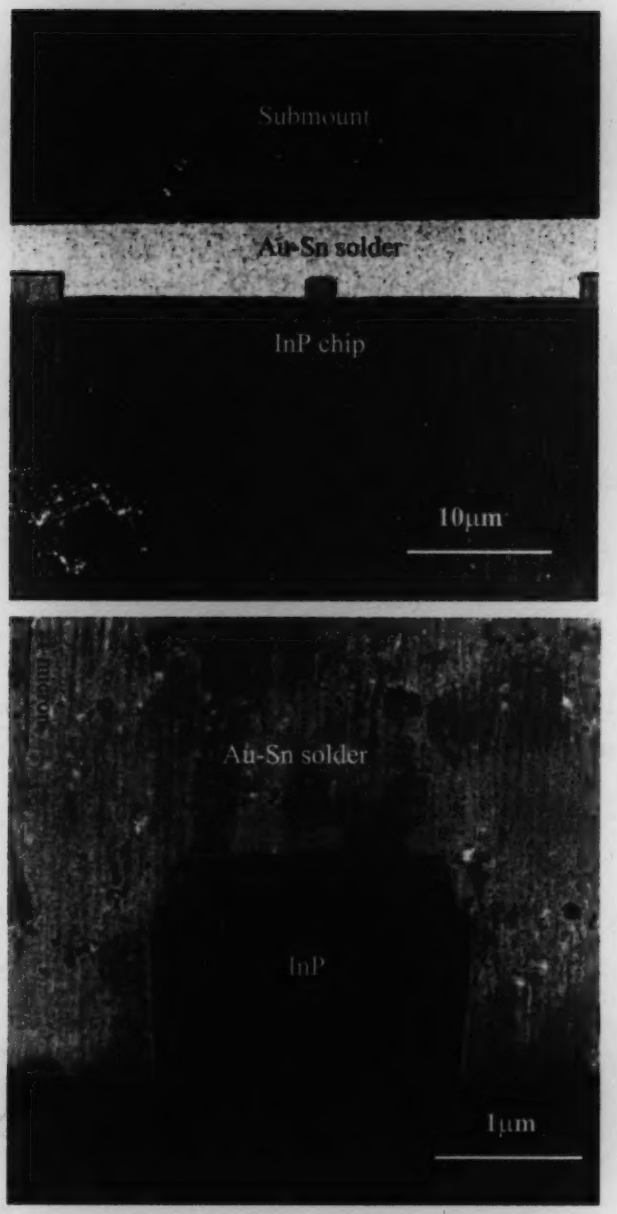

Fig. 2.1 Au-Sn eutectic solder for InP laser bonding [Ivey 98].

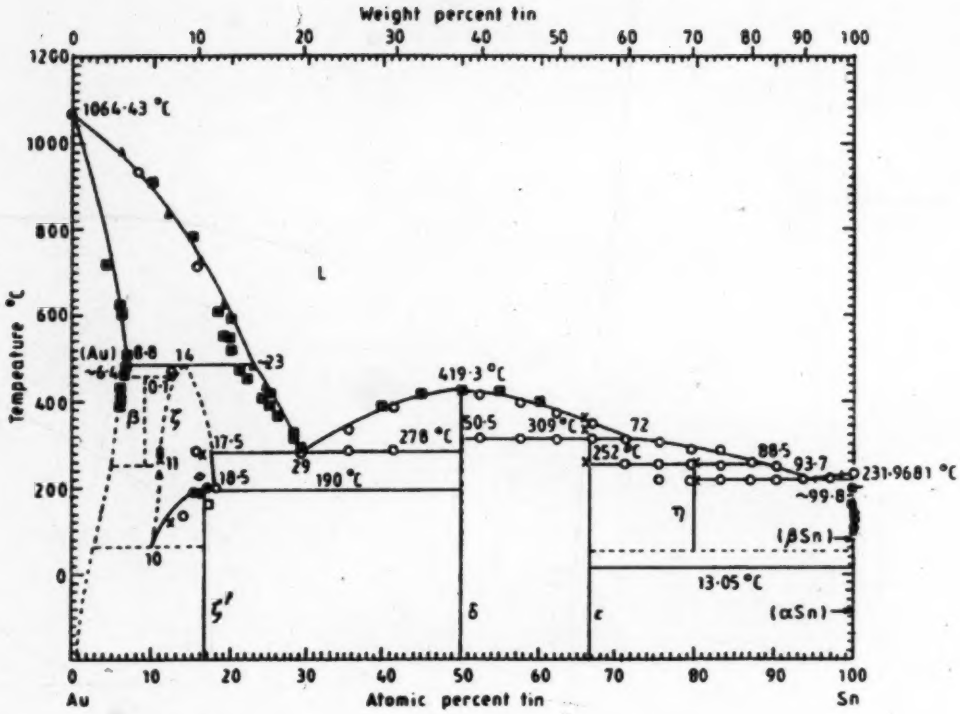

(a)

Fig. 2.2 Au-Sn phase diagram (a) and (b) Au-rich portion of the Au-Sn diagram [Matijasevic 93] (to be continued).

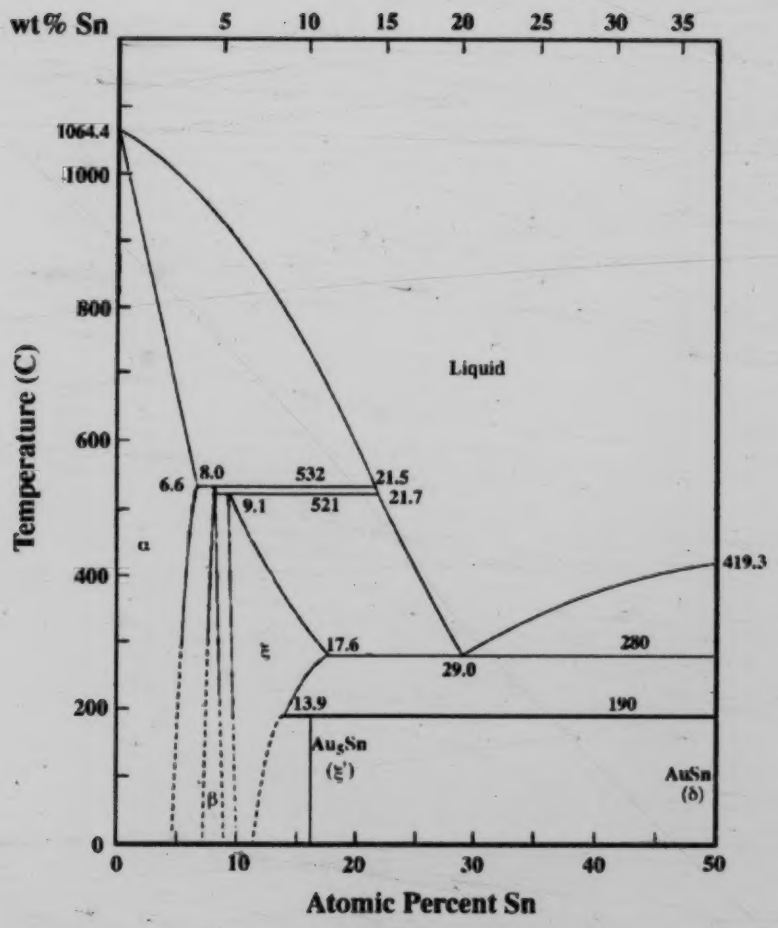

(b)

Fig. 2.2 Au-Sn phase diagram (a) and (b) Au-rich portion of the Au-Sn diagram [Matijasevic 93].

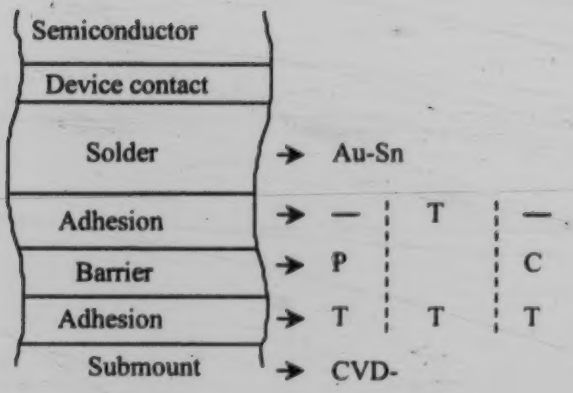

Fig. 2.3 A schematic presentation of theconceptual design of a bonded device [Katz 94-1].

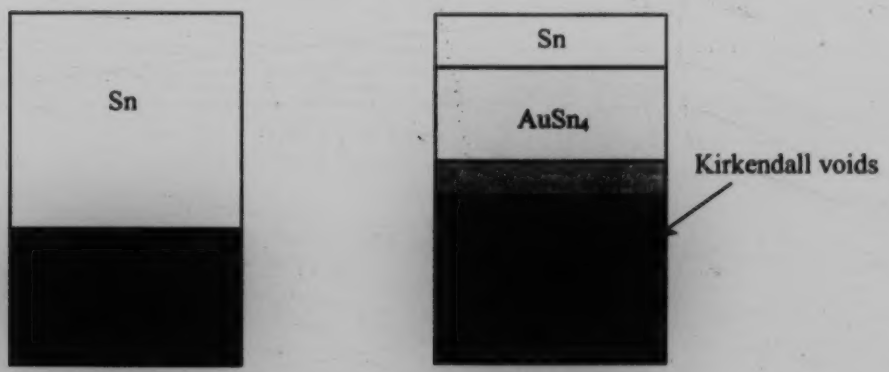

Fig. 2.4 Schematic of intermetallic compound formation and Kirkendall void formation in Au-Sn solder [Zakel 95-2].

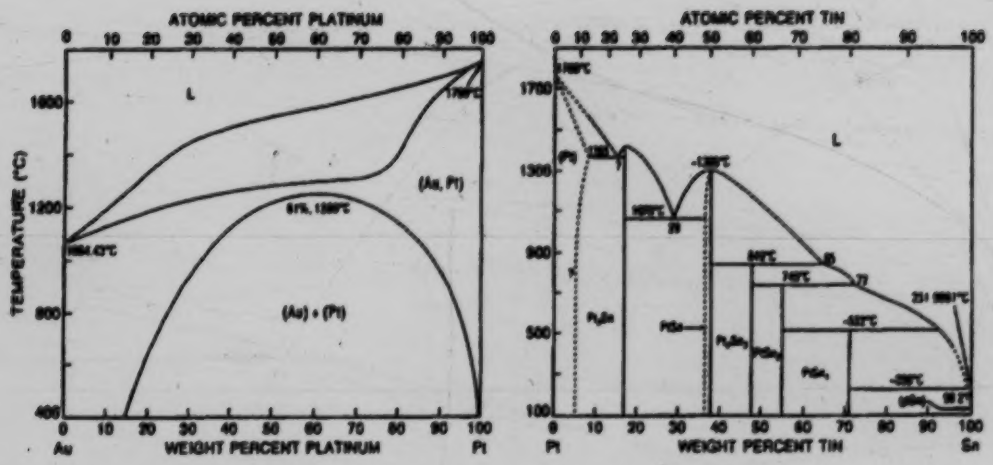

(a) (b)

Fig. 2.5 Binary phase diagram of Pt-Au (a) and Pt-Sn (b) [Katz 94-1].

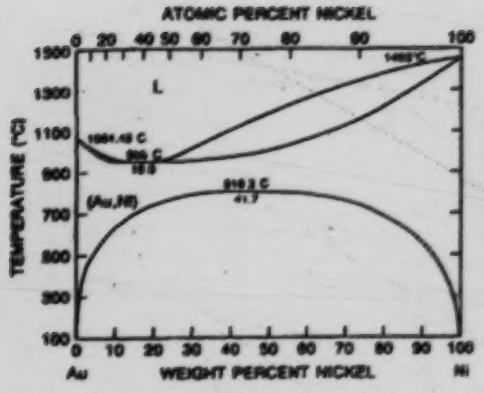

(a)

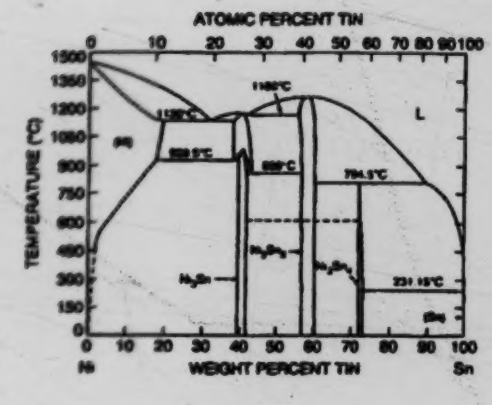

(b)

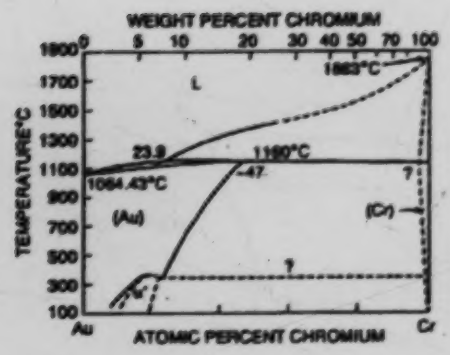

(c)

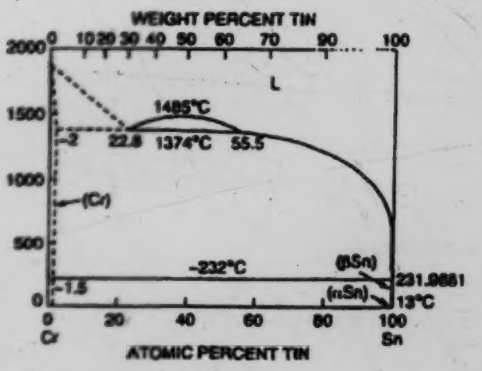

(d)

Fig. 2.6 (a) Au-Ni, (b) Ni-Sn, (c) Au-Cr, (d) Cr-Sn, and (e) Au-W phase diagram [Katz 94-1] (to be continued).

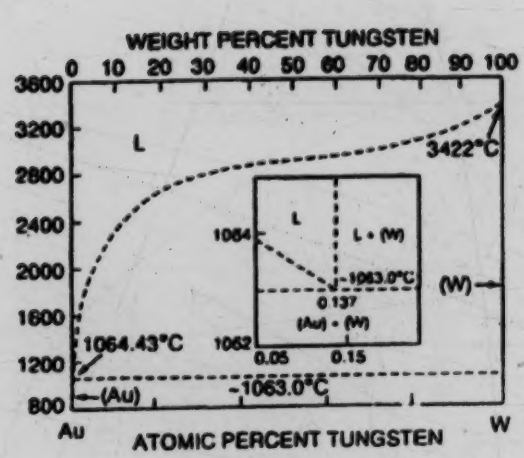

(e)

Fig. 2.6 (a) Au-Ni, (b) Ni-Sn, (c) Au-Cr, (d) Cr-Sn, and (e) Au-W phase diagram [Katz 94-1].

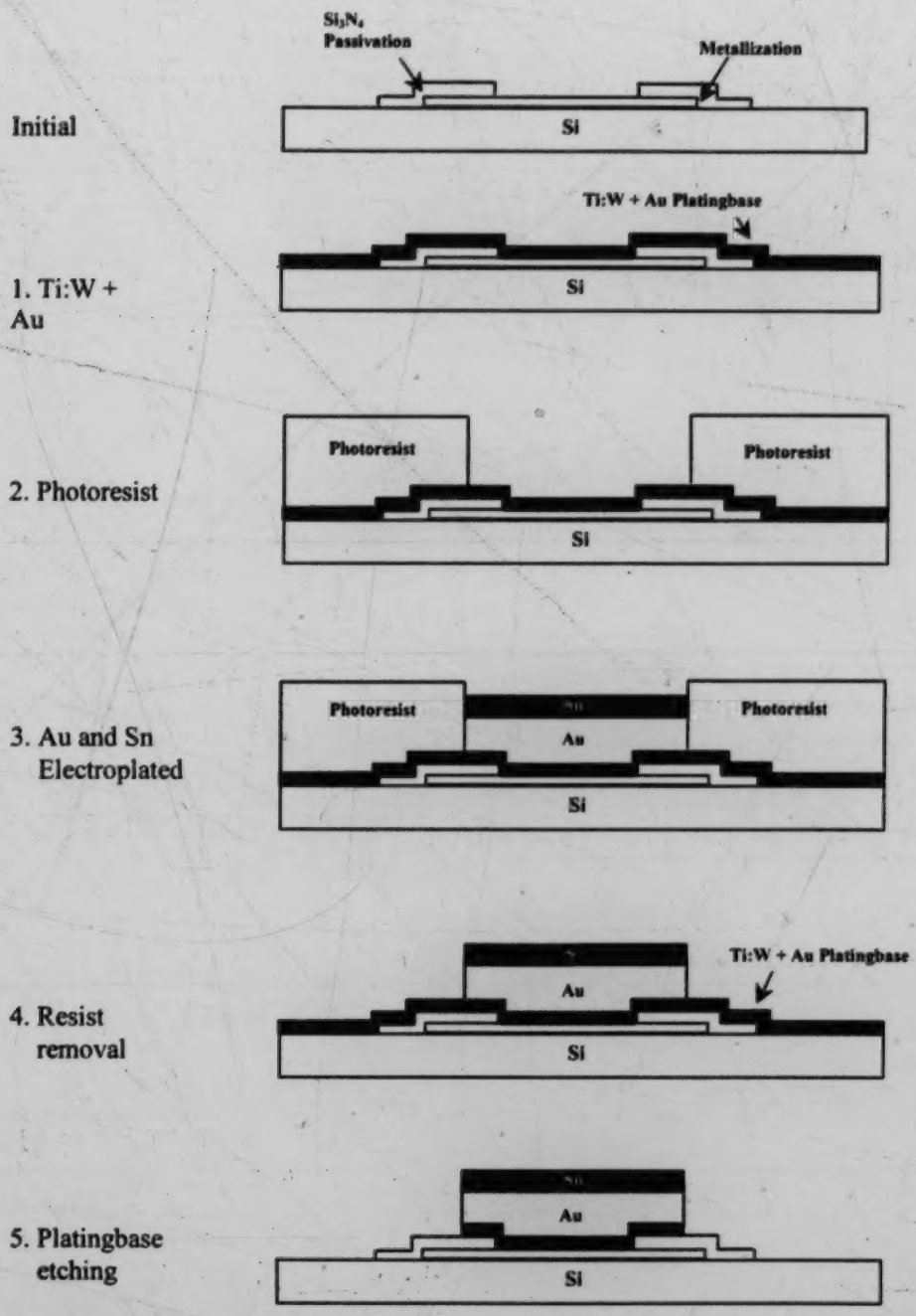

Fig. 2.7 Flow chart of bumping process by sequential electroplating of Au-Sn [Kallmayer 95-1].

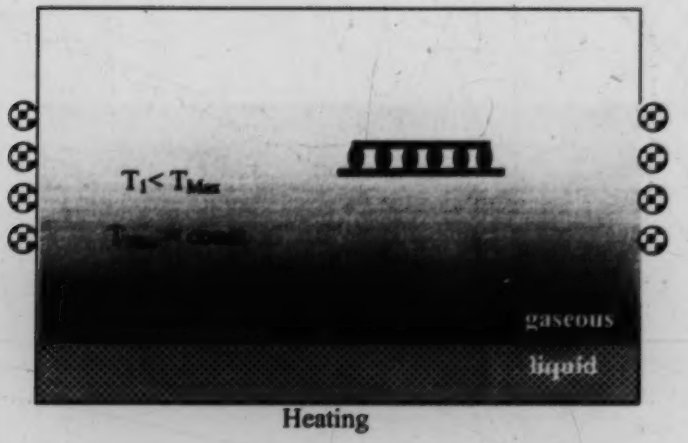

Fig. 2.8 Schematic showing vapor phase flow [Kallmayer 95-1].

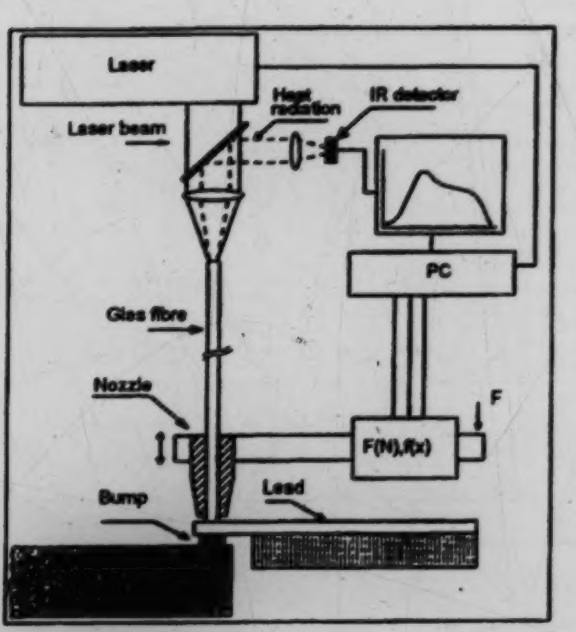

Fig. 2.9 Schematic of laser bonding [Azdasht 94].

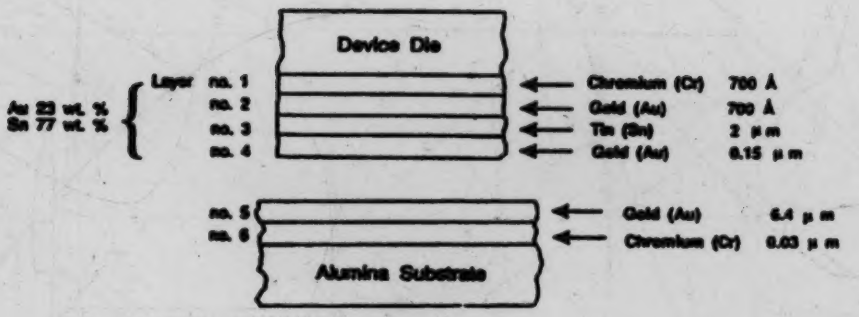

Fig. 2.10 Schematic of low temperature diffusion bonding [Lee 92-1].

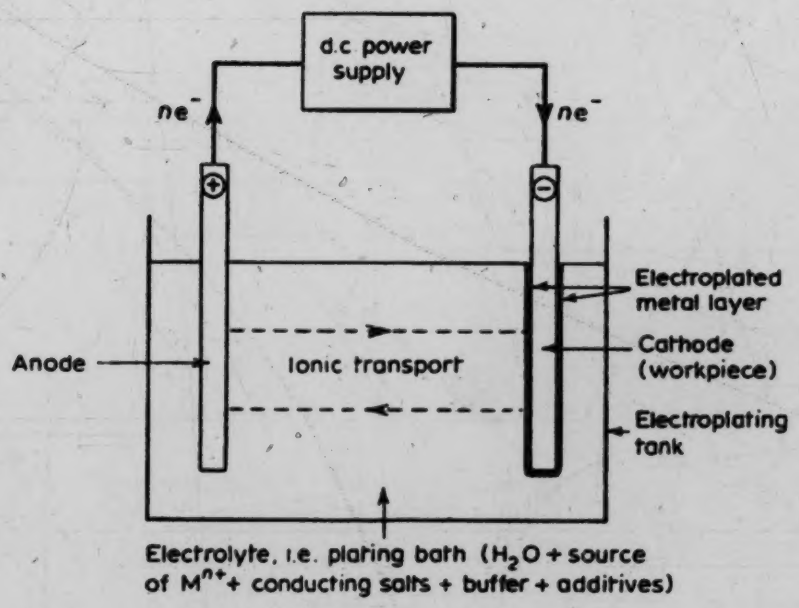

Fig. 2.11 The principal components of an electroplating process [Pletcher 90].

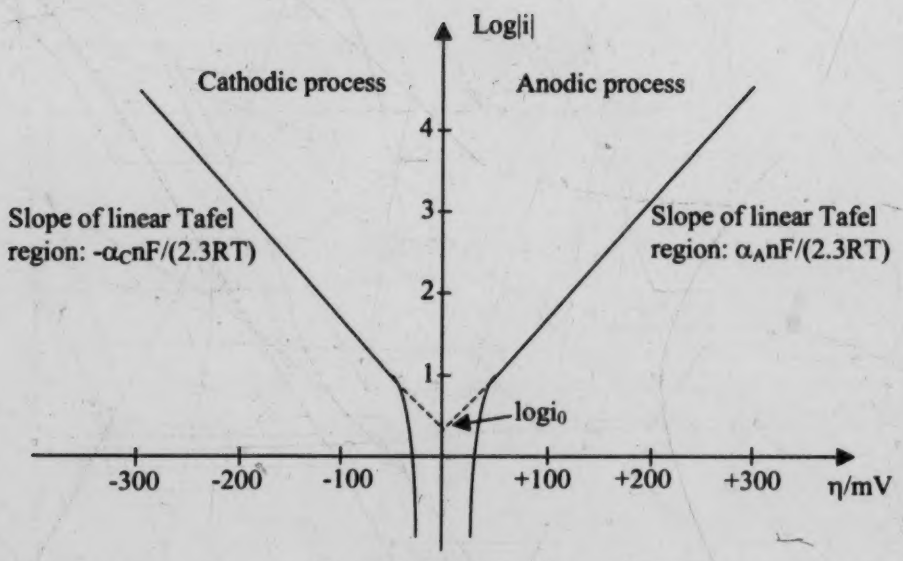

Fig. 2.12 Plot of log|i| vs. η.

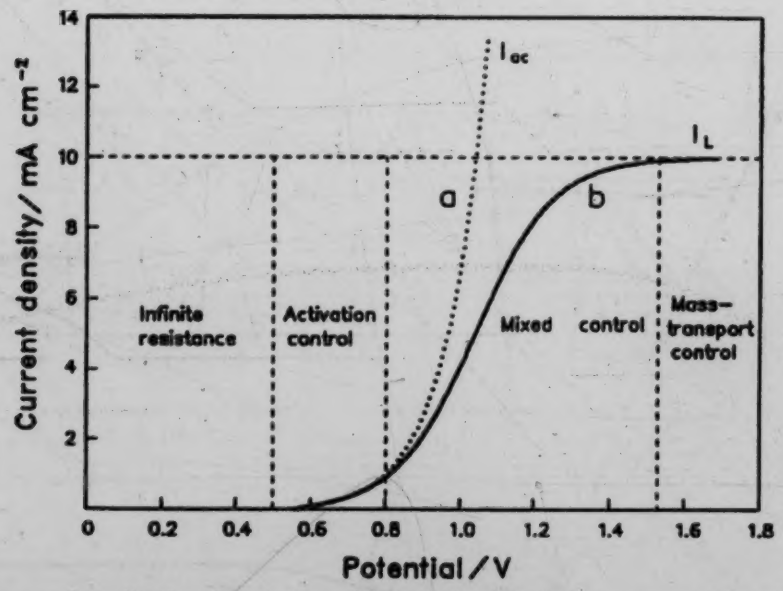

Fig. 2.13 A general qualitative description of the relationship between current density and potential. Line **a** is the purely activation-controlled current I_{ac}, line **b** is the actual current which will be measured, having a mass-transport-limited value I_L [Gileadi 93].

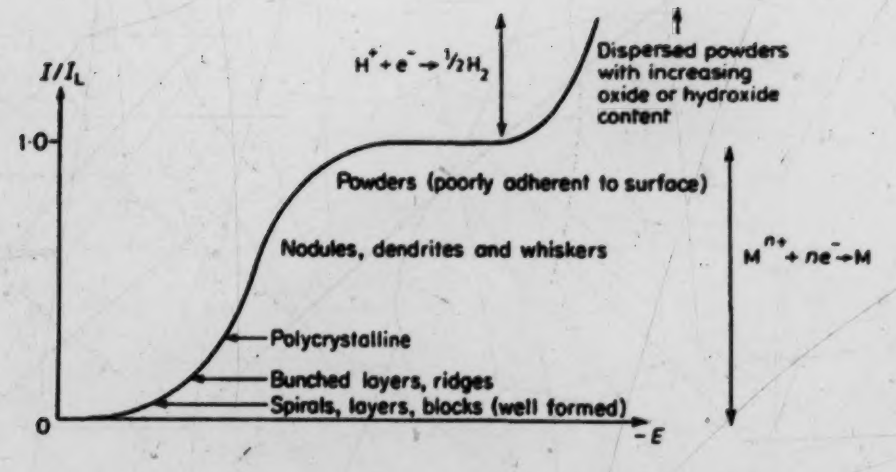

Fig. 2.14 Microstructure dependence on current density.

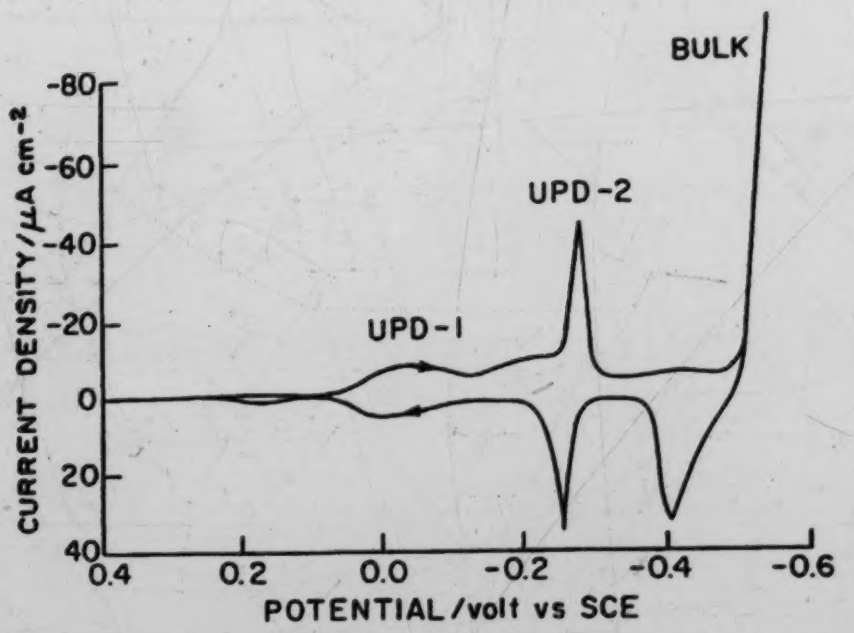

Fig. 2.15 Underpotential deposition of lead on gold from a solution of 1.0 mM $Pb(ClO_4)_2$ in 1.0 M $HClO_4$. Two underpotential deposition (UPD) and dissolution peaks are shown [Gileadi 93].

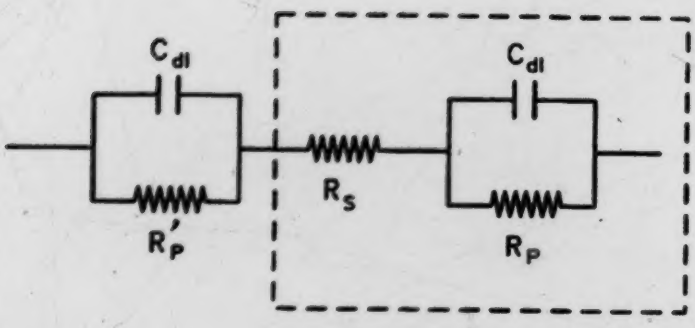

Fig. 2.16 Equivalent circuit for a two-electrode cell. A single interface is usually represented by the elements inside the dashed rectangle. C_{dl}, R_P and R_S represent the double-layer capacitance, the polarization resistance and the solution resistance, respectively.

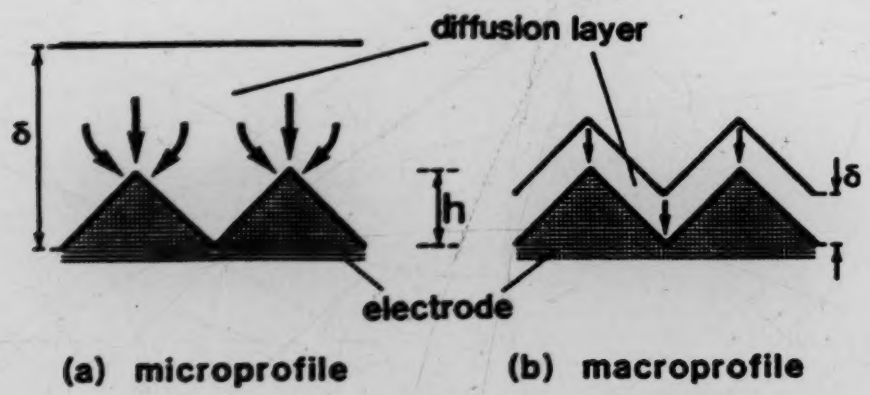

Fig. 2.17 Influence of diffusion layer thickness on tertiary current distribution. (a) microprofile: the crests are privileged from the point of view of diffusion, (b) macroprofile: the current density is uniformly distributed [Puipe 86].

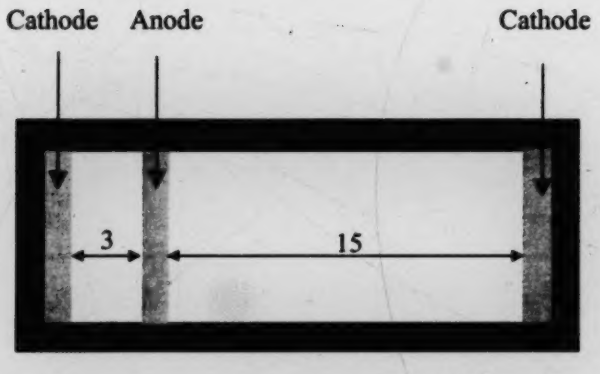

Fig. 2.18 Haring and Blum cell for throwing power testing.

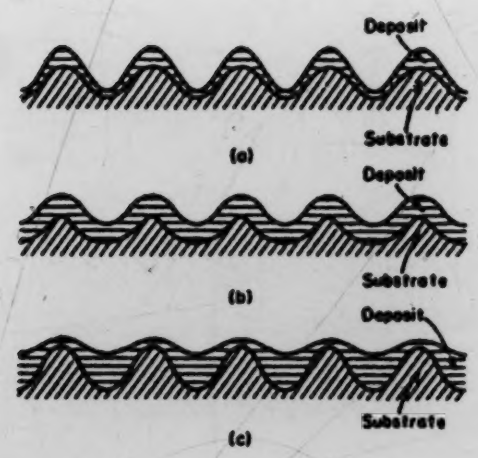

Fig. 2.19 Microthrowing power and levelling. (a) Poor microthrowing power; (b) geometric microthrowing power; (c) true levelling [Tan 93].

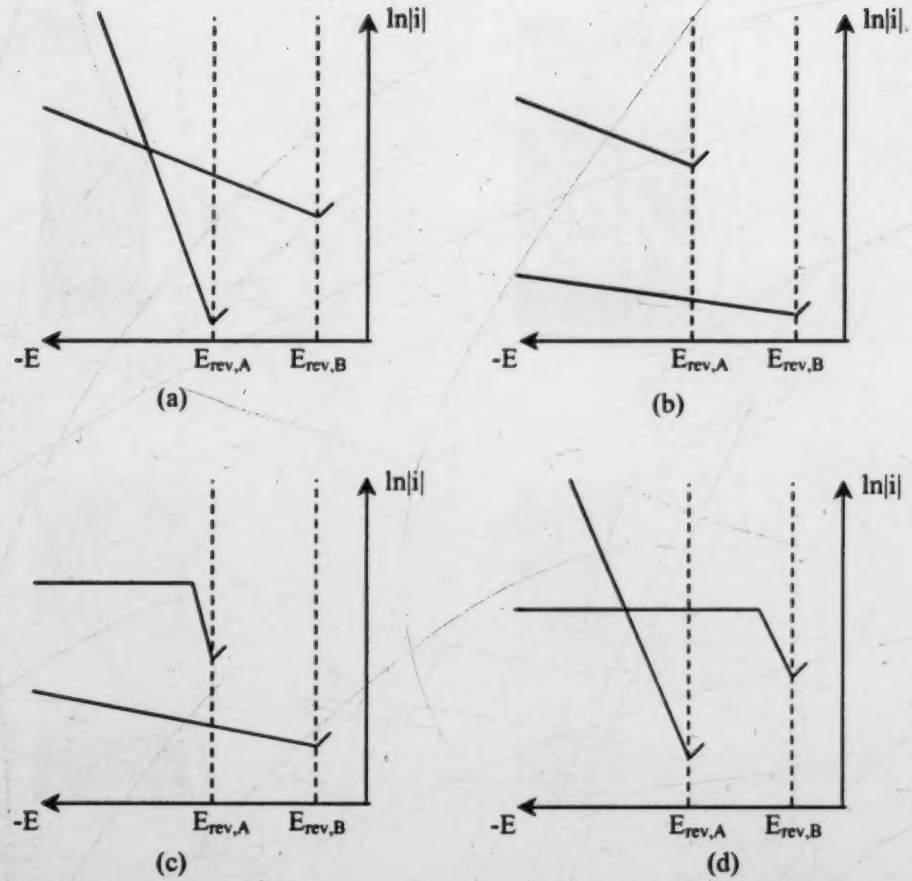

Fig. 2.20 Evans diagrams representing the partial currents of alloy components A and B for anomalous codeposition of a binary alloy AB. $E_{rev,A}$ and $E_{rev,B}$ represent the equilibrium potentials of the components. Figures (a) and (b): both partial reactions are charge transfer controlled. Figures (c) and (d): one of the partial reactions is mass transport controlled. The hashed area represents the potential range leading to preferential deposition of the less noble component A [Landolt 94].

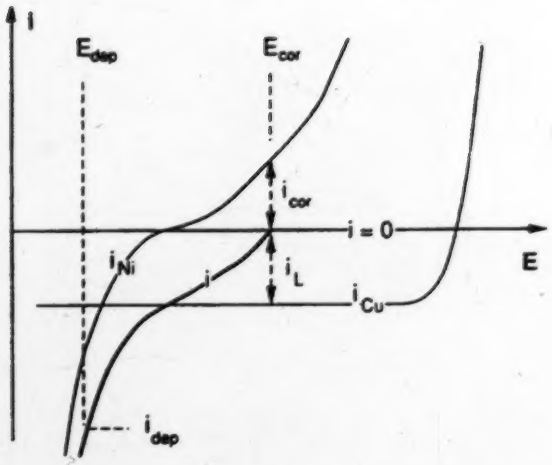

Fig. 2.21 Schematic presentation of partial anodic and cathodic currents for Cu and Ni and of the total cathodic current during deposition of a Ni-Cu alloy from an electrolyte containing a high Ni and a low Cu concentration [Landolt 94].

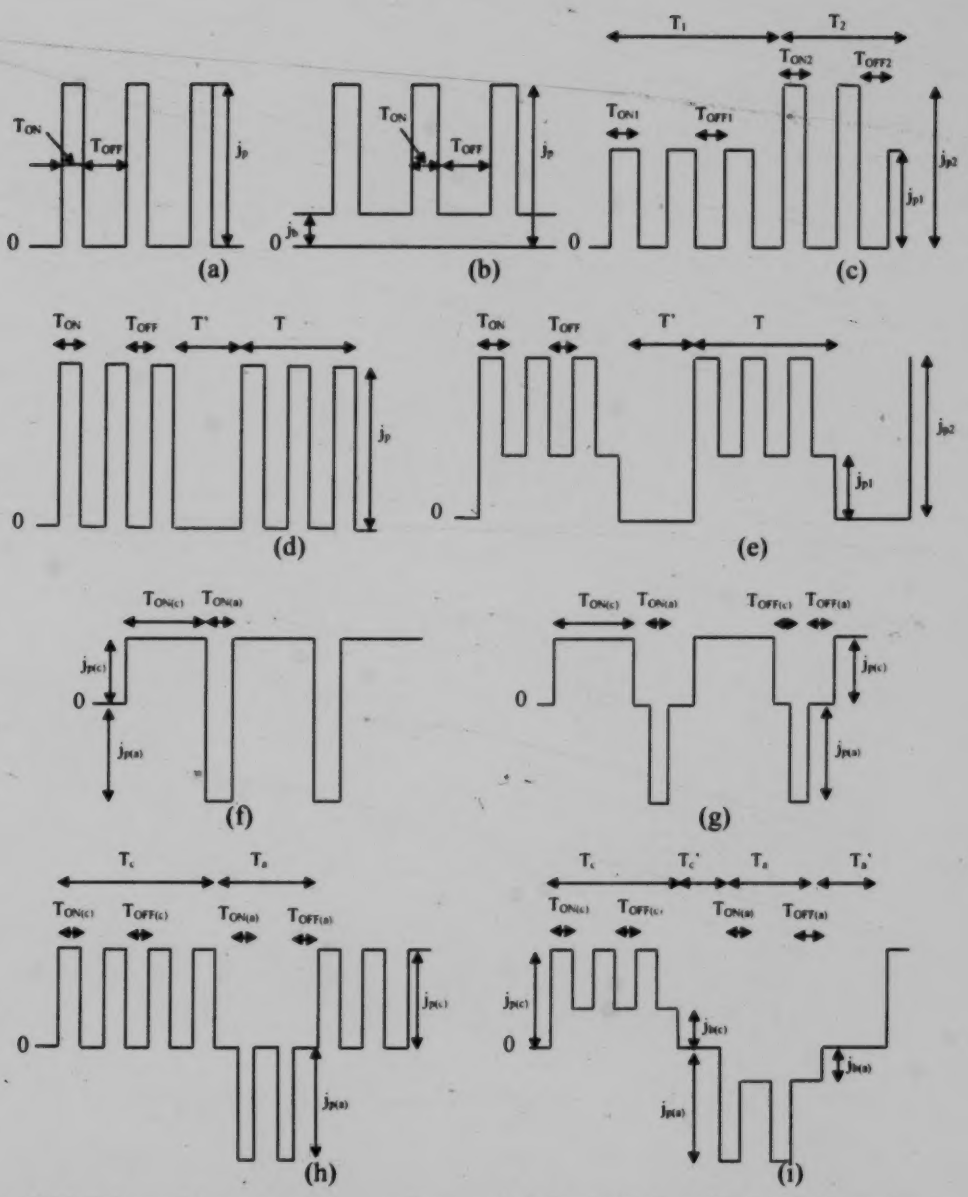

Fig. 2.22 Schematic representation and suggested nomenclature for some square-wave-modulated current systems, and definition of related parameters. (a) Pulse, (b) Superimposed pulse, (c) Duplex pulse, (d) Pulsed pulse, (e) Pulse-on-pulse, (f) Pulse reverse, (g) Pulse reverse (with OFF time), (h) Pulsed pulse reverse, (i) Pulse-on-pulse reverse [Puipe 86].

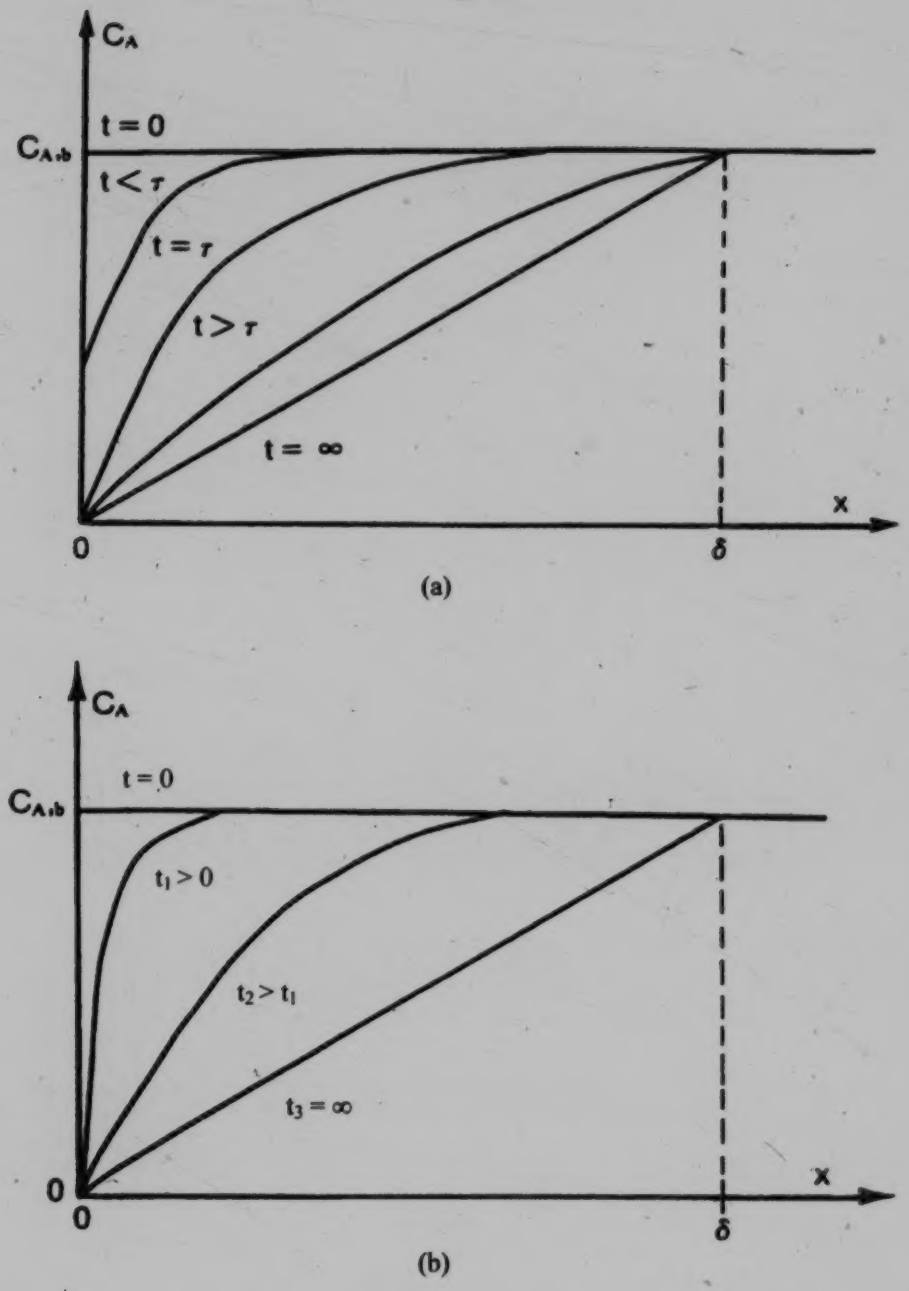

Fig. 2.23 Schematic concentration profiles at the cathode upon application of (a) a constant current step and (b) a constant potential step [Puipe 86].

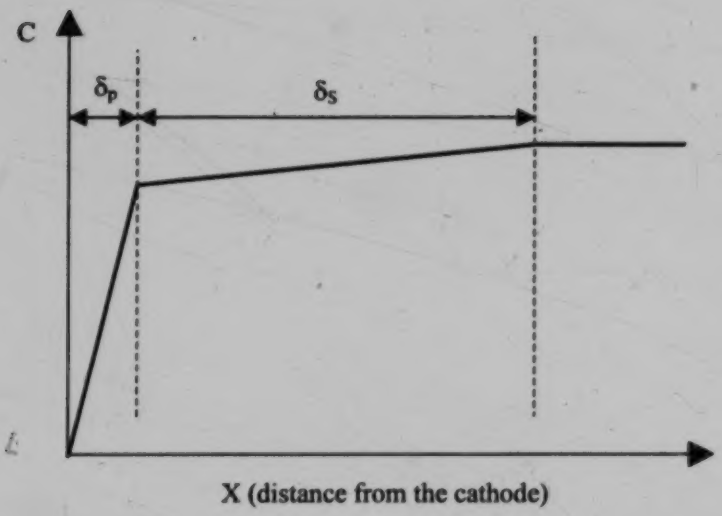

Fig. 2.24 Concentration profiles of the two diffusion layers on pulse electrolysis at the end of a pulse. δ_p is the thickness of the pulsating diffusion layer; δ_S is the thickness of the stationary diffusion layer.

Chapter 3

Bath Stability

3.1 Introduction

Electrodeposition of gold was widely acclaimed in the 1800's because this method of coating base metals would eliminate the mercury poisoning hazards of fire gilding. The industry eventually settled down to alkaline gold cyanide solutions, which were used for well over a century. The rapid growth of the printed circuit industry during the late 1950's provided a strong impetus for the development of acid gold solutions. The two main problems associated with conventional alkaline gold plating of edge contacts are attack of the adhesive bond between the copper foil and laminate by high pH solutions and limited wear resistance of deposits. Rinker and Ehrhardt [Rinker 63] discovered that potassium cyanuarate (I) remained stable in acid media down to a pH as low as 3.0 before decomposition occurred with slow precipitation of aurous cyanide. This formed the basis of acid gold plating solutions. Such solutions, whether acidic or alkaline, of course, were still poisonous.

Another strong impetus for developing non-cyanide gold plating solutions was the rapid growth of the electronics industry, which created demands for specific deposit characteristics which could not be met by cyanide gold solutions. A cyanide system has the problem of alloy deposition because of the extremely strong complexing ability of cyanide with many base metals. This problem was partially solved by eliminating free cyanide and operating at a pH of 3.0 - 5.0, but under these conditions heavy deposits (10μm or more) were not possible.

The challenges in developing a non-cyanide gold plating solution were essentially twofold:

(1) Obtaining stable solutions, since cyanide is the strongest gold complexing agent.

(2) The need for new corresponding base metal complexes, to ensure good compositional control of gold alloy by plating base metals in a controlled manner.

As early as 1845, Elsner [Elsner 45] suggested that non-cyanide gold electrolytes might have advantages. He mentioned a $KAuCl_4$ solution and a gold sulfite solution. Electrodeposition from gold (III) halide complexes has been reviewed by Page [Page 74]. Except for a Japanese patent [Matsumoto 86] for an Au-Sn alloy plating bath, no recent reports of developments for chloride systems have been noted. The thiomalate complex of gold that has been used is sodium gold (I) thiomalate, $NaOOC{\bullet}CH_2{\bullet}CH(SAu){\bullet}COONa$, which is reported to be highly stable. Its application in the plating of gold and Au-Sn alloys has been patented [Duva 70, Sel-REX 71]. Other types of electrolytes appear mostly in the patent literature [Schloetter 32, Schloetter 36], for instance, thiocyanate bath ($Au(SCN)_2^-$), iodide bath, and thiosulphate ($Au(S_2O_3)_2^{3-}$) baths. Little commercial use has been made of them.

The sulfite system is the one that has been studied most thoroughly as reviewed in Section 2.1.8.1 of Chapter 2 and is the only commercialized non-cyanide gold plating system. So far almost all the commercial sulfite gold plating solutions are alkaline and no reports have been noted about gold alloy deposits, which contain as high a content as 30at% of base metals. The problem of bath stability in sulfite systems still exists.

The goal of this project is to obtain a stable non-cyanide plating bath of gold-tin eutectic solder. The solution that was chosen as a starting point is the chloride system which was claimed to be very stable in the literature [Matsumoto 86]. Preliminary experiments were carried out to try to obtain the stable solution as described in the patent. The solutions deteriorated immediately when tin salt was added in the ammonium citrate buffered gold solution. To prepare a clear and stable solution for gold-tin alloy plating, a screening test was conducted to select suitable stabilizers from several candidates. The effect of the selected stablizers on the polarization behavior of the cathode in the solutions was studied to understand the roles of stabilizers and to obtain important reference information regarding current response to cathodic potential change, open circuit potential, limiting current density, and the potential at which limiting current density is approached. A proper set of plating parameters can be derived from the information. A causticity test for the wafers in the developed solution was performed to examine the causticity of the solution to the wafers to be plated.

3.2 Experimental Methods

3.2.1 Solution preparation

Starting solution

The starting solution S0 is listed as follows:

200	g/L	Ammonium citrate ($H_4NO_2CCH_2C(OH)(CO_2NH_4)CH_2CO_2NH_4$)
20	g/L	$KAuCl_4$
13	g/L	$SnCl_2.2H_2O$
30	g/L	L-ascorbic acid ($HOCH_2CH(OH)(C(H)OC(O)C(OH)C(OH)$)
1	g/L	$NiCl_2$
5	g/L	Peptone

The solutions were prepared according to the design in Table 3.1. The water used to dissolve chemicals is deionized water. The precipitated powder was examined by energy dispersive x-ray analysis (EDS) in the SEM.

Preliminary screening test with several non-cyanide stabilizers

Since Solution S0 was not stable, stabilizers had to be found to obtain a relatively stable solution. Several stabilizers were chosen for the purpose of stabilizing gold ions or tin ions in the bath. Three stabilizers as shown in Table 3.2 were added separately in the following solution:

300	g/L	Ammonium citrate
10	g/L	$KAuCl_4$

The solution preparation procedure was to add chemicals in the sequence of ammonium citrate, gold salt, stabilizer, and then tin chloride salt (5g/L). After a chemical was added in the solution, the solution was stirred thoroughly to dissolve the chemical completely. Then another chemical was added.

Bath stability test for various solutions

From the screening test, sodium sulfite was selected as a stabilizer for gold ions in the bath. L-ascorbic acid was chosen to prevent tin hydrolysis. Experiments were designed as shown in Table 3.3 to test the lifetime of the solutions containing different contents of sulfite, ammonium citrate, and different total content of gold and tin salt in the bath. The effect of peptone and ethylene diamine ($H_2NH_2CCH_2NH_2$) on bath stability was also tested.

3.2.2 Polarization behavior of the solutions

Polarization testing of the cathode in Au solutions, Sn solutions and Au-Sn solutions was done on an EG&G Potentiostat/Galvanostat Model 273. Only cathodic data is plotted in the subsequent figures. Open circuit potentials (Table 3.4) were determined from the full anodic-cathodic curves. The working electrode was a piece of InP wafer with a 25nm Ti adhesion layer and a 200nm Au coating on the surface. The wafer was cleaned in ethyl alcohol. Stop-off lacquer was used to define a 10mm×10mm exposed area of the gold-coated surface and to cover the backside of the sample. Platinum foil (20mm×10mm) was used as the anode, and a saturated calomel electrode (SCE) as the reference electrode. The cathode potential scanning rate was set at 0.5 mV/second. The solutions utilized are shown in Table 3.4.

3.2.3 Causticity test of wafers

Causticity tests for InP and GaAs were performed in Solution S6. The wafers with no metallization layers were weighed using a microgram balance. AFM was used to check their surface morphology before and after they were soaked in the above solution for 48 hrs at room temperature. The weight change was measured for each wafer.

3.3 Results and Discussion

3.3.1 Solution preparation

Starting solution

Bivalent tin chloride salt undergoes hydrolysis in water as shown in Equation (3.1).

$$Sn^{2+} + 2H_2O \rightarrow Sn(OH)_2 \downarrow + 2H^+ \qquad (3.1)$$

where the solubility product of $Sn(OH)_2$ is 3×10^{-27}. The solubility product of $Sn(OH)_4$ is 10^{-57} [Chang 81]. Solution A in Table 3.1 contains 30 g/L of L-ascorbic acid. Because of the presence of excess L-ascorbic acid in the solution, hydrolysis is minimized and no basic tin compound precipitation was found after preparation. The same situation was found for Solution B containing 200 g/L of ammonium citrate due to the weak acidity (~6.5) of ammonium citrate. After one week Solution A turned turbid, while Solution B changed to dark yellow from colorless but still remained clear. The difference may imply that ammonium citrate is a complexing agent for Sn^{2+} ions. But no information is available about the complexing ability of ammonium citrate with bivalent tin ions. Although the actual chemistry for the change in the solutions is not well understood, the change is attributed to the oxidation of stannous ion (II) by dissolved air to stannic ion (IV) and the formation of stannic compounds. Higher temperature than room temperature results in increased rate of this oxidation reaction in the solution. From Table 3.1 it is concluded that without any anti-oxidant additives, Solution A and B can remain stable for a week. The behavior of bivalent tin ions in water is very complex. The possible form of tin ions in a chloride solution can be $[SnCl]^+$, $[SnCl_2]$, $[SnCl_3]^-$ and $[SnOH]^+$ with stability constant of 14, 50, 50 and 10^{10}, respectively [Chang 81].

$KAuCl_4$ is soluble in aqueous solution and is light sensitive. It is used for toning silver photographic prints. Preparation of Solution C and D shows that $KAuCl_4$ undergoes hydrolysis both in light and in darkness. The solutions precipitate fine black powder, which gradually changed into gold color afterwards. The powder was determined by EDS

to be metallic gold powder. In aqueous solution, $AuCl_4^-$ ions are hydrolyzed to some extent according to Equation (3.2), forming species such as $[AuCl_3]H_2O$. This in turn acts as a weak acid forming species such as $AuCl_{4-n}(OH)_n$ (where n = 0 to 4 and increases with increasing alkalinity) in alkaline solutions.

$$AuCl_4^- + H_2O \rightarrow (AuCl_3)H_2O + Cl^- \rightarrow AuCl_3(OH) + H^+ + Cl^- \quad (3.2)$$

The pH value of Solution E containing 200 g/L of ammonium citrate falls in the range of a weak acid. The hydrolysis of $KAuCl_4$ is prevented by the presence of concentrated ammonium citrate. Since $(NH_4)^+$ hydrolyzes in water as shown in Equation (3.3) and produces a significant content of NH_3 that dissolves in the solution, NH_3 can form complex $Au(NH_3)^{3+}$ cations with simple gold (III) ions (if any are present) in the solution:

$$(NH_4)^+ \rightarrow NH_3 + H^+ \quad (3.3)$$

The stability of gold (III) ions in the solution is further improved. The stability constant β_4 for $AuCl_4^-$ is 10^{26}. However no information about the stability constant of $Au(NH_3)^{3+}$ has been found in the literature.

Preparation of Solution F was the first attempt to make a gold-tin solution. It turned black and turbid immediately after the gold solution (Solution E) was added into the tin solution (Solution B). The exact chemistry responsible for the problem of instantaneous precipitation of fine black powder is not clear because of the lack of relevant information. Still, it is reasonable to surmise that it is a chemical interaction between gold ions and bivalent tin ions that causes the problem. The fine black powder was determined by EDS to be metallic gold powder. The chemical processes for gold precipitation when tin salt is added can be $AuCl_4^-$ ion reduction to $AuCl_2^-$ ions, followed by $AuCl_2^-$ ion dissociation according to the following reaction:

$$3AuCl_2^- \rightarrow AuCl_4^- + 2Au + 2Cl^- \quad (3.4)$$

Since ammonium citrate is able to complex gold ions, solutions with more concentrated ammonium citrate are supposed to be more stable. Preparation of Solution G and H is the result of such an attempt. No improvement was found for Solution G, while Solution H was the first solution obtained that was clear after preparation. Solution H was obtained by adding the gold solution drop by drop into the tin solution instead of just pouring the gold solution at once into the tin solution. This means more concentrated ammonium citrate is needed to solve the problem of chemical reaction between gold (III) ions and tin (II) ions. The way in which ammonium citrate works might be twofold, i.e., acting as either a gold complexing or a tin complexing agent. From the fact that an extremely high concentration of ammonium citrate is needed for the purpose of stabilizing gold ions or tin ions, it can be surmised that ammonium citrate is not a strong complexing agent for gold (III) ions, nor for tin (II) ions. Solution H has two fatal problems in terms of being used as a practical plating solution. One is its short lifetime. It deteriorated and precipitated only a few hours after preparation. The other problem is the high viscosity of the solution resulting from the high concentration of ammonium citrate in the solution. This is unfavorable for practical plating since high viscosity results in a slow mass transport rate and therefore lower limiting current density. Although the improvement is minor, the key to developing a stable gold-tin solution lies in finding a more efficient gold complexing agent to decrease the oxidizing ability of gold ions when they have to be mixed with the reducing agent, bivalent tin. Another possible way to approach the same goal is to find a tin complexing agent to decrease the reducing ability of bivalent tin.

Preliminary screening test with several non-cyanide stabilizers

In Table 3.2 several stabilizers were chosen and tried based on the above discussion. Na_2SO_3 and $Na_2S_2O_3$ are gold complexing agents while $Na_2H_2EDTA{\bullet}2H_2O$ is a tin complexing agent. The results in Table 3.2 show that Na_2SO_3 was most effective in reducing gold precipitation during the addition of tin salt. Na_2H_2EDTA is a complexing agent for many base metal impurities in plating baths. It is often used to reduce the contamination of the coating with base metals where very pure gold deposits are required.

The stability constant for $[SnEDTA]^{2-}$ ions is 10^{22} [Chang 81], which is fairly high. But it fails to prevent the reaction between gold ions and tin ions. The problem may be due to tin salt that should be dissolved in Na_2H_2EDTA solution and be present in the form of an EDTA complex before being mixed with the gold solution.

From Table 2.3, the stability constants for $[Au(SO_3)_2]^{3-}$ and $Au(S_2O_3)_2^{3-}$ are 10^{10} and 5×10^{28}, respectively. Although the latter has a much higher stability constant, it still has no positive influence on solution stability in this specific situation. This phenomenon may be due to its incompatibility with the other chemicals in the solution, e.g., the buffering agent, ammonium citrate, which tends to nullify the stabilizing effect of the stabilizer.

The complexes formed by gold (I) and gold (III) in sulfite media are expected to be of the types $Au(SO_3)_2^{3-}$ and $Au(SO_3)_4^{5-}$, respectively. Pure $Na_5[Au(SO_3)_4].5H_2O$ has been isolated [Oddo 27], while there is no unequivocal evidence for the preparation of an $Au(SO_3)_2^{3-}$ complex in the solid state. However the existence of the $Au(SO_3)_2^{3-}$ complex in sulfite baths has been reported by Socha, *et al*, [Socha 75]. In one method of preparing such baths [Smith 62], for example, the precipitate, which is formed by adding ammonia to a gold chloride solution, is simply dissolved in an alkaline metal sulfite solution. The gold (III) is reduced to gold (I) in the process. In the 1970's, gold (I) amine-sulfite complexes stable at pH levels as low as 4.5 were found. In the preparation [Zuntini 74] of such baths the gold may be added in the form of solid gold (III) amine-sulfite complexes, which are reduced *in situ* by warming the bath before use. The complex

$$Na[(H_2N\text{-}H_2C\text{-}CH_2\text{-}NH_2)Au^{III}(SO_3)_2]$$

can be precipitated by mixing solutions of gold (III) chloride and excess ethylene diamine, cooling, and then adding a saturated solution of sodium sulfite. The gold (I) amine-sulfite complexes, to which they presumably give rise on reduction, do not appear to have been isolated. Laude, *et al*, patented solutions based on ammonium gold (I) sulfite that could operate at pH 6-8 in the absence of polyamines [Laude 80]. The solutions were prepared by adding ammonia to an $HAuCl_4$ solution, which resulted in the

formation of a precipitate. This was followed by dissolving this precipitate in an aqueous ammonium sulfite solution. This precipitate, the nature of which is ill determined, is called 'fulminating gold'. Before dissolving in the ammonium sulfite solution, the precipitate is washed by decantation until all chloride ions are eliminated.

The method of preparing gold-tin sulfite solutions in this work is a little different compared with the methods of preparing gold sulfite solutions described above. The gold is added in the form of solid $KAuCl_4$ salt that is dissolved in a concentrated ammonium citrate solution. When Na_2SO_3 is added to the solution, no precipitation occurs. It is presumed that the gold (III) ions have been reduced to gold (I) ions. The stability of the gold-tin solution was substantially improved. No gold precipitation occurred when tin salt was added.

Based on this fact, Na_2SO_3 was selected as the stabilizer for gold ions in the following work.

Bath stability test for various solutions

The experimental results for the effect of bath chemical content are listed in Table 3.3. Solutions S1 and S2 contained no sulfite. They deteriorated immediately when tin salt was added. With 60 g/L of Na_2SO_3, Solution S3 remained clear and stable for 4 days. After 4 days it started to precipitate fine gold particles gradually. Compared with Solution S3, Solution S4 containing 15 g/L of L-ascorbic acid had a significantly improved stability of 15 days. Its stabilizing effect on the solution is quite surprising since it was originally added to prevent Sn hydrolysis. L-ascorbic acid is a weak acid. The addition of 15 g/L of it only changed the pH value of the solution from ~6.5 to ~6, because a concentrated buffering agent, ammonium citrate, was present in the solution.

Comparing Solutions S5 and S6, it seems that the concentration of ammonium citrate in the solution has very little influence on the bath stability, which may be because almost all the gold ions are present in the form of gold sulfite complex. A lower content of citrate is favored for practical plating.

Comparison of Solutions S4, S6 and S10, which contained gradually increased total content of gold salt and tin salt, shows that the higher the total content, the shorter the

bath lifetime. Because the chemical reaction rate is proportional to the concentrations of the reactants, the higher the total concentration of the reactants, gold ions and tin ions, the faster the gold precipitates from the solution due to faster chemical reaction between gold and tin salts.

The effect of sulfite on bath stability can be seen clearly by comparing Solutions S6 and S7. Solution S7 contained less sulfite and its lifetime was shortened from 9 days to 3 days. Since the stability constant for gold sulfite is quite low, the need for free sulfite is very pronounced.

Solution S7, S8 and S9 had the same formula except that S8 contained 0.08M of ethylene diamine and S9 contained 3 g/L of peptone. The addition of ethylene diamine before adding sulfite to the solution, significantly improved the bath stability from 3 days to more than 30 days. Addition of peptone has less of an effect, but still extended the lifetime from 3 days to 5 days and much less gold precipitated compared with S7. The drawback of employing more additives in a bath is increased problems in quality control.

Another possible alternative way to improve bath stability is to prepare and store the gold solution and tin solution separately and mix them when plating is to be performed. Solution S11 is a gold solution and S12 is a tin solution. If S11 and S12 are mixed at a 1:1 volume ratio, the overall makeup would be the same as S7. The lifetime for the gold solution is 7 - 8 days. After 7 – 8 days, gold precipitation started in the gold solution and the tin solution turned light yellow from colorless. The reason that gold still precipitates from the solutions containing sulfite is that the stability constant of sulfite complex is not large enough and, with time, sulfite is subject to oxidation by air at the liquid/air phase interface. It can be predicted that if the solutions are used for plating, the lifetime of the solution will become even shorter because of the consumption of sulfite by anodic and chemical oxidation and cathodic reduction. The change in the color of tin solution is due to the oxidation of bivalent tin to tetravalent tin. The solution remained clear for more than a month. Compared with Solution S7, the lifetime of 7 – 8 days for the separate solutions is significantly better than 3 days for S7.

3.3.2 Polarization behavior

The polarization curves obtained for gold solutions, tin solutions and gold-tin solutions are plotted in Fig. 3.1, Fig. 3.2, Fig. 3.3 and Fig. 3.4, respectively.

Comparing curves Fig. 3.1(a) and Fig. 3.1(b), it is observed that the concentration of ammonium citrate does not affect the polarization behavior of the cathode in the gold solution very much. The limiting current density (~ 1mA/cm^2) and the open circuit potential do not change significantly. When the cathode potential is lower than ~ -0.7 V vs. SCE, organic decomposition at the cathode takes place, plating carbon at the surface of the cathode. For Solutions SAu1 and SAu2, because their polarization curves only have one wave in the Au plating region, it is likely that the cathode reaction is a one-step reaction.

$$Au(III) + 3e \rightarrow Au(0) \qquad (3.5)$$

The following mechanism for the reduction of gold (III) in chloride solution was proposed by Nicol, *et al*, [Nicol 76-1]:

1. $AuCl_4^- \leftrightarrow AuCl_3 + Cl^-$
2. $AuCl_3 + 2e \rightarrow Au(I)$ (slow step)
3. $Au(I) + e \rightarrow Au(0)$ (fast step)

The slow step reaction (reaction 2) is not balanced. Because the role of the chloride in the reaction is not clear, chloride not indicated on the right side of the reaction.

Fig. 3.1(c), (d) and (e) show that addition of sodium sulfite in gold solution dramatically lowers the open circuit potential. Both the oxidizing ability of gold ions and the ease of plating gold have been greatly decreased. The effect of different concentrations of sulfite in the solution on the polarization curves is not very significant

and cannot be correlated in a clear way. These curves (c), (d), and (e) have one wave at the potential range higher than -0.75 V vs. SCE, where the cathodic reaction could be

$$Au(I) + e \rightarrow Au(0) \qquad (3.6)$$

The potential for carbon plating is also lowered to ~0.75 V vs. SCE. The proper range of the cathode potential for gold plating in these three solutions ((c), (d) and (e) is -0.60 to -0.75 V vs. SCE with a limiting current density of less than 2 mA/cm^2. At potentials higher than -0.6 V vs. SCE, the gold plating speed is too low, while at potentials lower than -0.75 V vs. SCE, gold plating is diffusion controlled which is usually not good for practical plating. At this potential, hydrogen evolution also starts, resulting in a lower current efficiency and a local increase in pH which can cause tin hydrolysis and incorporation of tin hydroxide into deposits.

Fig. 3.1(f) and (g) show the effect of gold content in the solution. The higher gold content in the bath results in a little higher limiting current density, which is favorable for plating speed. However, the stability for solutions containing higher gold content is worse. Where a longer lifetime of solution is preferred, a lower gold content is a better choice.

Figs. 3.2(a) to (c) show the effect of ammonium citrate on the polarization behavior of the cathode in tin solutions. Curve (a) was obtained from SSn-1, which contains only tin salt and L-ascorbic acid. Its open circuit potential is much higher than that of curve (b) and (c) obtained for SSn-2 and SSn-3 that contain ammonium citrate. This might imply that tin ions form complexes with ammonium citrate although no information about this is available. The cathodic reaction for these three solutions is expected to be

$$Sn(II) + 2e \rightarrow Sn(0) \qquad (3\text{-}7)$$

where Sn(II) ions are in the form of simple tin ions for curve (a), and in the form of a tin complex for curves (b) and (c).

Hydrogen evolution in SSn-1 occurs at a potential around -0.65 V vs. SCE, while in SSn-2 and SSn-3, the potential is moved to much more negative values of about -1.10 V vs. SCE. This is because ammonium citrate keeps the pH of the solution around 6.5, which greatly suppresses hydrogen evolution. The change in the concentration of citrate in the bath does not seem to significantly change the limiting current density and open circuit potential.

Figs. 3.3 (a) to (d) show the effect of sodium sulfite on Sn plating. Curve (a) is for Solution SSn-3, which contains no sulfite, while curve (b), (c) and (d) are for SSn-4, SSn-5 and SSn-6 which contain 30g/L, 60g/L and 100g/L of sulfite, respectively. All the curves for solutions containing sulfite have two distinct waves in the tin plating region, which correspond to a potential range of higher than -1.2 V vs. SCE. The first wave occurs in a potential range of higher than -0.8 V vs. SCE, while the second wave occurs at a potential between -0.8 - -1.2 V vs. SCE. The second wave has a much higher limiting current density (>3mA/cm^2) than the first wave (<1mA/cm^2). This means that there are two different cathodic reactions occurring over different potential ranges as a result of the addition of sulfite. It is clear from the figures that the addition of sulfite results in a higher limiting current density and higher cathodic potential, which makes Sn plating easier. The open circuit potential is the highest and the limiting current density is the largest for sulfite additions of 30g/L. If too much sulfite is added, e.g. 100g/L, the effect on open circuit potential and limiting current density is not as great as that for solutions containing less sulfite. The observations about the effect of sulfite addition must be related to the interaction between ammonium citrate and sulfite for two reasons. First of all, when sulfite is added, some NH_3 gas is released from the solution during preparation. The addition of sulfite changes the concentration of (NH_3) in the solution somehow. Secondly, Sn is plated from a tin complex, which is believed to be a tin-(NH_3) complex. Although the exact mechanism of how the addition of sulfite affects Sn plating is not known, it is clear that the addition of sulfite to the solution lowers the concentration of the tin complexing agent, (NH_3), facilitating tin plating.

Polarization curves for Solutions SSn-5, SSn-7 and SSn-8 which contain different tin contents are shown in Fig. 3.3(c), (e) and (f). With more tin salt in solution, a larger limiting current density results while no difference in open circuit potential is found.

From Fig. 3.3, it can be seen that for Sn plating the suitable potential range is approximately from -0.7 to -1.10 V vs. SCE. Comparing this region with the suitable range for gold plating (Fig. 3.1d), -0.60 to -0.75 V, the overlapping region is very narrow, which is disadvantageous for practical plating.

The polarization curve for a gold-tin solution is given in Fig. 3.4(a). The curves for Solution SAu-4 and SSn-8 are shown in Fig. 3.4(b) and (c) while Fig. 3.4(d) is the sum of curves (b) and (c) obtained by summing up the current densities in the curve (b) and (c) at the same potential. Figures 3.4 (a) and (d) are fairly similar. This implies that the gold plating and tin plating are not completely independent plating processes. There are three distinct regions in curve (a), which are indicated by AB, CD and DE. The first region, AB, corresponds to the plating of nearly pure gold at a potential of higher than ~ -0.68 V, since there is no significant current density for tin plating in this region of curve (c). The steep edge BC from ~ 1mA/cm^2 to 3mA/cm^2 is due to the incorporation of tin plating. It can be predicted that the tin content in deposits will increase with increasing current density in the range of ~ 1 to 3mA/cm^2. The second region, CD, corresponds to the potential from -0.68 V to -0.8 V vs. SCE and current density from ~ 3 to 4.2 mA/cm^2. The total current density increases as the potential is lowered in curve (a). In this region, curve (c) shows that the current density for tin plating goes up first, then remains constant and jumps to a higher level again, while gold plating current density keeps rising as shown in curve (b). Although it is difficult to predict precisely how the deposit composition will change with the current density in this region, it can be estimated that the deposit composition will remain roughly constant because both gold and tin plating increase as the potential is lowered. In the region of DE, the current density increases rapidly with decreasing potential because of the incorporation of hydrogen evolution or carbon plating. It is also difficult to predict the tendency of deposit composition change with increasing current density. However, poor deposit appearances and high carbon content in deposits can be expected. From Fig. 3.4(a), a suitable range of working current

density or potential would be the region CD for gold-tin plating from a practical point of view, because in this region, the deposition composition is expected to not change significantly with the current density or the cathodic potential.

3.3.3 Causticity test of wafers

The results of weight loss for different wafers are listed in Table 3.5. The measurement accuracy of the balance is ±0.0002g.

Within the measurement accuracy, there is no weight loss for the wafers after soaking in Solution S6 for 48 hrs. The AFM images for InP and GaAs wafers before and after the causticity test are shown in Fig. 3.5 and Fig. 3.6. No corrosion pitting was detected for both InP and GaAs wafers. The substance present on the surface of InP wafer after the test may be chemical residues from the highly viscous solution due to the incomplete cleaning of the sample after the test.

Among the two types of wafers, only InP is subject to the attack by a strong hydrochloric acid. Solution S6 is only very weak in acidity. The chloride ions come from the addition of a relatively low concentration of gold salt and tin salt. Furthermore these chloride ions are acting as complexing ligands for gold and tin ions, where their chemical activity is much lower than that of simple chloride ions.

During a practical plating process, the working potential of the wafer will be around -0.2 to -1.1 V vs. SCE, which is under the condition of cathodic protection for the wafers. The plating time of eutectic Au-Sn solder for the application of laser chip bonding is generally 2 – 3 hrs. Therefore the conditions utilized in this causticity test are harsher than the practical plating conditions. From the data in Table 3.5, it can be concluded that the solution S6 has no causticity effect on InP and GaAs wafers.

3.4 Conclusions

A relative stable gold-tin plating system has been developed. This is a non-cyanide weak-acid system with ammonium citrate as a buffering agent for hydrogen ions and tin ions, chloride-ammonium citrate-sodium sulfite as a mixed complexing agent for gold, and L-ascorbic acid as an inhibitor of tin hydrolysis.

The bath stability depends on the total content of gold salt and tin salt, additives such as peptone, ethylene diamine, sodium sulfite concentration, and the way the solution is prepared and stored.

The effects of ammonium citrate, sulfite, concentration of gold and tin salt on the polarization behavior of a cathode in various solutions have been studied. In Sn solutions, addition of ammonium citrate changes the open circuit potential of the cathode and the hydrogen evolution potential to more negative values. The concentration of ammonium citrate has no significant effect on the polarization curves for Au solutions and tin solutions. Addition of sodium sulfite in gold solutions lowers the open circuit potential substantially and the content of sulfite seems to have very little effect on the curves for gold solutions. For tin solutions, the open circuit potential is moved to higher values and the limiting current density is increased somewhat, thereby enhancing tin plating. The shape of the curves for solutions with sulfite undergoes a substantial change from one-wave curves to two-wave curves, which is believed to result from the interaction between sulfite and ammonium citrate. The addition of a specific concentration of sulfite has the greatest effect on the curve. Comparing the curve for a gold-tin solution and the summed two component curves for the corresponding gold solution and tin solution, it was found that they are very similar. This shows indirectly that the gold and tin plating processes are independent processes in gold-tin alloy plating. From the curves in Fig. 3.4, it can be determined that the working current density range that can be used for plating an Au-Sn alloy from Solution SAuSn is the region CD.

The causticity test showed no weight loss and no corrosion pits were detected for InP and GaAs wafers after soaking in Solution S6 for 48 hrs. Therefore, the solution is safe for these wafers.

Table 3.1 Solution preparation.

Solution #	Solution	Observations
A	Dissolve 13 g/L $SnCl_2.2H_2O$ in a 30 g/L L-ascorbic acid solution.	Clear solution with pH = 1.7. After one week precipitation occurred.
B	Dissolve 13 g/L $SnCl_2.2H_2O$ in a 200 g/L ammonium citrate solution.	Clear solution with pH ≈ 6.5. After one week, solution turned dark yellow but still clear.
C	Dissolve 10 g/L $KAuCl_4$ in water.	Solution turned black and turbid on standing. Fine black powder precipitated.
D	Dissolve 10 g/L $KAuCl_4$ in water in darkness.	Solution turned black and turbid on standing. Fine black powder precipitated.
E	Dissolve 10 g/L $KAuCl_4$ in a 200 g/L ammonium citrate solution.	Clear solution and stable in light.
F	Add Solution E into Solution B.	Solution turned black and turbid on standing. Fine black powder precipitated.
G	Dissolve 10 g/L $KAuCl_4$ in a 800 g/L ammonium citrate solution and then add Solution B.	Same phenomena as Solution F.
H	(1) Dissolve 10 g/L $KAuCl_4$ in an 800 g/L ammonium citrate solution. (2) Dissolve 13 g/L $SnCl_2.2H_2O$ in a 400 g/L ammonium citrate solution. (3) Add solution (2) to solution (1) drop by drop with violent agitation.	Clear solution with dark-green color. Precipitation occurred a few hours after preparation.

Table 3.2 Screening test of stabilizer candidates.

Stabilizer	Stabilizer concentration (g/L)	Observations
No stabilizer		Fine black powder precipitated immediately after tin salt was added.
Na_2SO_3	20 - 100	Solution was clear and stable for a few days.
$Na_2S_2O_3$	20 - 100	Fine black powder precipitated within a few minutes.
$Na_2H_2EDTA \bullet 2H_2O$*	5 - 40	Gold precipitated on the wall of the beaker within a few minutes after tin salt was added.

* The formula of $Na_2H_2EDTA \bullet 2H_2O$ is $NaO_2CCH_2N(CH_2CO_2H)CH_2CH_2N(CH_2CO_2Na)CH_2CO_2H \bullet 2H_2O$.

Table 3.3 Solutions utilized for bath stability tests.

#	S1	S2	S3	S4	S5	S6	S7	S8	S9	S10	S11	S12
Ammonium citrate (g/L)	200	200	200	200	100	200	200	200	200	200	200	200
$KAuCl_4$ (g/L)	5	5	5	5	7	7	7	7	7	10	14	
Ethylene diamine (M)								0.08				
Na_2SO_3 (g/L)			60	60	60	60	30	30	30	60	60	
L-ascorbic acid (g/L)		15		15	15	15	15	15	15	15		30
$SnCl_2.2H_2O$	5	5	5	5	7	7	7	7	7	10		14
Peptone (g/L)									3			
Solution stability (days)	0	0	4	15	11	9	3	>30 (very small amount of gold fines)	5	7	8 (precipitation starts)	7 (colorless → light yellow, clear for >30 days)

Table 3.4 Solutions utilized to test polarization curves (to be continued).

	Solution Make-up		Open Circuit Potential (V vs. SCE)
Au Solutions	SAu-1	100 g/L Ammonium citrate 5 g/L $KAuCl_4$	0.39
	SAu-2	200 g/L Ammonium citrate 5 g/L $KAuCl_4$	0.31
	SAu-3	200 g/L Ammonium citrate 5 g/L $KAuCl_4$ 30 g/L Na_2SO_3 15 g/L L-ascorbic acid	-0.16
	SAu-4	200 g/L Ammonium citrate 5 g/L $KAuCl_4$ 60 g/L Na_2SO_3 15 g/L L-ascorbic acid	-0.22
	SAu-5	200 g/L Ammonium citrate 5 g/L $KAuCl_4$ 100 g/L Na_2SO_3 15 g/L L-ascorbic acid	-0.22
	SAu-6	200 g/L Ammonium citrate 7 g/L $KAuCl_4$ 60 g/L Na_2SO_3 15 g/L L-ascorbic acid	-0.22
	SAu-7	200 g/L Ammonium citrate 10 g/L $KAuCl_4$ 60 g/L Na_2SO_3 15 g/L L-ascorbic acid	-0.19

Table 3.4 Solutions utilized to test polarization curves (continued).

Sn Solutions	SSn-1	15 g/L L-ascorbic acid 5 g/L $SnCl_2.2H_2O$	
	SSn-2	100 g/L Ammonium citrate 15 g/L L-ascorbic acid 5 g/L $SnCl_2.2H_2O$	
	SSn-3	200 g/L Ammonium citrate 15 g/L L-ascorbic acid 5 g/L $SnCl_2.2H_2O$	
	SSn-4	200 g/L Ammonium citrate 30 g/L Na_2SO_3 15 g/L L-ascorbic acid 5 g/L $SnCl_2.2H_2O$	
	SSn-5	200 g/L Ammonium citrate 60 g/L Na_2SO_3 15 g/L L-ascorbic acid 5 g/L $SnCl_2.2H_2O$	
	SSn-6	200 g/L Ammonium citrate 100 g/L Na_2SO_3 15 g/L L-ascorbic acid 5 g/L $SnCl_2.2H_2O$	
	SSn-7	200 g/L Ammonium citrate 60 g/L Na_2SO_3 15 g/L L-ascorbic acid 7 g/L $SnCl_2.2H_2O$	
	SSn-8	200 g/L Ammonium citrate 60 g/L Na_2SO_3 15 g/L L-ascorbic acid 10 g/L $SnCl_2.2H_2O$	
Au-Sn Solutions	SAuSn	200 g/L Ammonium citrate 5 g/L $KAuCl_4$ 60 g/L Na_2SO_3 15 g/L L-ascorbic acid 5 g/L $SnCl_2.2H_2O$	

Table 3.5 Causticity test of InP and GaAs wafers in solution.

Sample	Weight before soaking (g)	Weight change (g)	Surface morphology
InP	0.1395	-0.0000	No change
GaAs	0.2066	-0.0001	No change

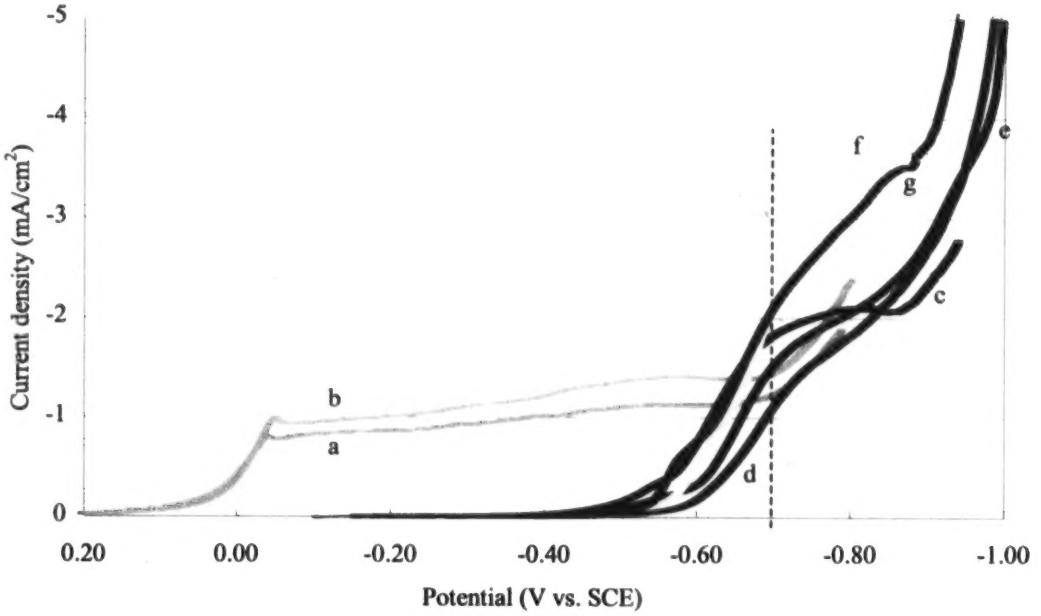

Fig. 3.1 Cathodic polarization curves for Solutions (a) SAu-1, (b) SAu-2, (c) SAu-3, (d) SAu-4, (e) SAu-5, (f) SAu-6, and (g) SAu-7. The dashed line indicates the approximate potential of hydrogen evolution.

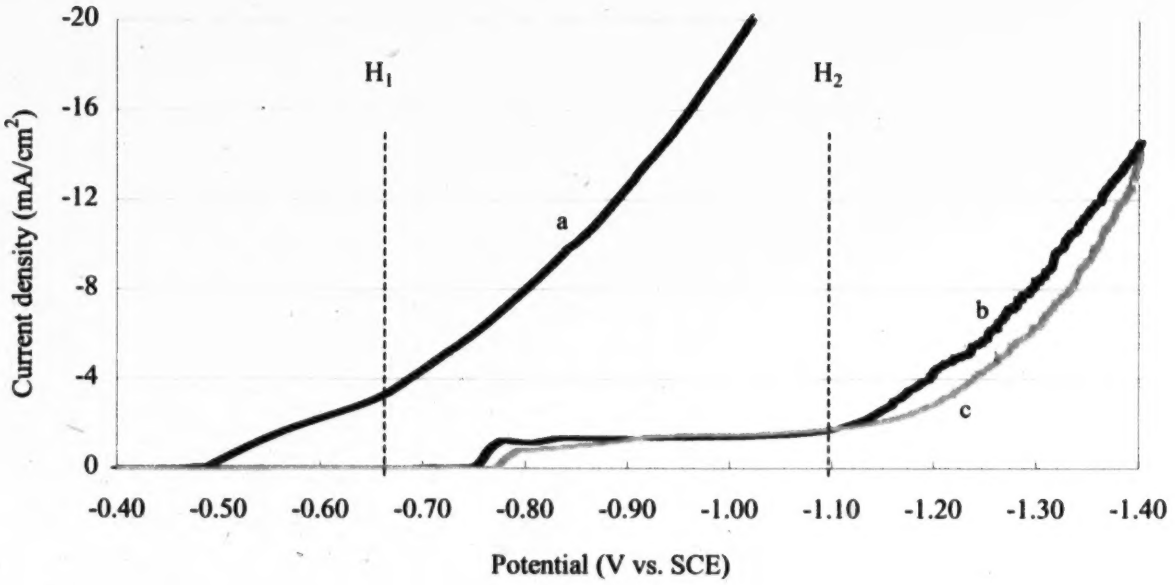

Fig. 3.2 Cathodic polarization curves for (a) SSn-1, (b) SSn-2 and (c) SSn-3. The dashed lines H_1 and H_2 show the approximate potentials for hydrogen evolution on curve (a), and on curves (b) and (c), respectively.

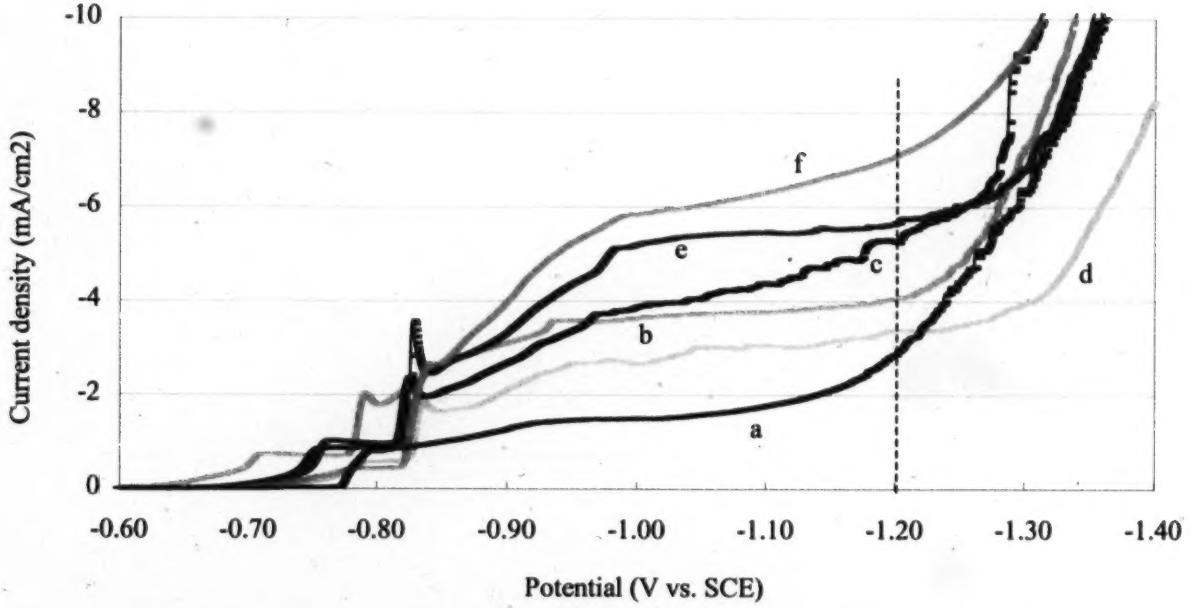

Fig. 3.3 Cathodic polarization curves for Solutions (a) SSn-3, (b) SSn-4, (c) SSn-5, (d) SSn-6, (e) SSn-7, and (f) SSn-8. The dashed line indicates the approximate potential for hydrogen evolution for all the solutions.

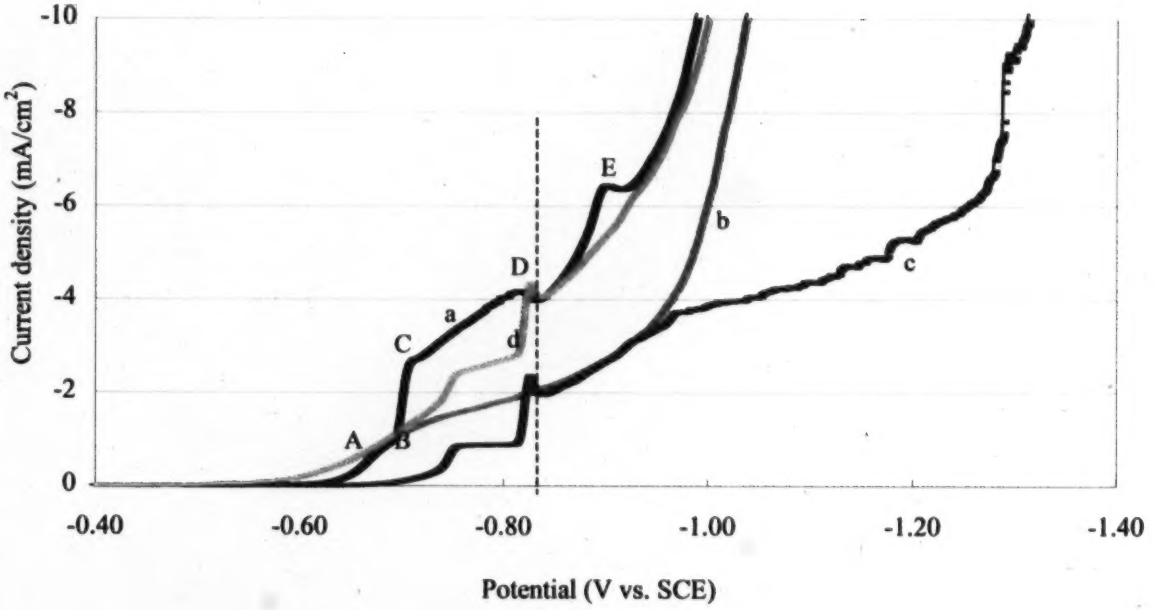

Fig. 3.4 Polarization curves for Solutions (a) SAuSn, (b) SAu-4, and (c) SSn-5. Curve (d) is the sum of curves (b) and (c). The dashed line indicates the approximate potential for hydrogen evolution for curve (a).

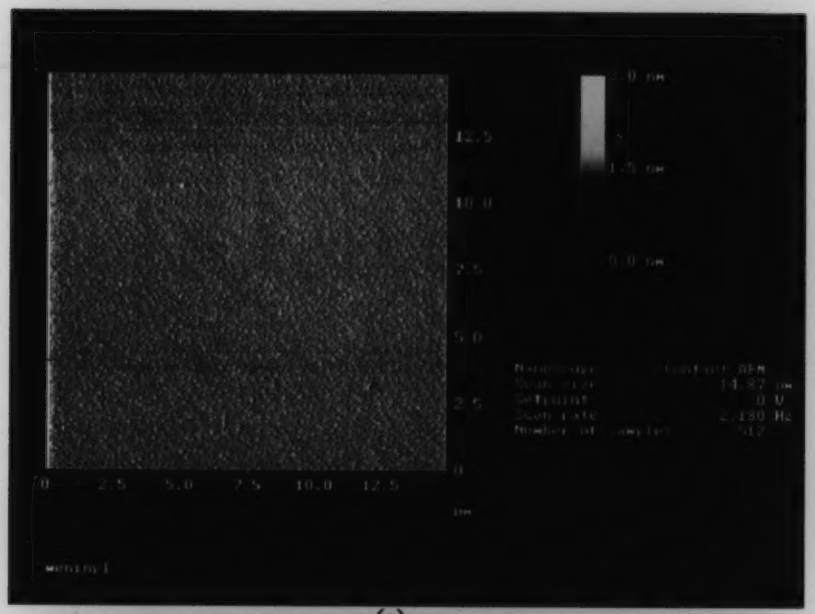

(a)

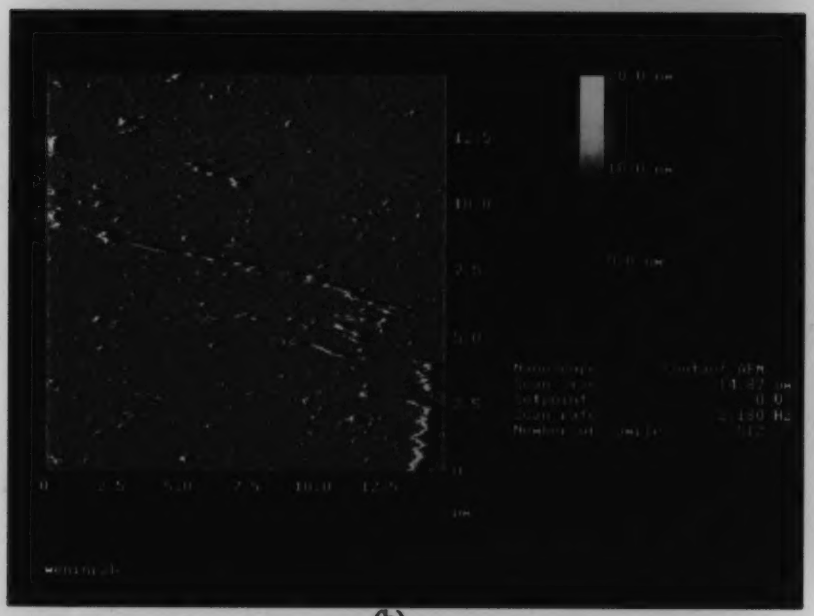

(b)

Fig. 3.5 AFM images of InP wafer surface before (a) and after (b) the causticity test in Solution S6.

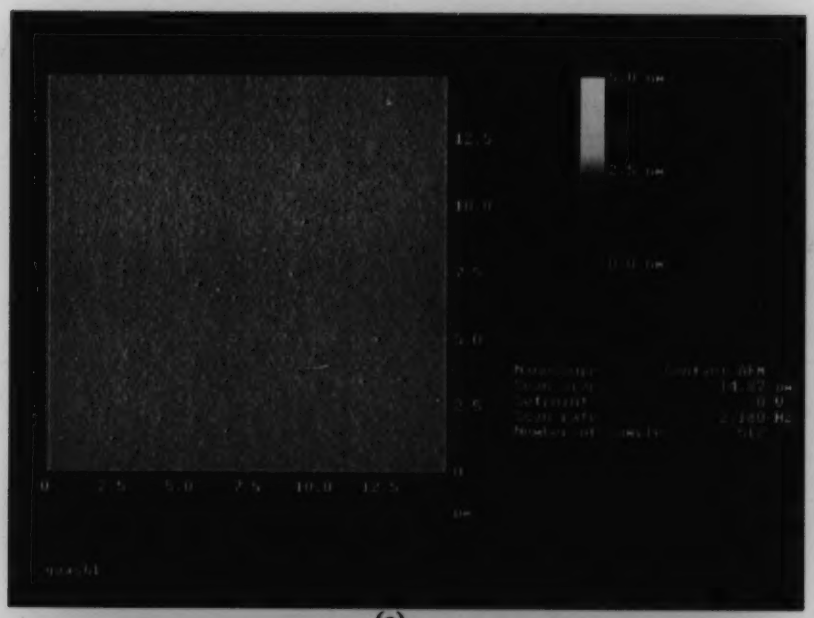

(a)

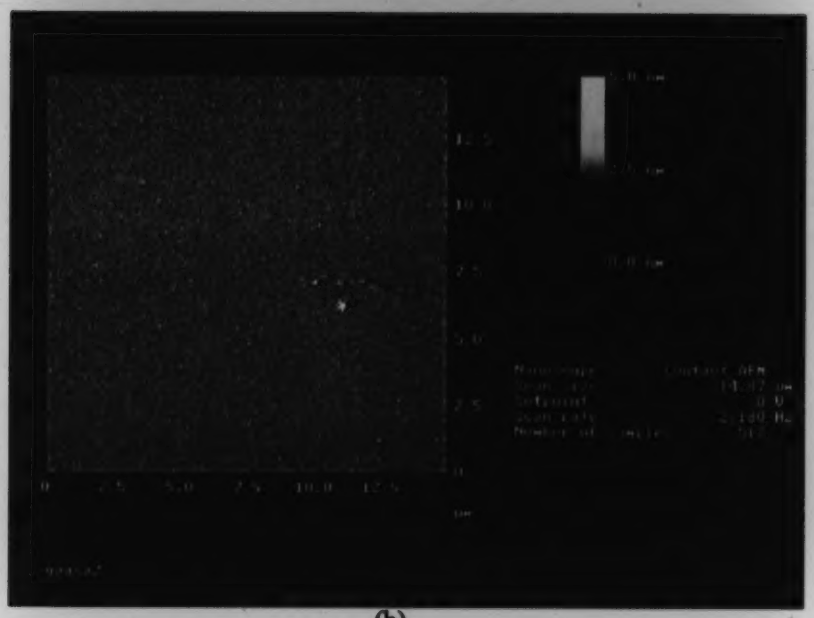

(b)

Fig. 3.6 AFM images of GaAs wafer surface before (a) and after (b) the causticity test in Solution S6.

Chapter 4

Electroplating

4.1 Introduction

As reviewed in Chapter 2, electroplating of gold-tin solder is a one-step batch operation that offers efficient materials usage and limited capital investment compared with metallurgical gold-tin preforms and evaporated deposits. However, the non-cyanide plating process presents some challenges, because the bath stability of such a plating bath is usually shorter than a cyanide bath and the compositional control of the alloy is critical due to the steep liquidius curve in the Au-Sn phase diagram. The issue of bath stability has been addressed in Chapter 3 and generally a two-week lifetime has been obtained. In order to obtain good deposit compositional control, it is essential to study the effect of various electrolyte and plating parameters. Electrolyte parameters include the content ratio of the component in the alloy to be plated in the bath, their total content, and additive content. Plating parameters include plating mode, e.g., DC plating or PC plating, current density, pH value of the solution, temperature, and agitation.

DC plating mode is the most commonly used mode because of its simple operation and low cost. A few papers have published results of experimental studies of gold-tin plating using the DC mode. Kubota, *et al*, [Kubota 83] reported that when using a solution containing $K_4P_2O_7$, $KAu(CN)_2$ and $Sn_2P_2O_7$, the gold content in the alloy deposit is always higher than gold content in the solution. Tin content in the deposit increased with increasing current density, tending to decrease with the introduction of agitation and an increase in the electrolyte temperature. The phase structure of the deposits was similar to that of metallurgical gold-tin alloys. Tanabe, *et al*, [Tanabe 83] studied the phase structure of gold-tin alloys electrodeposited from an alkaline cyanide solution containing $HAuCl_4$, KCN, and K_2SnO_3. It was found that the solubility of the α solid solution was decreased and the composition range of the intermediate phase ζ was shifted to the Sn side by about 10at% compared with alloys in thermal equilibrium. Holmbom, *et al*,

[Holmbom 98] found in an alkaline cyanide solution containing $Au(CN)_2^-$, SnO_3^{2-}, PO_4^{3-}, CO_3^{2-}, and $(CN)^-$ that Sn content in the deposit was increased by increasing the current density and reduced by increasing agitation, as well as by increasing temperature. The plated gold-tin alloy was crystallographically similar to the bulk material with respect to phase composition.

No other plating mode has been tried to plate gold-tin alloys. It is necessary to consider the plating mode that is being used for gold plating since the gold-tin plating solution developed in Chapter 3 is based on a gold plating system: the chloride-sulfite system. The reasons for this are twofold. One is the alloy to be plated is a gold-tin alloy with tin as the alloying element. The ideal deposit composition for solder application is the eutectic point at 70at%Au-30at%Sn, which is very gold rich. The other is when gold plating is involved, a special complexing agent is needed to stabilize gold, which usually plays a very important role in the performance of the solution. In the history of gold plating, pulse plating has received much attention since the 1970's. Early observations showed that the use of pulsed current in the millisecond range resulted in substantial improvements in density and other properties, such as conductivity and porosity, both in the case of the pure gold and particularly gold alloyed with such metals as cobalt and nickel, which are widely used in the electronics industry. On this basis, further investigation was stimulated by the promise of considerable economy in the usage of the precious metal. Thus far, pulsed gold plating has been applied to obtain high conductivity gold deposits for integrated circuitry, to metallize the substrates for microwave integrated circuits (MIC), to plate high-resistance materials, poorly contacted devices, and extremely small areas, and to selectively plate lead frames for microelectronic packaging [Puipe 86].

The electrodeposition of gold and gold alloys by pulsed current was reviewed by Knodler [Knodler 86]. The earliest studies were conducted by Cheh [Cheh 71], who developed a diffusion model to calculate the deposition rate of metals by a periodic pulsed current, which was extended to calculate the limiting rate of deposition by pulse reverse plating. It was concluded that the advantage of applying pulsed current during electrodeposition is not to increase the limiting overall plating rate, but to raise the pulsed

current density, thereby possibly improving the physical properties through structural modifications of the electrodeposits.

In the review, it was indicated that applying pulsed current could improve microthrowing power and macrothrowing power. The porosity of soft gold deposits was found to be the lowest for pulse plated deposits, followed by asymmetric AC and DC plated deposits, while it is highest for evaporated gold layers. In a weakly acidic gold cyanide bath, it was found that PC plating decreases the current efficiency and increases microhardness of the deposits. A study of the mechanical properties of gold deposits from a phosphate bath revealed that PC plated deposits had an increased tensile strength and elongation, which was explained by the finer grain size and higher purity.

In a study of the effect of PC plating of gold-nickel alloys from an alkaline cyanide bath, a slight increase in the nickel content of PC plated deposits was observed as compared with DC plated deposits. Nickel contents in DC plated deposits were much more sensitive to current density variations than in PC plated deposits.

Much of the later work on pulse plating of gold alloys has been done with acidic cyanide baths in the presence of small amounts of cobalt or nickel as a brightener. Despite purities greater than 98%, gold deposits from these electrolytes have high hardness and wear resistance. For this reason, such deposits are used widely for a finish on electrical contacts. Large amounts of carbonaceous material were detected in DC plated deposits, which was believed to be polymeric hydrocyanic acid precipitated at the cathode during gold plating. The aim of the application of pulse plating was to reduce the codeposition of polymeric inclusions with gold. A study using an acidic citrate plating solution with small additions of either cobalt or nickel showed an increase in the alloy metal content and a decrease in carbon content and current efficiency in PC plated deposits. As the OFF time was increased while the average current density and ON time remained constant, carbon content fell rapidly to low values characteristic of PC plated deposits, becoming constant at certain OFF times. Cobalt contents increase with higher OFF times, also becoming constant at a certain OFF time, while in gold-nickel plating, nickel content continues to rise with increasing OFF time. The explanation for the lower carbon content at longer OFF time is that carbon-containing reaction products, formed during the cathodic current pulse, may diffuse away from the cathode into the bulk of the

solution, thus reducing the possibility of their codeposition in the deposit. There exists sufficient time for the reaction products to attain a stationary concentration in the diffusion layer.

Results of gold-cobalt deposition showed that as the ON time was increased, while pulsed current density and OFF time were held constant, cobalt content decreased linearly while carbon content rose steadily to high values characteristic of DC plated deposits. As temperature is increased, the nickel content rises rapidly in PC plating while under DC plating a similar but less marked increase is observed. Carbon content goes through a minimum at 40°C, which is not observed in DC plating. In gold-cobalt plating, as the temperature rises, cobalt content remains almost constant, while carbon content decreases continuously.

It was found that the current efficiency of gold-cobalt plating steadily decreases as the OFF-time is increased. This result was interpreted in terms of adsorption-desorption modes. Hydrogen is desorbed during OFF times. When a new pulse begins, the surface is less covered with hydrogen than during plating and hydrogen deposition is facilitated, resulting in a lower current efficiency for gold deposition.

PC and pulse reverse plating (PRC) have proven to reduce porosity of gold and gold alloy deposits as the result of structural changes in the deposits. In PC plating, porosity of gold and gold alloy deposits decreases with increasing OFF time, which is attributed to the desorption of hydrogen during OFF time, as porosity is related to the presence of bubbles on the cathode surface during deposition.

The study on the effect of PC plating on the morphology of gold-cobalt showed, at constant pulse time (1ms) and constant PC density (100 mA/cm^2), the grain size of the alloy deposits increases with increasing OFF time. This is in contrast to the results with cadmium deposition where a grain refinement was observed. An investigation on wear resistance of gold-cobalt deposits from DC and PC plating, in a conventional citrate-buffered bath, showed that PC plated coatings had characteristics of abrasive wear by seizure, while DC coatings subjected to the same condition showed only a slight polishing effect with negligible abrasive wear.

In the review, the effect of PRC on the electrodeposition of gold-cobalt alloys from acidic cyanide solutions was also addressed. At low pulse frequencies the carbon content

of PRC plated deposits is significantly lower than that of PC plated layers. The explanation is that during the anodic current pulse the carbon-containing species, which is formed during the cathodic pulse, is desorbed from the cathode, thus being prevented from incorporation into the deposit. At high pulse frequencies, ON and OFF times are too short for diffusion processes to have any significant effect on the composition of the alloy deposits.

From the studies on gold and gold alloy plating, it can be concluded that the large range of experimental conditions for pulse electrolysis leads to a greater variety of results than is possible with DC electrolysis. The optimum conditions for desired coating properties lie in a narrow range that cannot be predicted theoretically. PC plating of gold alloys offers interesting possibilities for achieving an optimum compromise between various characteristics such as ductility, contact resistivity, bondability, and wear resistance.

Based on the solutions developed in Chapter 3, an experimental study of electroplating of gold-tin alloy was carried out to compare DC and PC plating modes for a gold-tin plating system. The effects of various electrolyte parameters (content of gold salt and tin salt in the bath) and operation variables (peak current density, ON time, and OFF time) were also studied to try to find the optimum plating conditions for gold-tin eutectic alloys.

4.2 Experimental Methods

Fig. 4.1 shows the electroplating setup employing a PR0.1-10 pulsed current supply with ON and OFF time settings in the range of 0 - 9.9 ms. A 50 Ω standard resistance R_0 was connected in series with the plating bath to monitor the peak current density in the circuit by monitoring the voltage of the standard resistance using an oscilloscope. The cathodes were either InP or Si wafers, which were coated with a Ti(25nm)/Au(250nm) metallization. A specific exposed plating area of about 1cm×1cm was defined by a stop-off lacquer. A 2cm×1cm piece of platinum foil was used as the anode. A polypropylene sample holder was customized to assure a fixed spacing between the cathode and the

anode. The wafers were cleaned in acetone and the platinum anode was cleaned by cathodic cleaning in a weak HCl acid. The wafers were rinsed in deionized water and then dried.

Deposit composition and microstructure were examined by a Hitachi S-2700 scanning electron microscopy (SEM), with a Link eXL energy dispersive x-ray spectroscopy (EDS) system. Samples were rinsed in deionized water and then cleaned in acetone before microstructure and composition examination. An accelerating voltage of 20keV was used for imaging and EDS. In EDS analysis, pure gold and pure tin standards were used. The operating conditions for EDS were Setting 13 for the coarse beam current, Setting 3 for the aperture, 12mm for the working distance, a Be window for the x-ray detector, and 100 seconds of collection time for each spectrum. Cross sections of cleaved samples were checked by field-emission SEM (FESEM) for deposit thickness measurement. Roughness of the deposits was measured by atomic force microscopy (AFM). Phase analysis of deposits was done by X-ray diffraction (XRD). A Cu target was used as the anode in the XRD analysis. The other XRD analysis conditions included an operating voltage of 40kV, a current of 30mA, a 2θ range of 7° - 90°, a step size of 0.1°, and a dwell time of 4 seconds.

4.2.1 DC and PC plating

Table 4.1 shows the composition of the solutions and the operating variables used for experiments involving the comparison between DC plating and PC plating. Deposit composition and microstructure were examined by EDS analysis and SEM and compared.

4.2.2 Effect of ON time

4.2.2.1 Effect of ON time at constant average current density and cycle period

Solution S4-1 was used to perform PC plating at different ON times, i.e. 0.2, 0.5, 1, 2, 3, 4, and 5 ms. The cycle period was maintained at 10 ms. The average current density was 2.4 mA/cm^2, and the plating time was 1 hr. Deposit composition was determined by EDS analysis. Surface roughness was checked using a scanning probe microscope controller (AFM: Nanoscope E, Digital Instrument) with a Si_3N_4 tip. The scan size was 14.94μm and the scan rate was 2.001hz.

4.2.2.2 Effect of ON time at constant peak current density and OFF time

Thirty mL of Solution S4-1 was used to perform PC plating at different ON times, i.e., 0.5, 1, 2, 3, and 4 ms. InP wafers were used for 2 and 3 ms ON times while Si wafers were used for the other ON settings. The same metallization was used for both wafers. The peak current density was kept at 10 mA/cm^2, and the plating time and OFF time were 80 min and 8 ms, respectively. In order to estimate the density of the deposits and current efficiency of the plating process, the weight gain after plating was checked by a microgram balance. Deposit composition was determined by SEM EDS analysis. Cleaved cross sections were examined and thickness measurements were made in the FESEM. Phase structure of the deposit was analyzed by XRD.

4.2.3 Effect of OFF time

Thirty mL of Solution S4-1 was used to perform PC plating at different OFF times, i.e. 9.9, 8, 6, 4, and 3 ms. The peak current density was kept at 10 mA/cm^2, and the plating time and ON time were 80 min and 2 ms, respectively. Deposit composition was determined by SEM EDS analysis. Cleaved cross sections were examined and thickness

measurements were made in the FESEM. Phase structure of the deposit was analyzed by XRD.

4.2.4 Effect of various electrolyte parameters

Series 1

Experimental Series 1 was designed to examine the effect of the ratio of gold and tin content in the bath on the deposit composition. Solutions with different ratios of gold and tin salts and the pulse plating parameters used in this part are listed in Table 4.2.

Series 2

Experimental Series 2 was designed to examine the effect of the total concentration of gold and tin salts in the bath on the deposit composition. Solutions with different total concentration of gold and tin salts and the pulse plating parameters used in this part are listed in Table 4.3.

4.3 Results and Discussion

4.3.1 DC and PC plating

The deposit composition results are plotted in Fig. 4.2 and the corresponding microstructures for DC and PC deposits obtained from Solution S4-1 are shown in Fig. 4.3. The composition vs. current density tendencies are similar for DC and PC plating. The Sn content in deposit first increases with increasing average current density; then a plateau is reached in the Sn content vs. current density curve within a certain current density range. Beyond this range, the Sn content decreases with increasing current density. The initial increase in the curve can be explained by the results of polarization curve measurements in Chapter 3. It was shown in Fig. 3.4 that tin is plated at a more

negative cathodic potential than gold. This means tin plating is favored by a more negative cathodic potential, which can be obtained with a much higher current density setting. Therefore, the higher the current density, the more negative the cathodic potential, which favors tin plating and results in higher Sn content in the deposit. However, with a further increase in the average current density, hydrogen evolution becomes significant, which decreases the current efficiency of alloy plating. Hydrogen deposition may cause a locally higher pH value, where tin ions become more likely complexed by $(OH)^-$ ions to form an $Sn(OH)^-$ complex, which has a stability constant of 10^{10}. There is another possible explanation for this decrease of Sn content with increasing current density. Because of the local change of hydrogen ion concentration due to the hydrogen deposition, more ammonium citrate will dissociate into NH_3 and hydrogen ions according to Equation (3.3) to play the role of maintaining a constant pH value as a buffering agent. A higher NH_3 concentration in the bath arises. The (NH_3) can form complexes with both tin ions and gold (III) ions in the solution according to the discussion of the polarization behavior of tin solution and gold solution shown in Fig. 3.1 and Fig. 3.2 in Section 3.3.2. Since the gold ions are mainly in the form of a gold(I) sulfite complex, (NH_3) does not influence gold plating as much as tin plating. Therefore tin ions will be further stabilized as a result of the higher (NH_3) concentration in the solution at higher current density and tin plating is suppressed in this way, giving rise to a lower tin content in deposit with increasing current density.

From Fig. 4.2, it can be seen that DC deposits at the same current densities are consistently lower in Sn content. This result is similar to that found in some other gold alloy pulse plating systems, e.g., gold-cobalt and gold-nickel pulse plating systems [Knodler 86]. This may be due to a different polarization behavior in DC mode compared with PC mode. When the same average current density is used in DC and PC plating, the way the cathodic potential responds to the current density in DC and PC mode may be different so that the cathodic potential in PC mode is more negative relative to that in DC mode. From the polarization curve measurement in Chapter 3, it was found that tin is plated at more negative cathodic potential than gold. This means tin plating is favored by a more negative cathodic potential. If possible a transient test should be performed to

examine the response of the cathodic potential to an application of a high constant current density for a duration time in the range of several milliseconds.

Comparing the microstructures of PC deposits in Fig. 4.3, it is obvious that the higher the average current density (because of higher peak current density), the larger the grain size. At 2.0 and 2.4 mA/cm^2 current density, PC deposits have needle-like fine grains while at 2.8 mA/cm^2, the grains are coarser. This observation is different than the result of Rehrig [Puipe 86], who found in the plating of soft gold that at low peak current density, the grain size increased with the duration of the pulse. At higher peak currents and a duty cycle less than 50%, the grain diameter was inversely proportional to the peak current and the duration of the pulse. It is found in this work that the deposit microstructure is not only affected by the plating parameter, but also by the deposit composition. When the deposits are gold-rich compared with the eutectic composition, the deposits are generally very bright and shiny and the grains are unresolvable in the SEM. The microstructure comparison between deposits should be made when the deposit compositions are very close. The comparison result is also related to the range of plating parameter studied, e.g., average current density.

The DC and PC deposits have the same microstructure tendency with current density in the range of 2.0 to 2.8 mA/cm^2. In this range, the compositions of DC and PC deposits are all tin-rich compared with the eutectic composition. This tendency for DC deposits can be explained easily since a higher current density in DC plating is closer to the limiting current density, where a coarser structure is more likely to form. The same tendency found in PC deposits can also be explained as follows. When the average current density in PC plating is increased, it is approaching the limiting average current density, resulting in a coarser microstructure.

Comparing the microstructures of DC and PC deposits as shown in Fig. 4.3, at current densities ranging from 1.6 to 2.0 mA/cm^2, the microstructures are similar, while at higher current densities (>2.0 mA/cm^2), deposits from PC plating are denser and finer. At low average current density, PC plating has no obvious influence on deposit microstructure. However, at higher average current density, the PC mode has an obvious influence on deposit microstructure. When a duty cycle of 20% and the same average current density are used in PC plating as for DC plating, the peak current density is equal to (average

current density/20%), e.g., five times the average current density according to Equation (2.50). Therefore the peak current density for PC plating is usually considerably higher than the corresponding current density for DC plating. If the average current density is much smaller than the limiting current density, the higher peak current density results in finer deposit structure because the rate of electron transfer to form adatoms is much faster than the diffusion rate of the adatoms across the surface to positions in the lattice.

As described in Chapter 2, in pulse electrolysis there are two distinct diffusion layers (see Fig. 2.24) related to two kinds of limiting current densities in PC plating. The depletion of the cationic concentration in the pulsating diffusion layer limits the pulse current density, and the depletion of the cationic concentration in the outer diffusion layer limits the average current density. Since the concentration gradient in the pulsating diffusion layer can be very high, and increasing with shorter pulse length, the pulse current density can reach extremely high values, e.g., up to 10000 times the usual DC values, without a decrease in current efficiency due to hydrogen evolution. As long as the pulse duration time is shorter than the transition time, the average current density used in PC plating will not exceed the DC limiting current density and PC deposits may have finer grain structure than DC deposits when the same average current density is used.

Grain refinement in pulse plating is also favored by the enhancement of nucleation rates due to high overpotentials which result from high peak current densities. Grain refinement was quite often observed in other plating systems, e.g. a phosphate gold plating bath [Puipe 86].

Sample edge effects in PC plating at average current densities of 2.0, 2.8 and 3.2 mA/cm^2 are shown in Fig. 4.4. At higher current density, edge effects are more pronounced than that at lower average current density. The actual current density at the edge is higher than the current density setting. Therefore, as the higher the average current density setting is increased, the actual current density approaches the limiting peak current density, and the deposits are more likely to have characteristic microstructures of limiting current conditions, such as coarse grains and dendrites.

From the work in this section, it is concluded that in the range of the average current density studied, PC plating using Solution S4-1 has advantages over DC plating. PC

deposits at higher average current densities have a finer and denser microstructure than DC deposits under otherwise identical plating conditions.

4.3.2 Effect of ON time

4.3.2.1 Effect of ON time at constant average current density and cycle period

The deposit composition results obtained at different ON times are plotted in Fig. 4.5 and the microstructures of deposits at ON times of 1, 2, 3, and 4 ms are shown in Fig. 4.6. The 3-dimensional AFM images for these four ON-time settings are shown in Fig. 4.7.

The deposit composition curve first increases with increasing ON times, then forms a plateau for ON times of 1- 4 ms and finally decreases with a further increase in ON time. The plateau in the compositional curve is favorable for plating practice since the working window for plating parameters can be wider. Since this series of experiments was done under the conditions of constant current density and constant cycle period, when ON time is increased, there is actually a decrease in the peak current density and OFF time. Therefore this curve and all the microstructural characteristics in this part are the results of the combined effects of these three factors. If the ON time is too short, e.g., 0.2 and 0.5 ms, the charging effect or capacitance effect of the cathode is very obvious. The faradaic current for alloy plating is substantially lower than the peak current setting. This may result in lower tin content in the deposit. At a long ON time setting, e.g., 5 ms, the peak current density is quite low, which is favorable for gold plating. For example, at 5 ms of ON time, the peak current density is 4.8 mA/cm^2, which is one fifth of the peak current density at 1 ms of ON time. ON time is an important parameter in PC plating. For pure metal pulse plating, ON time should be shorter than the transition time, otherwise hydrogen evolution or organic decomposition may occur. The transition time τ, pulse current density i and metal concentration C in the bath have the relationship shown in Equation 2.46. Hydrogen evolution decreases the current efficiency while organic decomposition causing carbon plating destroys the deposit by increasing the deposit

resistance. For alloy pulse plating, the mechanism is far more complicated than that for pure metal pulse plating. It is possible that for each component there is a transition time.

From the SEM micrographs in Fig. 4.6, the deposits obtained at 2 ms of ON time have the densest structures, finest grain size and smoothest deposits. This result is also confirmed by the 3-dimensional AFM images shown in Fig. 4.7 and roughness measurement. Deposit surface mean roughness for 1, 2, 3, and 4 ms ON times measured by AFM are 73.8nm, 58.4nm, 64.1nm, and 62.9nm, respectively. The mean roughness R_a is defined as the mean value of the surface relative to the center plane.

$$R_a = \frac{1}{L_x L_y} \int_0^{L_x} \int_0^{L_y} |f(x,y)| dxdy \qquad (4.1)$$

where f(x,y) is the surface relative to the center plane and L_x and L_y are the dimensions of the surface. The values of the mean roughness for the deposits obtained at 1 - 4 ms of ON times are very small and fairly close. This means the deposits have very smooth and uniform surface morphology.

4.3.2.2 Effect of ON time at constant peak current density and OFF time

The weight gain of the deposits after plating, deposit composition obtained by SEM EDS analysis, and thicknesses measured in the FESEM are listed in Table 4.4.

Estimation of Current Efficiency

Current efficiency (CE) is the percentage of the total current used to plate the alloy. It can be calculated according to Equation (4.2).

$$CE = \frac{Q_{Sn} + Q_{Au}}{i_p \times \gamma \times S \times t} \qquad (4.2)$$

i_P is the peak current density, γ is the duty cycle, S is the sample area, t is the plating time, and Q_{Sn} and Q_{Au} are the charge used for Sn plating and Au plating respectively. Since the deposit thickness (d) and composition (C) are known from the experimental results in Table 4.4, the charge Q_{Sn} and Q_{Au} can be calculated according to the following equation

$$Q_i = nF\frac{d \times S \times \rho \times C}{A_i} \tag{4.3}$$

where n is the number of electrons transferred to reducing a metal ion, F is the Faraday constant (96,488C), C is the weight percentage of the metal in the deposit, A_i is the atomic weight of the metal, i, being plated, and ρ is the density of the deposit. For the Au-16.7at%Sn deposit obtained at 1 ms of ON time, the density of the deposit is calculated to be 16.5 g/cm^3 according to equation (4.4). For the Au-39.5at%Sn deposit obtained at 3 ms of ON time, its density is calculated to be 12 g/cm^3 according to equation (4.4), in which ρ_{AuSn} and ρ_{Au5Sn} are the densities of AuSn and Au_5Sn with values of 11.7 and 17.1 g/cm^3, respectively.

$$\rho_{deposit} = \frac{A_{AuSn} + A_{Au5Sn} \times \dfrac{1-2C_{deposit}(at\%)}{6C_{deposit}(at\%)-1}}{\dfrac{A_{AuSn}}{\rho_{AuSn}} + \dfrac{A_{Au5Sn} \times (1-2C_{deposit}(at\%))}{\rho_{Au5Sn} \times (6C_{deposit}(at\%)-1)}} \tag{4.4}$$

For Sn plating, n is equal to 2. For gold plating, if the reduction reaction is Au(I) → Au, then n is equal to 1, while if the reduction reaction is Au(III) → Au, n will be 3. Since a sulfite gold-tin plating bath is used, most likely the gold reduction reaction is Au(I) → Au. Deposit composition obtained from SEM EDS analysis was given in atomic percent. It can be converted into weight percent, according to the following (for tin):

$$C(wt\%) = \frac{C(at\%) \times A_{Sn}}{C(at\%) \times A_{Sn} + (1 - C(at\%)) \times A_{Au}} \qquad (4.5)$$

where A_{Sn} and A_{Au} are the atomic weights for Sn and Au.

The calculated results for current efficiency are shown in Table 4.4. The major source of the error in the calculated current efficiency includes the error in the assumed deposit density and the thickness measured in the FESEM. Since the deposits usually have porous structures, the actual density of the deposit may be lower than the assumed value. The thickness of the deposits is not uniform. The standard deviation in thickness may be substantial. The errors in the sample area, peak current density and deposit composition also contribute to the final results of calculated current efficiency. The calculated current efficiency is quite low(<65%), no matter which gold reduction reaction is assumed. The current efficiency at 3 ms of ON time is lower than that at 1 ms of ON time. This result can be explained using the polarization curve of Solution SAuSn. When a substantial amount of current density is consumed by Sn plating (between Point B and D in Fig. 3.4(a)), hydrogen deposition also consumes a substantial amount of current density. The average current density at 3 ms of ON time is $10\times(3/(3+8)) = 2.7$ mA/cm^2, while at 1 ms of ON time, it is $10\times(1/(1+8)) = 1.1$ mA/cm^2. The average current density at 3 ms of ON time is much higher than that at 1 ms of ON time. The higher the average current density used, the more current is consumed by hydrogen evolution, resulting in lower current efficiency.

Composition

The Sn content in deposit vs. ON time is plotted in Fig. 4.8. The Sn content in the deposits increases with increasing ON time for short ON times, reaches a plateau and then decreases with a further increase in ON time. The rising edge of the plateau in the curve may be explained by the transition time for gold plating. When the ON time is longer than about 0.5 ms, Au plating becomes a diffusion controlled process and Sn plating or hydrogen deposition initiates. From this it can be estimated that the transition time for Au plating is about 0.5 ms. When ON time is increased to about 2 ms, both gold

plating and tin plating likely become diffusion controlled, resulting in a composition plateau in the curve. With a further increase in ON time, hydrogen deposition increases and the local pH value may increase. This may result in the formation of a $Sn(OH)^-$ complex or higher (NH_3) content in the bath arising from dissociation of $(NH_4)^+$ ions to buffer the pH value of the solution. These two possible consequences suppress Sn plating by stabilizing Sn ions in the form of a Sn complex.

Microstructure

The SEM micrographs of deposits obtained at different ON times are shown in Fig. 4.9. The deposit obtained at 1 ms of ON time has a very fine structure and bright appearance. It is quite different compared with other deposits obtained at 2 to 4 ms of ON times in deposit microstructure. This difference results mainly from the difference in deposit composition. The deposit obtained at 1 ms of ON time is Au-16.7at%Sn, while the deposits obtained at 2 to 4 ms of ON time have tin contents over 33at%. Comparing the deposits obtained at 2 to 4 ms of ON times, the deposits obtained at short ON times have a finer structure and brighter appearance. This is because at short ON times, but the same peak current density, the deposit thickness is thinner. The thickening effect is not dominating. Therefore, the grains are very fine. At longer ON times, however, the average current density is higher and the thickening effect is obvious; grains becomes coarser. At 4 ms of ON time, the microstructure of the deposit is already close to the characteristic structure at the DC limiting current density.

The cleaved cross section images for the deposits in Fig. 4.9 are shown in Fig. 4.10. The deposit at 1 ms of ON time has the features of a ductile fracture. The composition of this deposit is gold rich, which should be ductile. For the deposits obtained at 2 ms and 3 ms of ON time, the deposit/wafer interfacial adhesion is very good. No cracks or pores are found along the interface. The deposits are very dense. The thickness of the deposit at 3 ms of ON time is greater than that at 2 ms of ON time. If a closer look is taken at the grains, it is found that the grain size is smaller in the region closer to the deposit/wafer interface and the grains gradually grow coarser along the thickness direction in a columnar manner. This phenomenon is very similar to that in a solidification process of liquid metal on a cold surface, e.g., casting. The fractured surfaces of these two deposits

have the similar features of a brittle fracture. The compositions of these two deposits are almost the same, Au-39at% Sn, which is Sn rich compared to the eutectic point, Au-29.5at% Sn. This explains the structural similarity. The deposit obtained at 4 ms of ON time is very rough and has an extremely scattered thickness distribution, ranging from 1.4 to 8.9 μm. This is because the average current density in this case is very high, 3.3 mA/cm^2, which is likely very close to the limiting current density.

From the above discussion, ON times of 1 - 3 ms are good for practical plating in terms of deposit microstructure. Their plating rate ranges from 0.7 - 1.7 μm/hr. This deposition rate should be suitable for plating Au-Sn solder for laser chip bonding, while faster rates may be needed to produce Au-Sn bumps in microelectronic applications. Faster plating rates could be achieved by using higher gold and tin contents in the bath to increase the limiting current density.

Phase Analysis

XRD spectra for the deposits obtained at different ON times are shown in Fig. 4.11.

From the Au-Sn phase diagram in Fig. 2.2(b), it can be seen that for a gold-tin alloy with Sn content between 16-50at%, Au_5Sn and AuSn are expected.

Since the sampling depth of the x-ray in XRD analysis is deeper than the thickness of the deposits obtained at 0.5 and 1 ms of ON times, i.e. 0.3 and 1μm, respectively, substrate peaks ((400) for Si and (200) and (400) for InP) show up in the spectra. The gold (111) and (222) peaks are likely from the metallization layer under the deposit, and from the deposit itself. The gold shows a (111) preferred orientation. The main phase in the deposit at 0.5 ms of ON time is Au_5Sn, which exhibits a (001) preferred orientation parallel to the deposit surface. A small amount of AuSn is present. For the 1 ms ON time, Au_5Sn remains the main phase with a less pronounced (001) preferred orientation compared with the 0.5 ms sample. A significant amount of AuSn is present with a slight (110) preferred orientation parallel to the surface. The second strong peak for Au_5Sn is (113).

Although the thickness of the deposit at 2 and 3 ms of ON time are already 1.6 and 2.3 μm, the substrate and Au metallization peaks still appear in the spectra. However, their intensities are much lower in the deposit at 3 ms of ON time than those at 2 ms of

ON time. In both deposits, AuSn is the main phase with (110) preferred orientation parallel to the surface. For Au_5Sn, (006) and (113) are the two strongest peaks. The (113) peak is a little stronger in the deposit at 3 ms of ON time than the peak (006), while at 2 ms of ON time, the (006) peak is a little stronger that the (113) peak. The intensity ratio of the strongest peaks of AuSn and Au_5Sn is further increased in the deposit at 3 ms of ON time compared with those deposits obtained at 0.5, 1, and 2 ms of ON times.

For the 4 ms ON time sample, substrate and Au metallization peaks still appear. This is because the deposit is not uniform in thickness as shown in Fig. 4.10. The deposit is very thin in places. The main phase is AuSn with a strong (110) preferred orientation parallel to the surface. Peaks at (100) and (102) are the next most intense. Only Au_5Sn (113) peak was detected. It is difficult to conclude whether the gold peaks come from the deposit.

The change of the strongest Au_5Sn peak from (006) at short ON times, e.g., 0.5 and 1 ms to (113) at longer ON times, e.g. 3 ms, is an interesting phenomenon. The strongest AuSn peak also changes from (210) at 0.5 ms of ON time to (110) at 1 to 4 ms of ON times. This phenomenon is likely related to the possibility that different crystal orientations are favored by different crystallization overpotential and have different growth rates.

From the above discussion, it can be concluded that the phases in these electrodeposits are all crystalline. For gold-rich deposits, the main phase is Au_5Sn, while for the deposits which have compositions close to the eutectic point, the main phases are Au_5Sn and AuSn. With an increase in ON time, the Au_5Sn to AuSn ratio decreases.

4.3.3 Effect of OFF time

Composition

The effect of OFF time on deposit composition is shown in Table 4.5 and Fig. 4.12.

The tin content in the deposit first increases with increasing OFF time for short OFF times, i.e., 3 - 4 ms. With a further increase in OFF time, the tin content remains constant in the 6 - 9.9 ms OFF time range. There is a sharp increase in the curve. This is because

at the end of the ON time, the tin ions are depleted at the cathode. During the OFF time, the concentration of tin ions is recovered before the next pulse to some extent by diffusion of the tin ions from the bulk solution to the depletion region. The extent of recovery depends on the length of OFF time. The longer the OFF time, the higher the concentration of tin ions at the cathode at the beginning of the next pulse, resulting in a higher tin content in the deposit. However, if the OFF time is long enough, the concentration of tin ions at the cathode at the beginning of the next pulse reaches the maximum value, which is the bulk concentration. In this situation, a further increase in OFF time has no influence on the deposit composition.

Microstructure

The SEM top views of the deposits obtained at different OFF times are shown in Fig. 4.13. When 3 ms of OFF time is used, the deposit has a very loose structure and is black in color. This implies a very high carbon content in the deposit. It is because the OFF time is too short for the Sn and Au concentration at the cathode to return to the bulk value, resulting in a diffusion controlled plating condition. Also 3ms of OFF time is too short for organic compounds at the cathode to diffuse away. It is understandable that the shorter the OFF time, the closer the microstructure of a PC deposit is to that of a DC deposit. PC deposits will lose the advantage of a finer grain size at very short OFF time.

The deposit obtained at an OFF time of 4 ms has a coarser structure and a much greater thickness than the deposits obtained at OFF times of 9.9, 8, and 6 ms, although they have very similar compositions. It seems that an OFF time of 4 ms is still too short. For OFF times ranging from 6 ms to 9.9 ms, the grain size in the deposits is almost the same. This result arises from the fact that the OFF times from 6 - 9.9 ms are long enough for the reacting species to recover, however, the range of OFF times examined is too small to see the effect of OFF time on microstructure. If the effect of OFF time is to be studied, a wider OFF time setting should be used.

In the literature about metal pulse plating [Puipe 86], it has been reported that an increase in OFF time results in grain refinement for cadmium, but in grain growth for copper and for gold. The explanation is that for copper and gold, grain growth occurs

during the OFF time. Larger grains are thermodynamically more stable. For cadmium, the observed opposite trend in grain size is most likely due to blocking of growth centers on the cathode during the OFF time as a result of adsorption of the inhibiting species.

Cleaved cross section images for the deposits obtained at 9.9 and 4 ms of OFF times are shown in Fig. 4.14. The thickness of these two deposits is 1.6 and 7.6 μm, respectively. The average current density for the deposit at an OFF time of 4 ms is two times that of the deposit at an OFF time of 9.9 ms, however, the deposit thickness at an OFF time of 4 ms is more than four times that of 9.9 ms OFF time deposit. Both of the deposits at 4 ms and 9.9 ms OFF times have a columnar structure, while the deposit at 4 ms OFF time is less dense.

Phase Analysis

The XRD spectra for the deposits obtained at OFF times of 8, 6, 4, and 3 ms are shown in Fig. 4.15. It was found that the spectra for (b) 6 ms and (d) 3 ms were shifted to the left by ~1.5° and to the right by ~1°, respectively, which may arise from the positioning system error of the x-ray detector. The following results are obtained from the corrected spectra. The main phase in the deposit at an OFF time of 8 ms is AuSn with only one strong peak at (110). Peaks of gold (111) and (222) are also present. These peaks are likely from the deposit itself and from the gold layer under the deposit. The only two Au_5Sn peaks present are at (006) and (113) with approximately the same intensities. Compared with 8 ms OFF time deposit, in the deposit at 6 ms OFF time, AuSn is still the main phase. Besides the strongest AuSn (110) peak, many other AuSn peaks appear and the AuSn (100) peak is the second strongest peak for AuSn. The Au_5Sn (006) and (113) peaks remain the two strongest peaks with approximately the same intensities. In the deposit at 4 ms OFF time, Si and gold peaks appear, possibly as a result of non-uniformity in the deposit thickness. AuSn is the main phase in the deposit with (100), not (110), as the strongest peak. The AuSn (110) peak becomes the second strongest peak. There are also other AuSn peaks present. The intensity of the Au_5Sn (113) peak is significantly higher than that of the Au_5Sn (006) peak. In the spectrum for the deposit at 3 ms OFF time, gold is the main phase with a (111) preferred orientation. The gold peaks are likely from the gold layer under the deposit since the deposit is very loose.

Since the intensity of the Si peaks is very weak, most gold must exist in the deposit. The deposit contains AuSn with the strongest peak at (110). No Au_5Sn peaks were detected. A small peak at 2θ of 36.6° has not been identified. This peak might come from the inclusions in the deposit since the deposit is black in color, which means there is a relatively high carbon content in the deposit. The average current density for the 3 ms OFF time deposit is 4 mA/cm^2, which is fairly high and close to the limiting average current density. The presence of AuSn as the main phase is understandable; while why pure gold is plated out is not clear.

Comparing the spectra for the different OFF times, it is found that at long OFF times, e.g., 8 ms and 6 ms, the deposits exhibit a strong preferred orientation for the main phase AuSn. This may be due to the long OFF time that is favorable for grain growth. In the course of grain growth, only the grains with the most thermally stable crystal orientation can grow larger and other grains will dissolve and be incorporated in the favorable orientated grains. At short OFF times, there is not enough time for the growth of the most favorably orientated grains during the OFF time. Grains with various crystal orientations co-exist in the deposit, resulting in the presence of many peaks in the spectrum of short OFF time deposits, e.g., 4 ms.

From above analysis, it is concluded that as the OFF time decreases from 8 ms to 4 ms, the intensity of the peak AuSn (100) increases and becomes the strongest peak for AuSn instead of (110) at an OFF time of 4 ms. The Au_5Sn phase present in these deposits has (113) and (006) as the strongest peaks. The Au_5Sn (006) peak completely disappears at 4 ms OFF time.

When the OFF time decreases to 3 ms, gold with a (111) preferred orientation is the main phase in the spectrum. Since only a small Si(400) peak from the wafer is detected, it can be concluded that gold is present in the deposit. AuSn is present with (110) as the strongest peak. As explained above about the effect of OFF time on deposit composition, if OFF time is too short, the concentration of Sn ions at the cathode is low due to short recovery time, the Sn content will be low in the deposit. However, since the same peak current density and ON time were used at different OFF times, AuSn other than Au_5Sn remains to be one of the main phases in the deposit. The reason for it is that the cathode

potentials at the same peak current density, but different OFF times, are lowered to approximately the same range, which favors AuSn plating.

4.3.4 Effect of electrolyte parameters

Series 1

The effect of the gold to tin salt content ratio (R) is shown in Fig. 4.16.

From Fig. 4.16, it is apparent that the curves peak at a certain average current density. The maximum point depends on the solution used. Solution S4-2 has the highest tin content at the peak. The tendency is that a higher tin content in the bath results in a higher tin content in the deposit at the peak position. This phenomenon has been discussed in Section 4.3.1. Higher tin content in the bath gives a better working window of average current density.

Series 2

The results of deposit composition vs. average current density for Solutions S4-1, S4-5, S4-6 and S4-7 are plotted in Fig. 4.17.

Solutions S4-1, S4-5 and S4-7 have gradually increased gold salt content. The maximum tin content in the deposit decreases with increasing gold content in bath. Comparing the curves for Solution S4-1 and S4-6, it is found that a higher total content of gold and tin salts in the bath results in a lower tin content in the deposit.

4.4 Conclusions

In this chapter, DC plating and PC plating of gold-tin alloys in the developed chloride-sulfite solutions were carried out and compared. In the studied range of average current density, PC deposits have consistently higher Sn content than DC deposits. At relatively low average current densities, i.e. less than 2.4 mA/cm^2, the grain sizes of the

PC deposits are similar to that of the DC deposits, while at higher average current densities, i.e., greater than 2.4 mA/cm^2, the PC deposits have a much finer structure and smoother surface.

The effect of ON time was studied at two different conditions. When the average current density and cycle period are held constant, deposit composition vs. ON time curve has a plateau. The deposit obtained at 2 ms of ON time has the finest structure and smoothest surface. This observation is actually the result of the combined effects of peak current density and OFF time. In the second case, the peak current density and OFF time are held constant and the ON time is an independent variable. The deposit composition curve also has a plateau. The microstructure of the deposit depends on the deposit composition. When the deposit is gold-rich compared with the eutectic composition, the grain structure is very fine and the deposit is bright and shiny. When the deposit composition is comparable, e.g., for the deposits obtained at 2 ms to 4 ms ON times, the grain structure is finer for shorter ON times. When the ON time is too long, e.g., 4 ms, the deposit has a microstructure characteristic of DC deposits. The longer the ON time, the smaller the difference between PC plating and DC plating. XRD phase analysis shows that the electrodeposits are consistently crystalline. The phase structure is close to the equilibrium phase structure of the gold-tin binary system. Au_5Sn and AuSn are present in the deposits and these phases exhibit preferred orientation which changes with the ON time.

The effect of OFF time was also studied when the peak current density and ON time were held constant. The Sn content in the deposits first increases with increasing OFF time and then reaches a plateau. Microstructural examination shows that at very short OFF times, e.g. 3 - 4 ms, the grains are very coarse since PC plating is actually approaching DC plating conditions. For OFF times of 6 - 9.9 ms, no microstructural difference is found in the deposits.

The effect of selected electrolyte parameters was examined. Higher Sn content in the bath results in a higher tin content in the deposits. Higher total content of gold and tin salts in the bath results in a lower tin content in the deposits.

The plating rates under which pulse plating has been studied are about 0.7-1.7 μm/hr, which is suitable for laser bonding applications involving gold-tin alloys.

Table 4.1 Solutions and plating conditions utilized for DC and PC plating.

	DC Plating		PC Plating
Solution	S4-1	200 g/L Ammonium citrate 5 g/L $KAuCl_4$ 60 g/L Sodium sulfite 15 g/L L-ascorbic acid 5 g/L $SnCl_2.2H_2O$ 1 g/L $NiCl_2$	S4-1
Average current density (mA/cm^2)	2.0, 2.4, 2.8, 3.2, 3.6		1.6, 2.0, 2.4, 2.8, 3.2, 3.6
Other plating parameters			ON time = 2ms OFF time = 8ms Duty cycle = 20%
Plating time (hr)	1		1
Temperature (°C)	24		24

Table 4.2 Solutions and pulse plating parameters used in Series 1.

	Ratio of gold and tin salts	Ammonium citrate (g/L)	$KAuCl_4$ (g/L)	Na_2SO_3 (g/L)	L-ascorbic acid (g/L)	$SnCl_2.2H_2O$ (g/L)	$NiCl_2$ (g/L)
S4-2	0.5	200	5	60	30	10	1
S4-3	1.0	200	5	60	30	5	1
S4-4	2.0	200	10	60	30	5	1
Plating condi-tions	ON time = 1 ms; OFF time = 9 ms; average current density range from 1.3 to 5.1 mA/cm^2; room temperature; plating time 80 min.						

Table 4.3 Solutions and pulse plating parameters used in Series 2.

	Ammonium citrate (g/L)	$KAuCl_4$ (g/L)	Na_2SO_3 (g/L)	L-ascorbic acid (g/L)	$SnCl_2.2H_2O$ (g/L)	$NiCl_2$ (g/L)
S4-1	200	5	60	15	5	1
S4-5	200	7	60	15	5	1
S4-6	200	7	60	15	7	1
S4-7	200	10	60	15	5	1
Plating condi-tions	ON time = 2 ms; OFF time = 8 ms; average current density range from 1.6 to 3.6 mA/cm^2; room temperature; plating time 80 min.					

Table 4.4 Deposit composition and thickness results at different ON times.

ON time (ms)	Deposit appearance	Sample area (cm^2)	Estimated current efficiency (%)		Thickness (μm)	Deposit composition (at%Sn)		
			Au(I) →Au	Au(III) →Au		Area-1	Area-2	Area-3
0.5	Bright				0.3	10.2	10.5	
1	Bright	0.38	24.9	61.3	1.0	16.3	17.0	
2	Semi-bright				1.6	41.0	38.9	
3	Semi-bright	0.48	22.7	42.5	2.3	39.4	39.6	39.4
4	Dull				Non-uniform	32.5	34.9	33.4

Table 4.5 Deposit composition at different OFF times.

OFF time (ms)	Deposit appearance	Thickness (μm)	Deposit composition (at% Sn)		
			Spot-1	Spot-2	Spot-3
9.9	Semi-bright	1.6	37.4	36.9	37.8
8	Semi-bright		37.0	36.3	37.5
6	Semi-bright		37.5	37.3	38.3
4	Dull	7.6	35.2	34.9	35.4
3	Black & loose		24.6	22.9	24.3

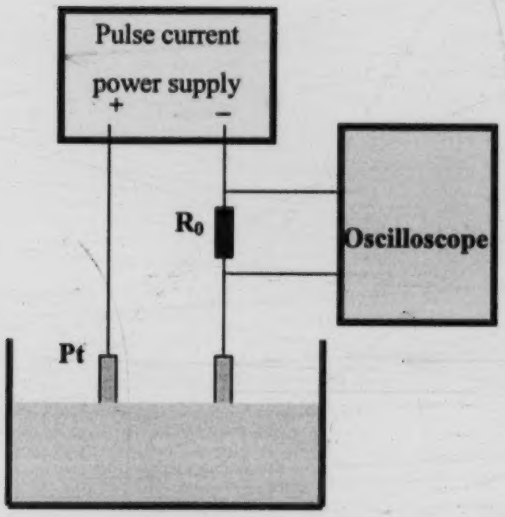

Fig. 4.1 Electroplating setup.

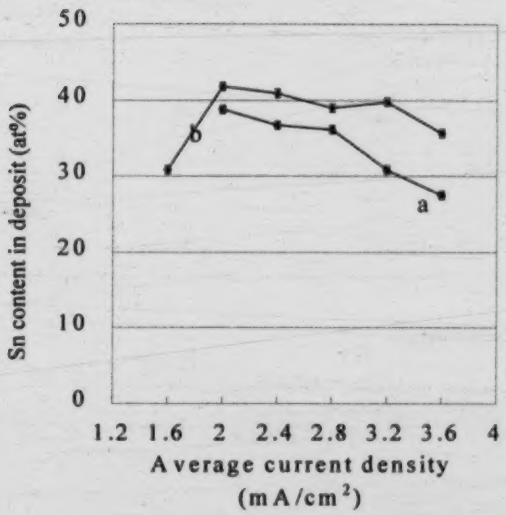

Fig. 4.2 Sn content in deposit vs. average current density for DC (a) and PC (b) plating in Solution S4-1. The ON time and OFF time for PC plating are 2 ms and 8 ms, respectively. The error bar corresponds to the standard deviation in the composition measurements at three different locations for each sample.

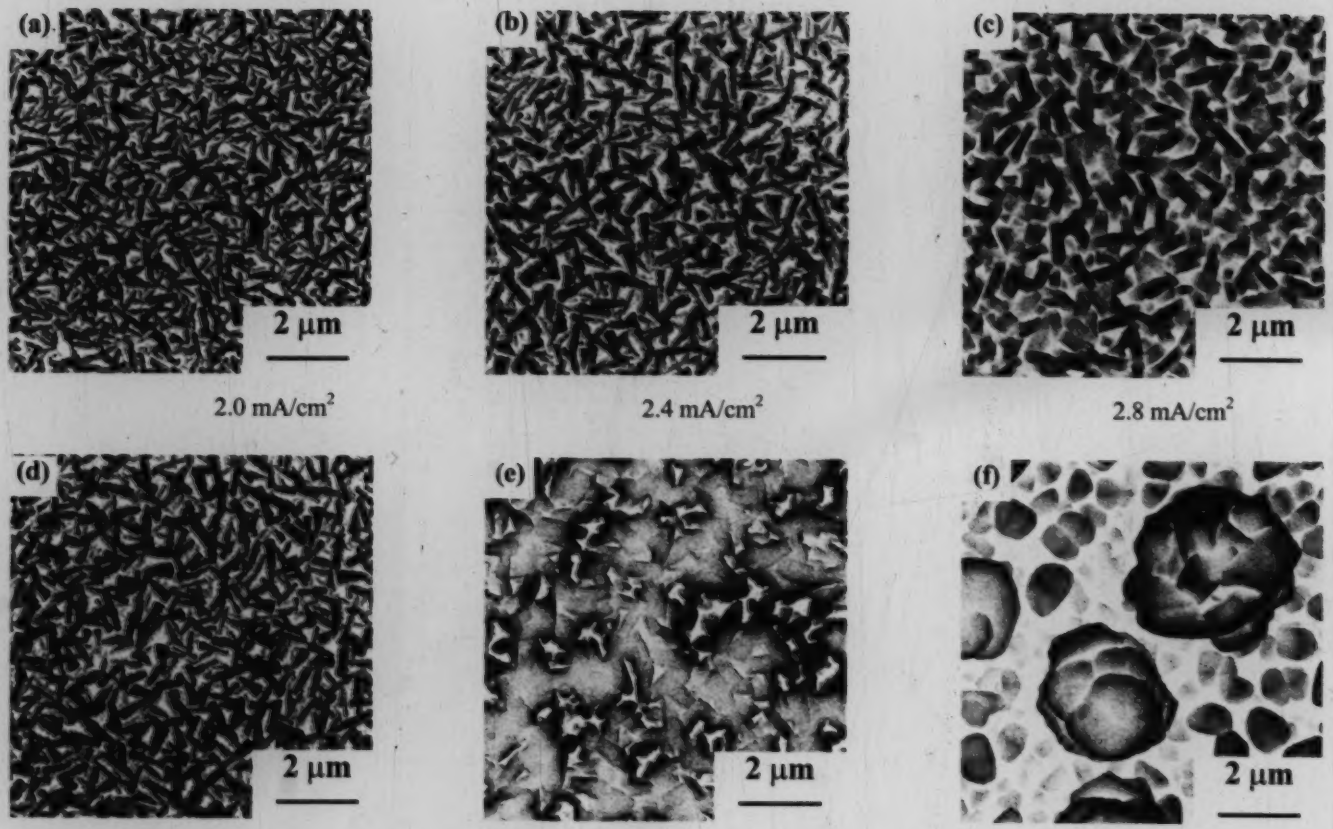

Fig. 4.3 SEM top-view images for PC plated deposits (a-c) and DC plated deposits (d-f). The ON time and OFF time for PC plating are 2 ms and 8 ms, respectively.

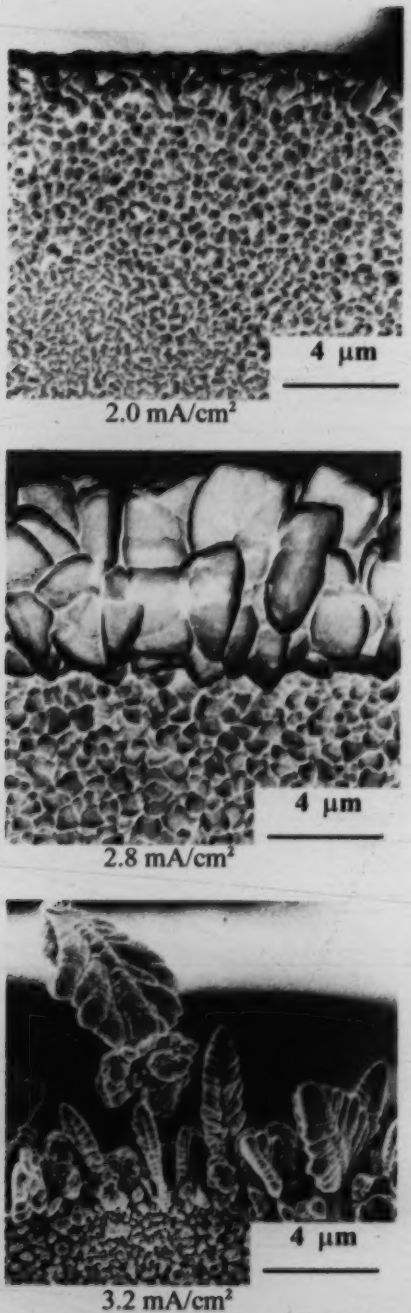

Fig. 4.4 Edge effects (SEM) in PC plating at current densities of 2.0, 2.8 and 3.2 mA/cm^2. The ON time and OFF time are 2 ms and 8 ms, respectively.

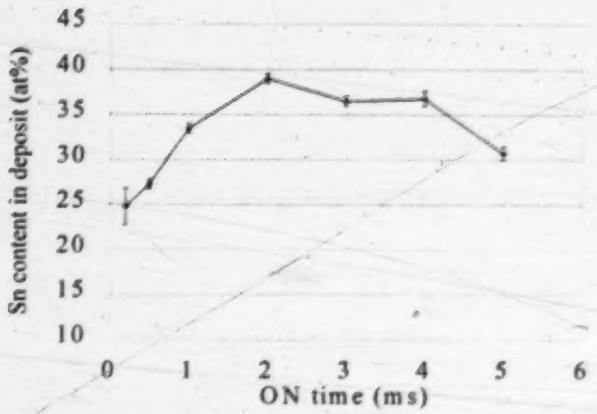

Fig. 4.5 Effect of ON time in PC plating on deposit composition at the constant average current density of 2.4 mA/cm^2 and cycle period of 10 ms. The error bar corresponds to the standard deviation in the composition measurements at three different locations for each sample.

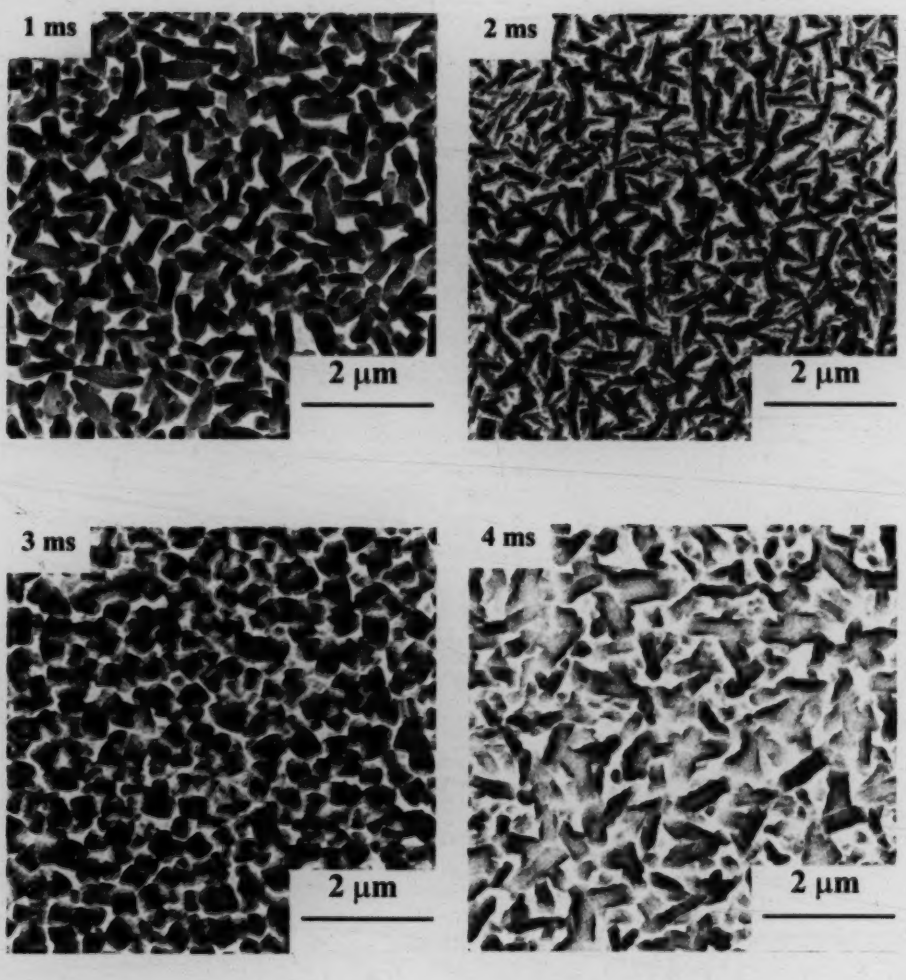

Fig. 4.6 SEM images for PC deposits at various ON times at the constant average current density of 2.4 mA/cm^2 and cycle period of 10 ms.

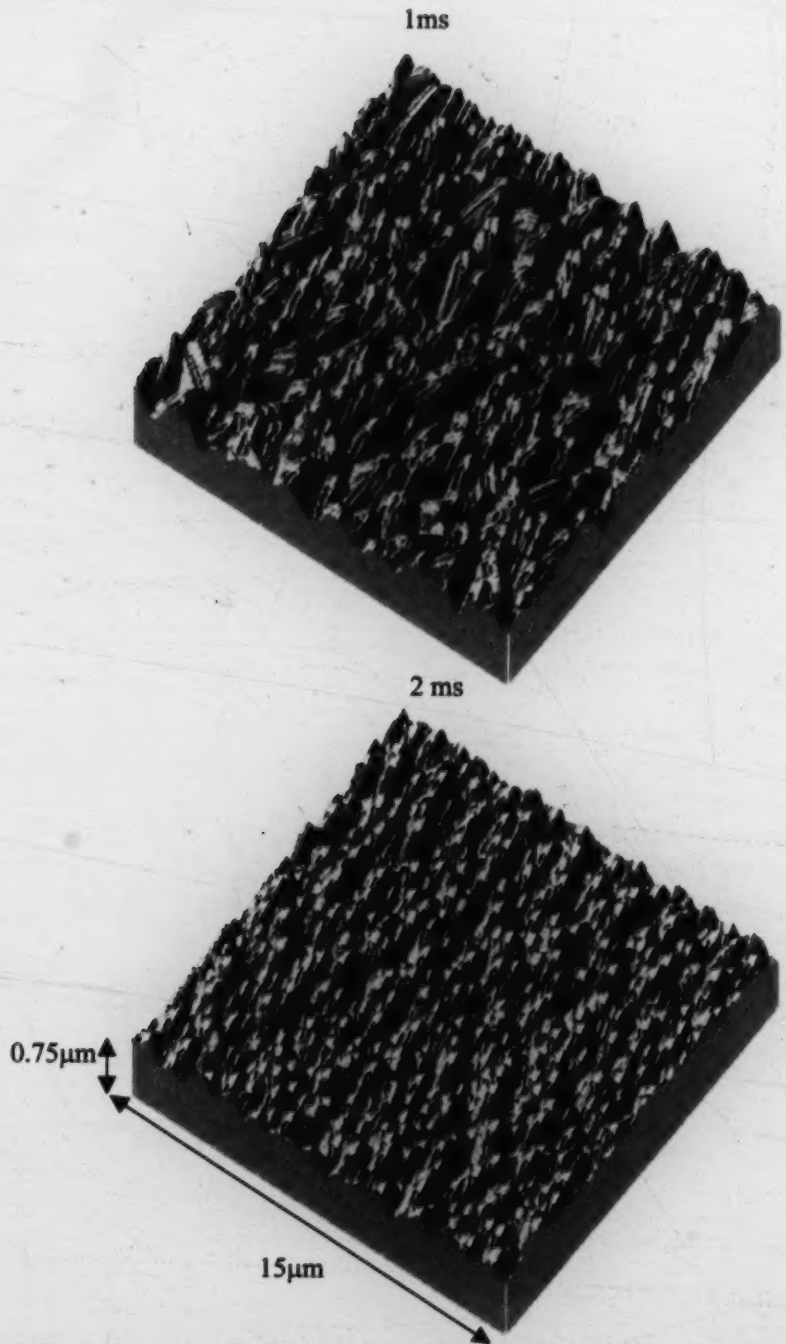

Fig. 4.7 Three-dimensional AFM images for PC deposits at various ON times at the constant average current density of 2.4 mA/cm^2 and cycle period of 10 ms (to be continued).

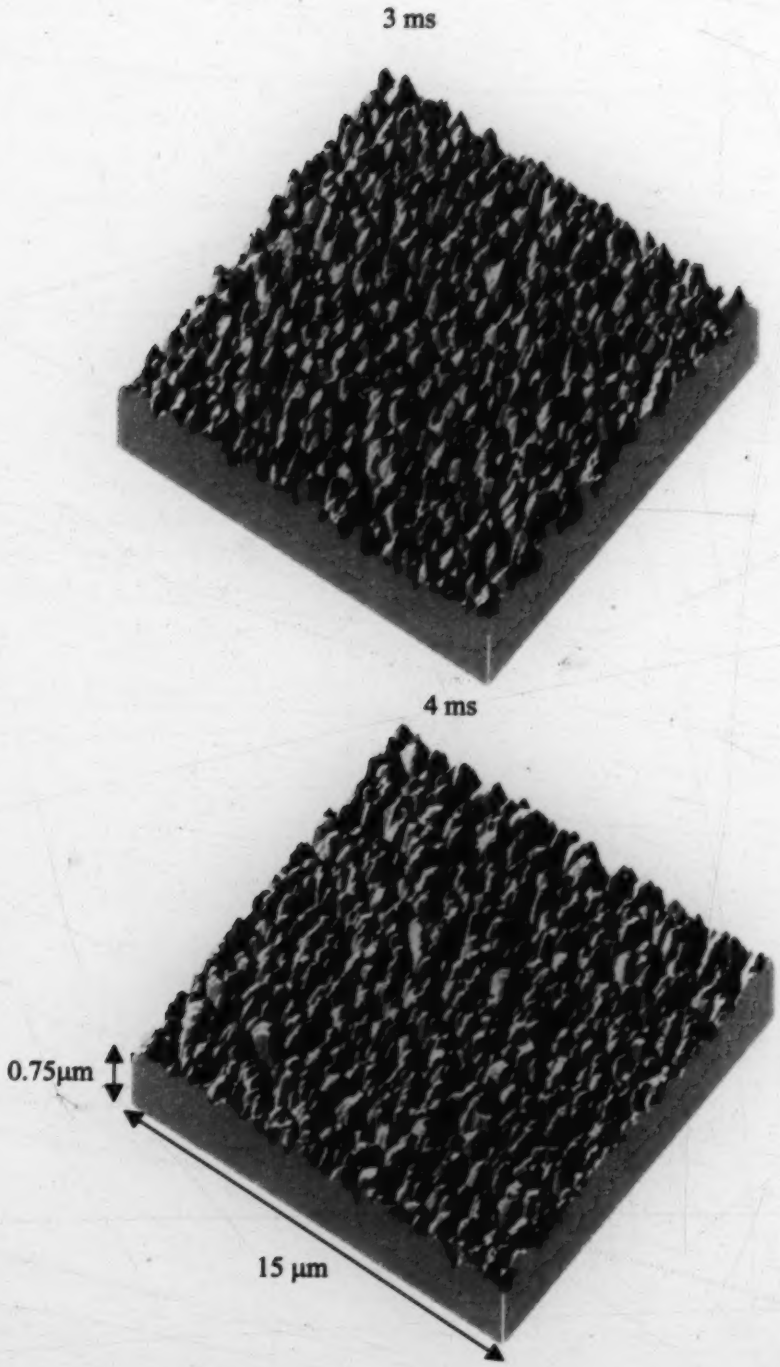

Fig. 4.7 Three-dimensional AFM images for PC deposits at various ON times at the constant average current density of 2.4 mA/cm^2 and cycle period of 10 ms (continued).

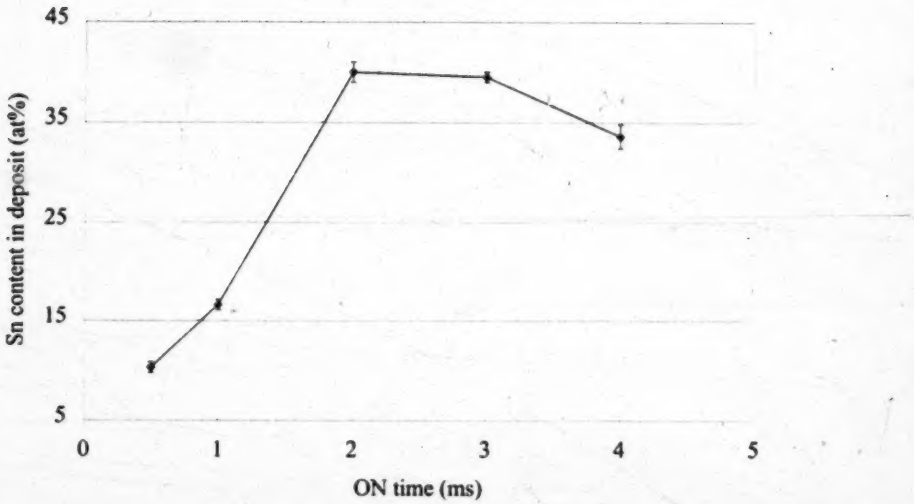

Fig. 4.8 The effect of ON time on deposit composition at a constant peak current density of 10 mA/cm^2 and OFF time of 8 ms. The error bar corresponds to the standard deviation in the composition measurements at three different locations for each sample.

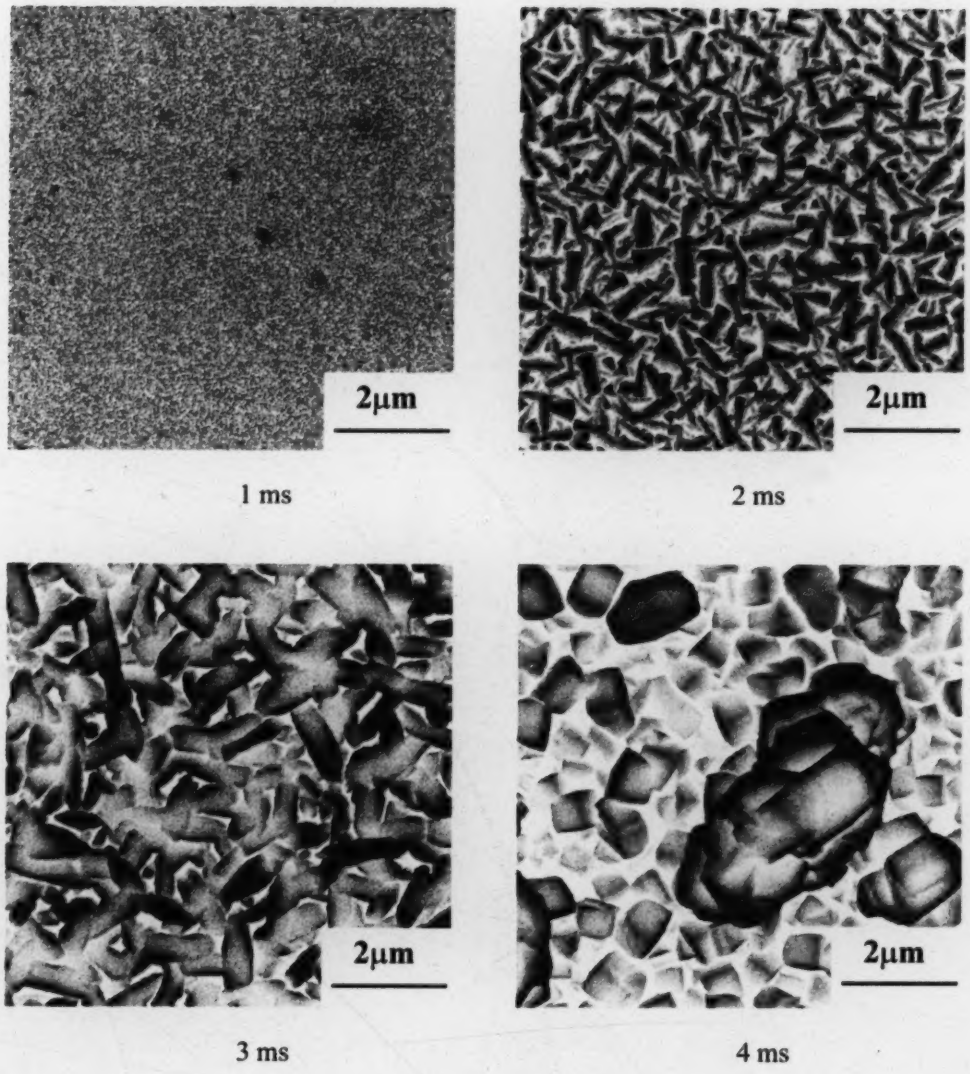

Fig. 4.9 SEM top views of the deposits obtained at ON times of 1, 2, 3, and 4 ms at a constant peak current density of 10 mA/cm^2 and OFF time of 8 ms.

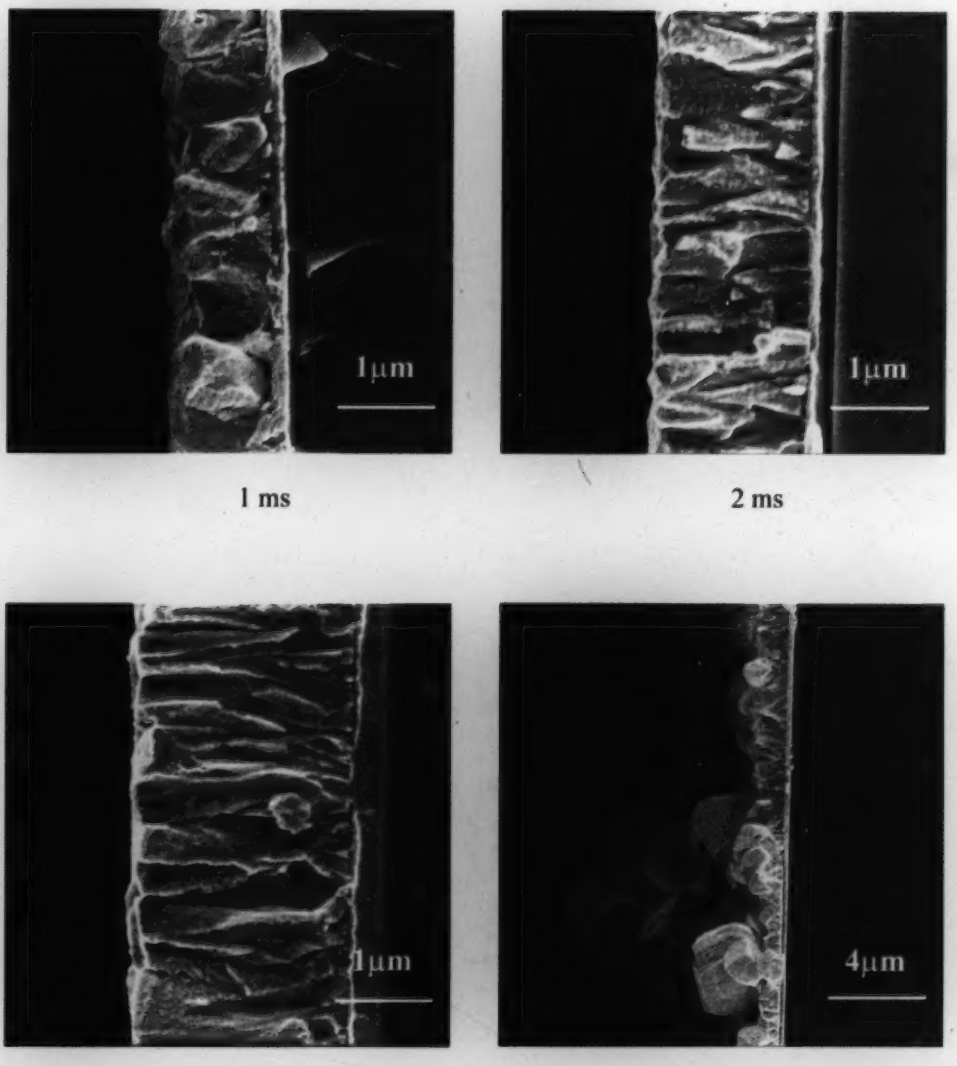

1 ms 2 ms

3 ms 4 ms

Fig. 4.10 Cleaved cross-section images of the deposits obtained at different ON times at a constant peak current density of 10 mA/cm^2 and OFF time of 8 ms.

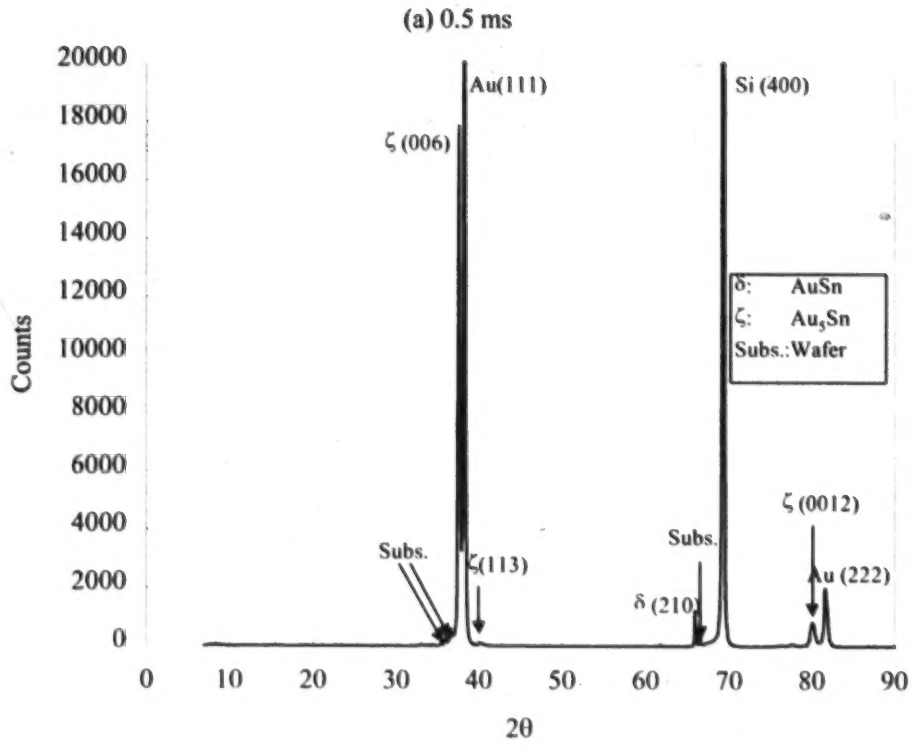

Fig. 4.11 XRD spectra for the deposits obtained at (a) 0.5, (b) 1, (c) 2, (d) 3, and (e) 4 ms ON times at a constant peak current density of 10 mA/cm^2 and OFF time of 8 ms (to be continued).

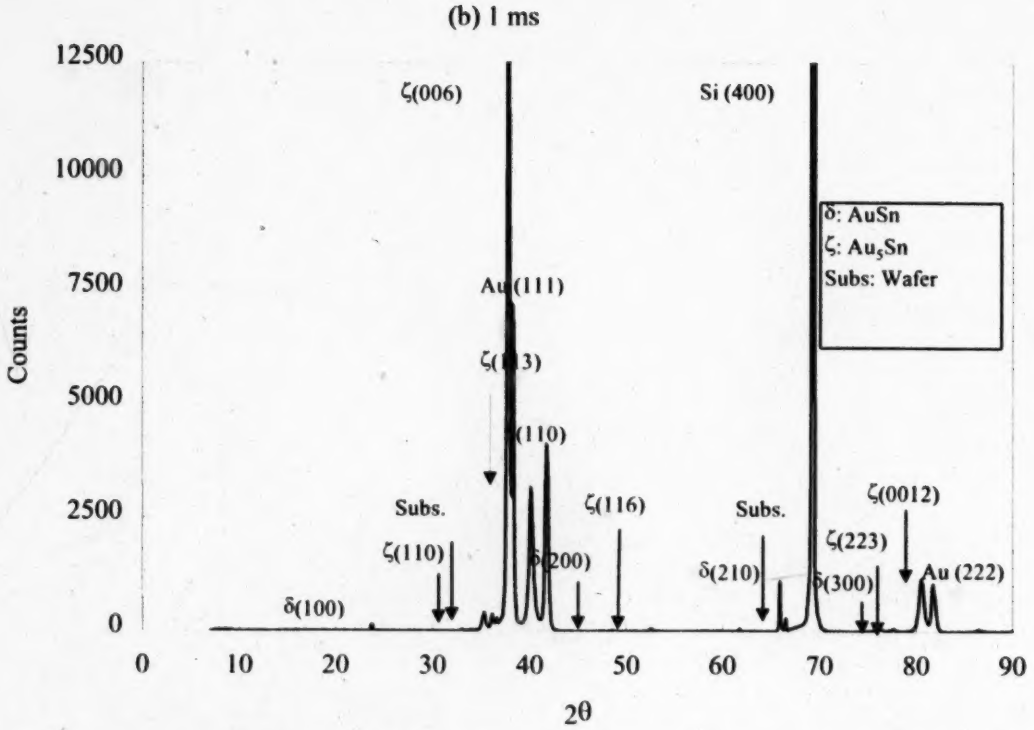

Fig. 4.11 XRD spectra for the deposits obtained at (a) 0.5, (b) 1, (c) 2, (d) 3, and (e) 4 ms of ON times at a constant peak current density of 10 mA/cm^2 and OFF time of 8ms (to be continued).

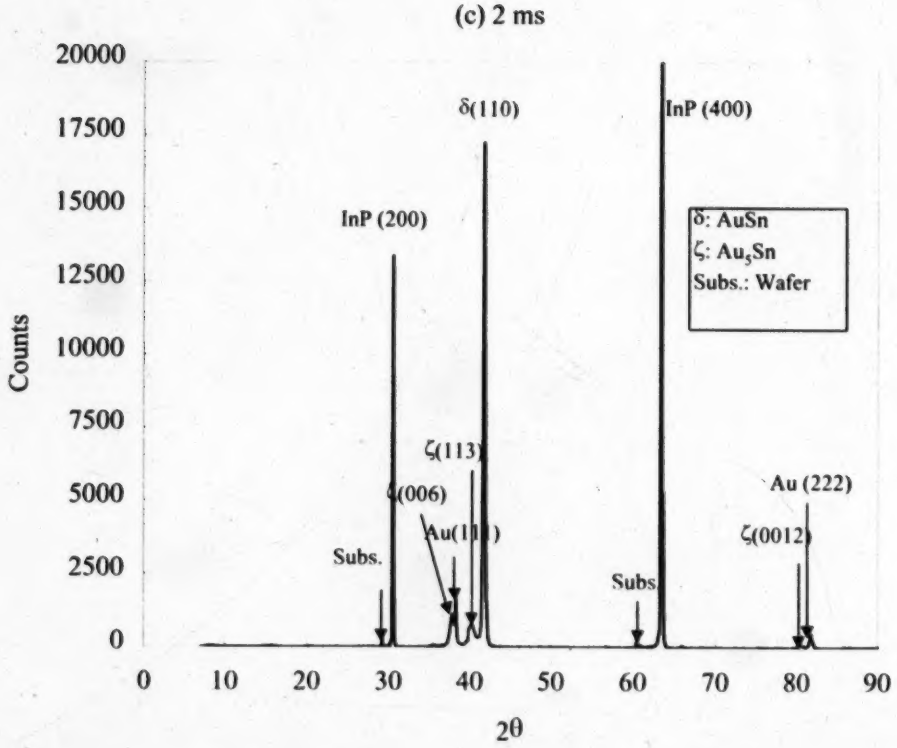

Fig. 4.11 XRD spectra for the deposits obtained at (a) 0.5, (b) 1, (c) 2, (d) 3, and (e) 4 ms ON times at a constant peak current density of 10 mA/cm^2 and OFF time of 8 ms (to be continued).

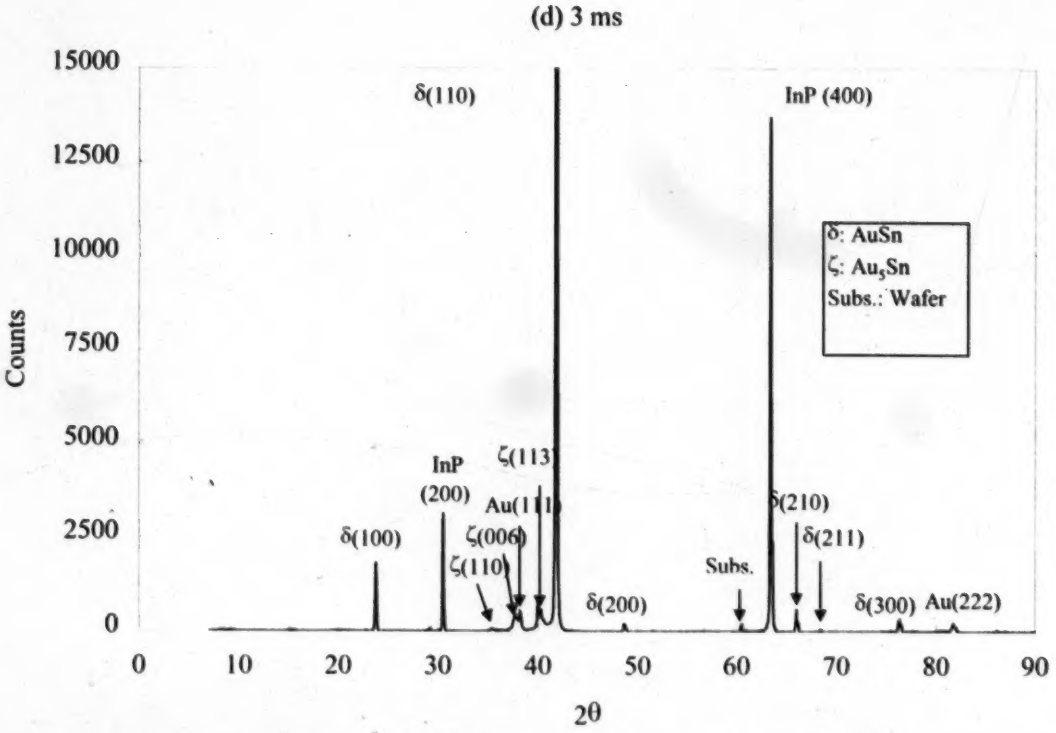

Fig. 4.11 XRD spectra for the deposits obtained at (a) 0.5, (b) 1, (c) 2, (d) 3, and (e) 4 ms ON times at a constant peak current density of 10 mA/cm^2 and OFF time of 8 ms (to be continued).

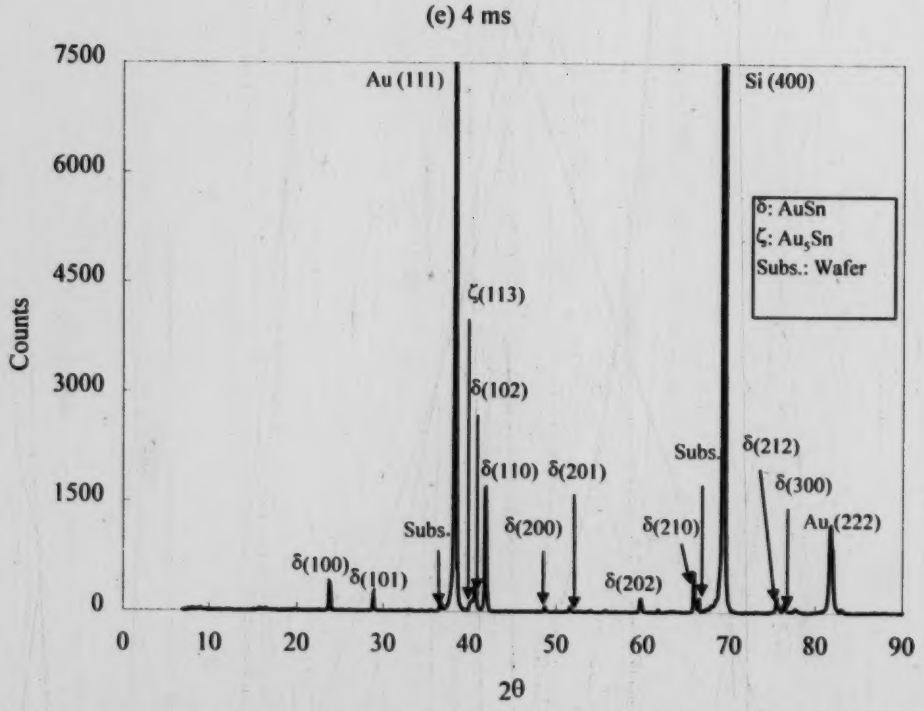

Fig. 4.11 XRD spectra for the deposits obtained at (a) 0.5, (b) 1, (c) 2, (d) 3, and (e) 4 ms ON times at a constant peak current density of 10 mA/cm^2 and OFF time of 8 ms.

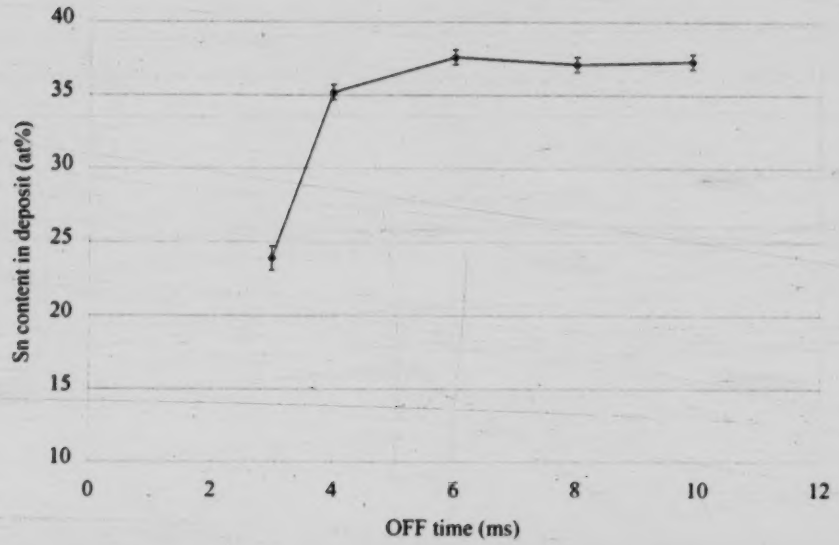

Fig. 4.12 Deposit composition at different OFF times. The peak current density is constant at 10 mA/cm^2 and the ON time is 2 ms. The error bar corresponds to the standard deviation in the composition measurements at three different locations for each sample.

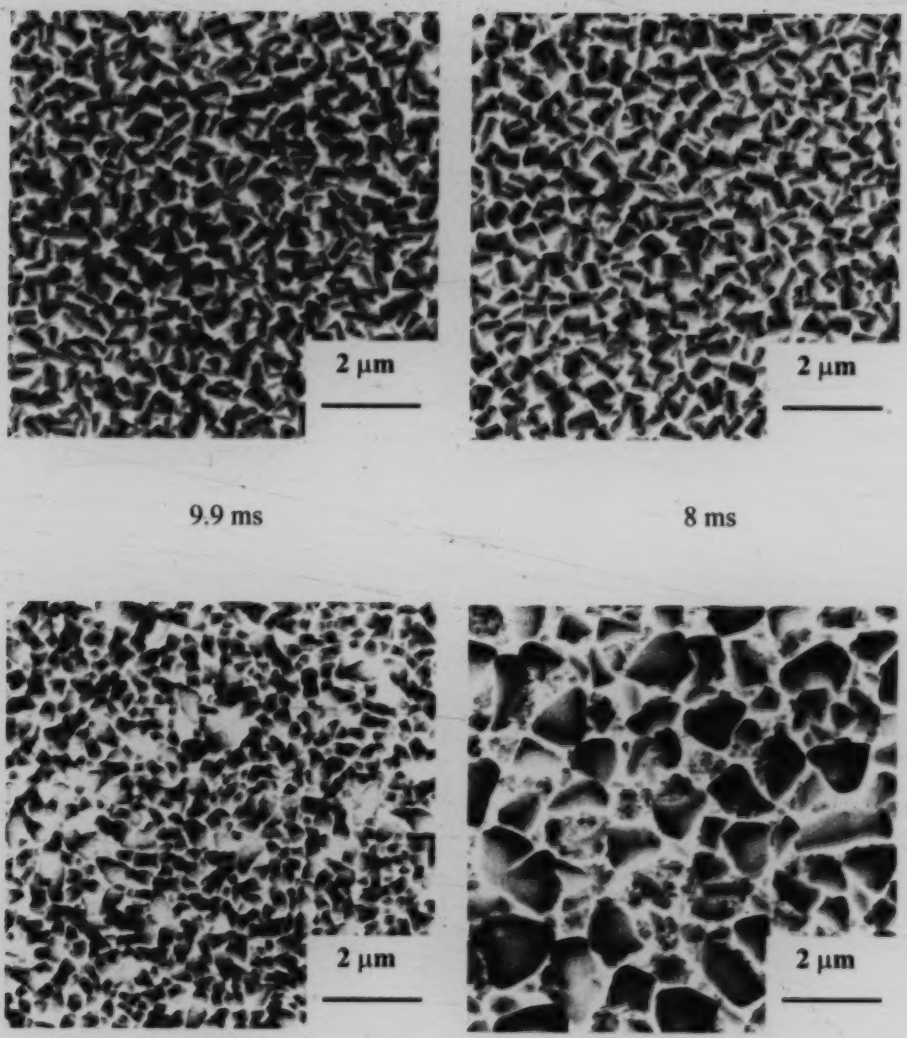

Fig. 4.13 SEM top view images of the deposits obtained at different OFF times, while the peak current density is kept constant at 10 mA/cm^2 and the ON time is 2 ms.

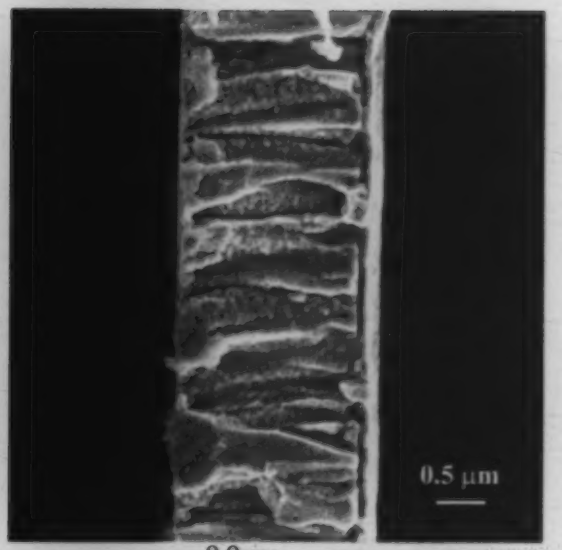

9.9 ms

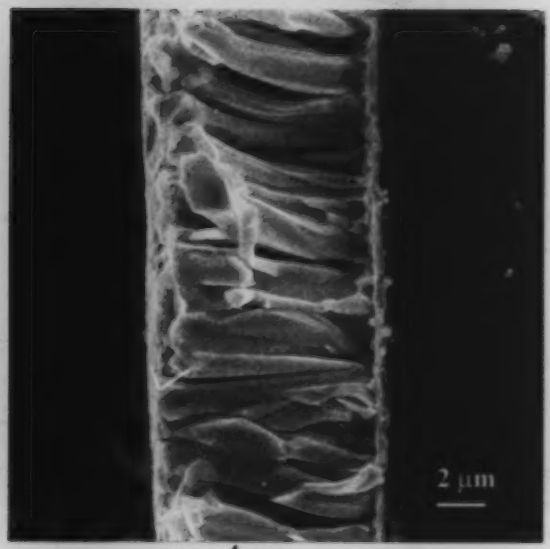

4 ms

Fig. 4.14 Cleaved cross section images of the deposits obtained at OFF times of 9.9 ms and 4 ms, while the peak current density is kept constant at 10 mA/cm^2 and ON time is 2 ms.

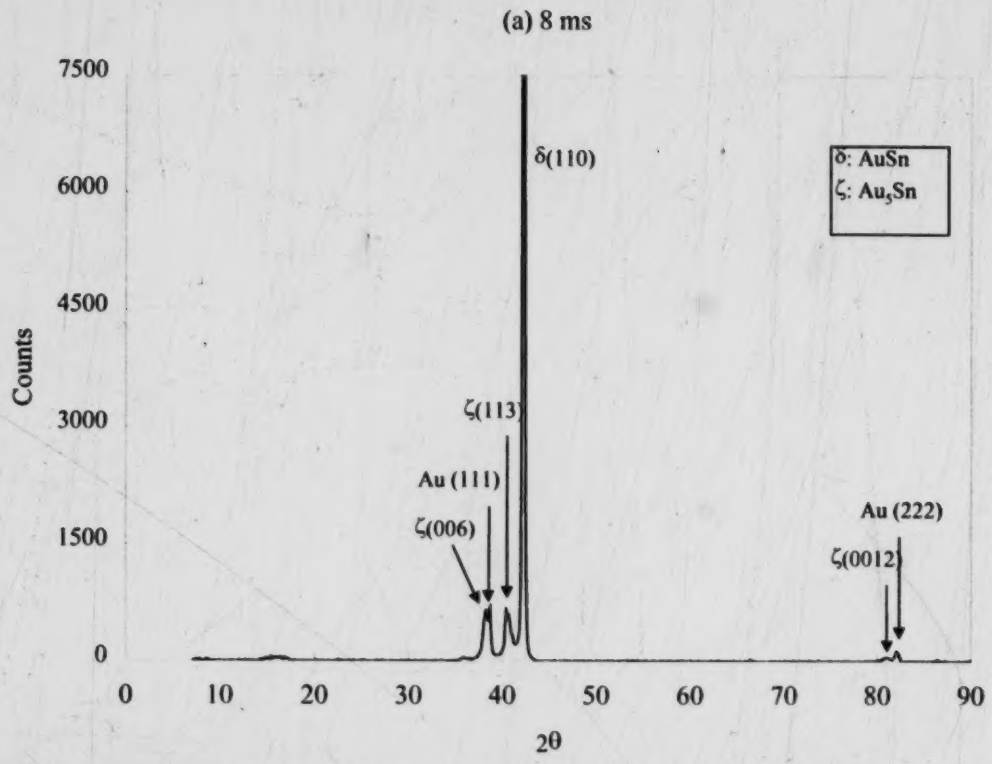

Fig. 4.15 XRD spectra for the deposits obtained at OFF times of (a) 8, (b) 6, (c) 4, and (d) 3 ms (to be continued) .

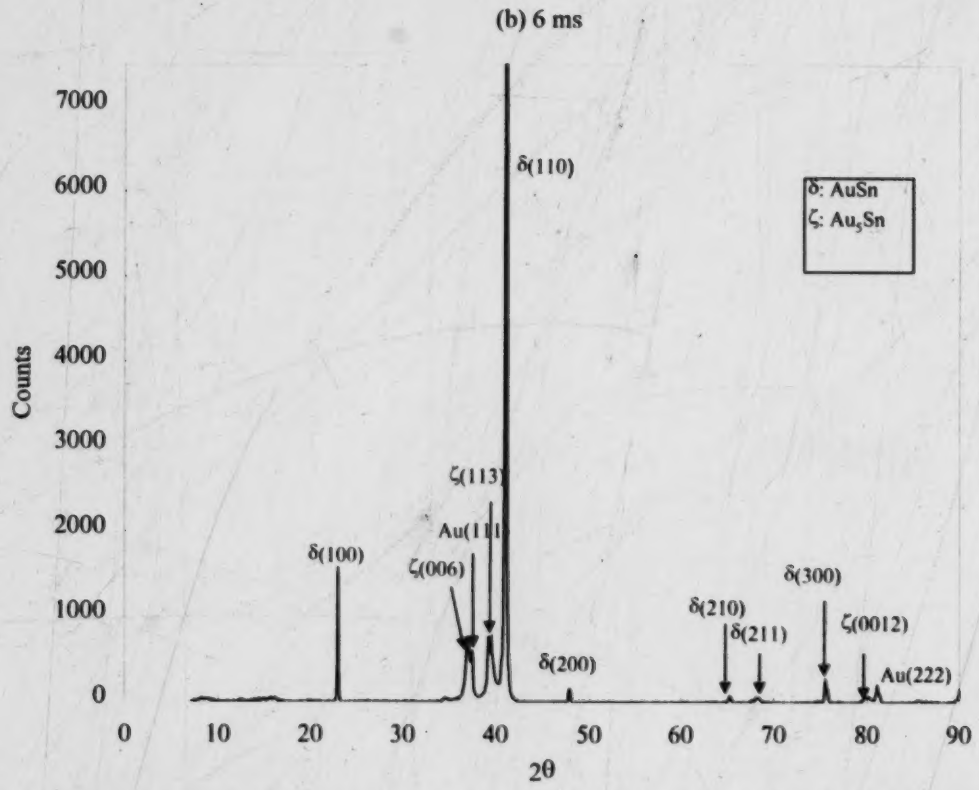

Fig. 4.15 XRD spectra for the deposits obtained at OFF time of (a) 8, (b) 6, (c) 4, and (d) 3 ms (to be continued).

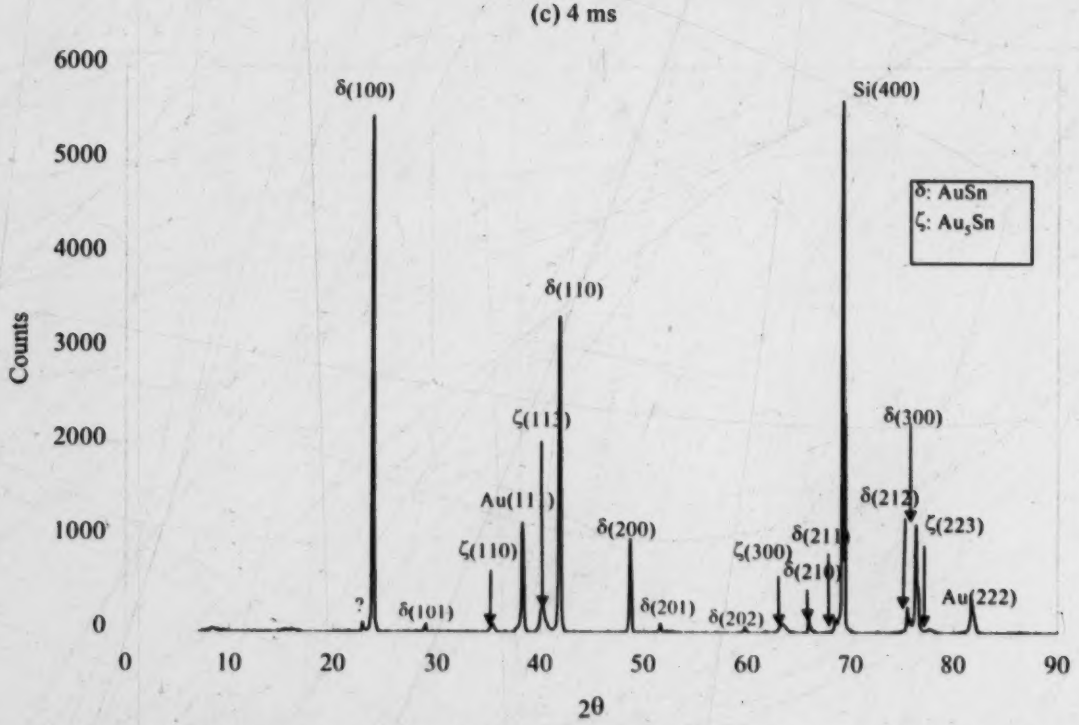

Fig. 4.15 XRD spectra for the deposits obtained at OFF times of (a) 8, (b) 6, (c) 4, and (d) 3 ms (to be continued).

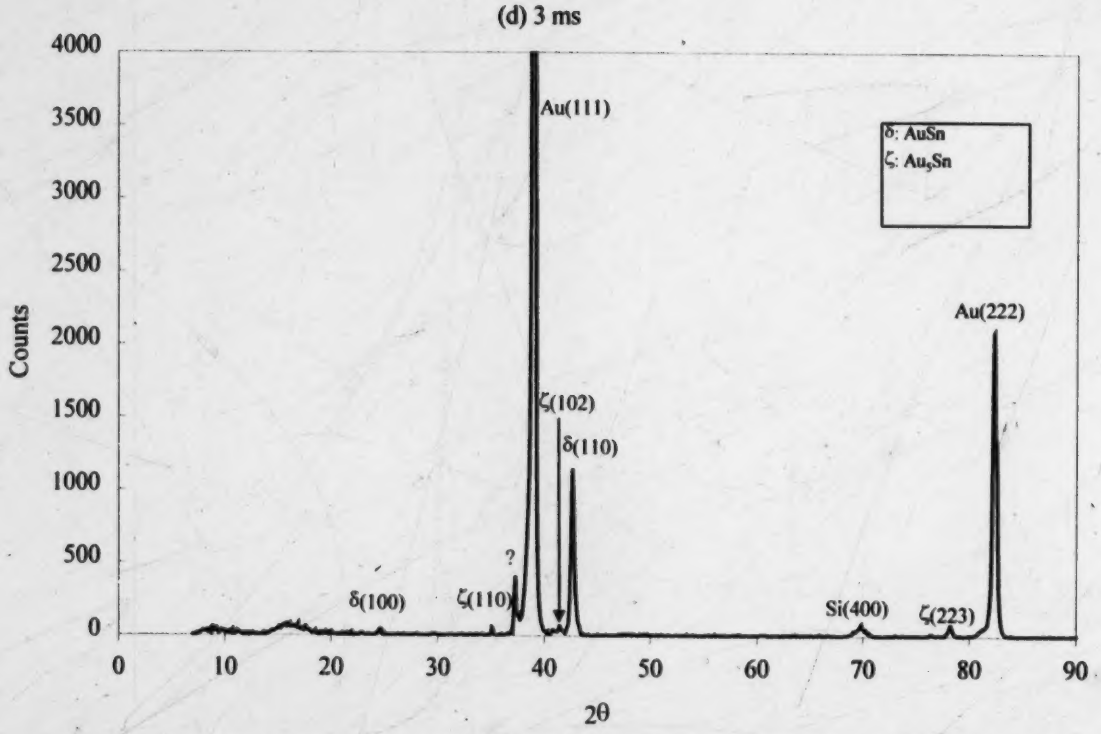

Fig. 4.15 XRD spectra for the deposits obtained at OFF times of (a) 8, (b) 6, (c) 4, and (d) 3 ms (continued).

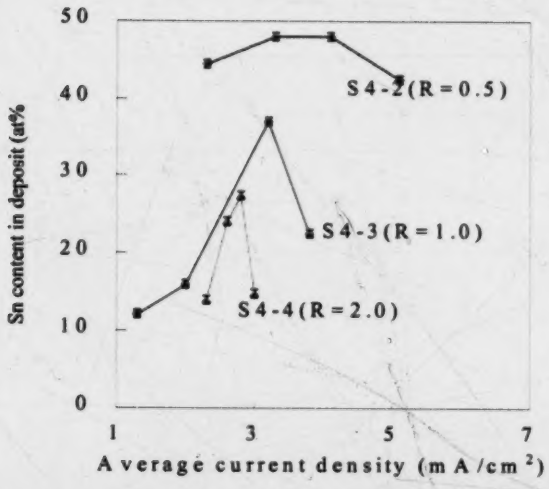

Fig. 4.16 Effect of ratio of gold to tin salt content in bath on deposit composition at 1ms of ON time and 9ms of OFF time. R is the content ratio of gold to tin salts. The error bar shows the standard deviation in the composition measurements at three different locations for each sample.

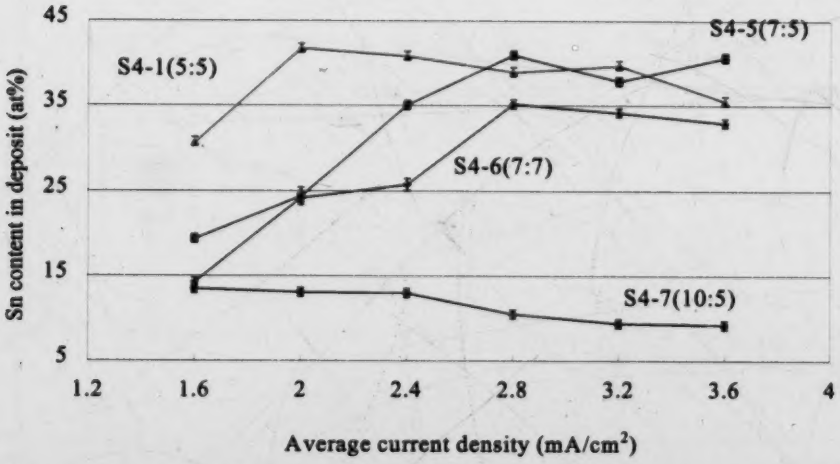

Fig. 4.17 Deposit composition curves vs. average current density for selected solutions at 2ms of ON time and 8ms of OFF time. The value in the parentheses is the content of gold and tin salts in the bath. The error bar corresponds to the standard deviation in the composition measurements at three different locations for each sample.

Chapter 5

Annealing Tests and Reproducibility Test

5.1 Introduction

In this chapter, annealing tests were performed for phase characterization purposes and reproducibility tests were conducted to assess the repeatability of the plating bath. With increasing plating time, the components in the bath are consumed, resulting in lower concentrations than their starting values. Some bath components used in the plating bath used have well developed analytical methods of determination, e.g., gold by atomic absorption spectroscopy (AAS) and gravimetry [Gemmler 94], tin by iodometric titration in the presence of an antioxidant [Schlotter 85], and sulfite by ion chromatography and differential pulse polarography [Gemmler 94]. However, it is difficult to monitor the organic components in the bath. In practice, a Hull cell is used to check the electrodeposits so that the content of the additives can be indirectly monitored. On other hand, an evaluation test for long term operation of the bath at practical deposition rates is very important for bath maintenance and accurate replenishing of components in the bath.

5.2 Experimental Methods

5.2.1 Annealing tests

Solution S4-1 was used to deposit a gold-tin alloy on a InP/InGaAs/InP wafer, which was coated with 25nm Mo/25nm Au metallization layers. The pulse plating conditions were 3 ms of ON time, 7 ms of OFF time, 2.4 mA/cm^2 of average current density and 80 min of plating time.

The as-deposited sample was annealed at 350°C for 2 min in forming gas.

Quantitative EDX analysis was done on both as deposited and annealed samples. Microstructural characterization was done primarily using SEM for the annealed sample. Cross sections of the annealed sample were also examined using transmission electron microscopy (TEM).

5.2.2 Reproducibility test

5.2.2.1 Test (I)

This reproducibility test was done with 30 mL of Solution S4-1 at an average current density of 2.8 mA/cm^2, 3 ms of ON time and 7 ms of OFF time. 18 InP wafers coated with 25nm Ti and 250nm Au were plated over approximately the same area, ~ 0.4 cm^2 for 1 hr each. The deposit composition of these wafers was determined by EDX analysis.

5.2.2.2 Test (II)

The solution utilized in this part was 50 mL of Solution S4-1. The plating was done on a InP wafer coated with 25nm Ti/250nm Au with an exposed area of 1.46cm^2. The plating conditions were 2 ms of ON time, 8 ms of OFF time, 1.6 mA/cm^2 of average current density, and 40 hrs of plating time.

The deposit composition along the thickness direction of the cross section of the sample was determined at 2.25μm intervals from the deposit-wafer interface using EDX analysis to monitor deposit composition changes with the thickness. The sample was first cold mounted, ground and finally polished with 0.05μm MgO paste. Directly cleaved cross sections were also examined in the FESEM.

5.3 Results and Discussion

5.3.1 Annealing tests

Microstructure

The composition of the as-deposited sample was Au-32.4±0.4at%Sn. SEM top view secondary electron (SE) images of an annealed sample are shown in Fig. 5.1 and backscattered electron (BSE) images of the annealed sample are shown in Fig. 5.2. The BSE images give much better phase contrast.

The composition at 3 points in the dark areas is 50.0, 47.2, 47.3at% Sn, respectively, with an average value of 48.2at% Sn. In the whiter areas, the composition is 18.3, 18.7,19.4at% Sn, respectively, with an average value of 18.8 at% Sn. It can be concluded that the dark area is AuSn and the white area is Au_5Sn. The overall composition of the deposit is hypereutectic, which is apparent from the microstructure. Representative EDX spectra for the eutectic areas, white areas and dark areas are shown in Fig. 5.3.

Phase analysis

XRD spectra of the as-deposited, annealed sample and InP wafer that hasn't been plated with deposit are shown in Fig. 5.4. Both the as-deposited and annealed sample consist of two phases. AuSn exhibits a (110) preferred orientation parallel to the surface. Both spectra contain several peaks, which come from the wafer substrate. Comparing the two spectra, the relative peak intensity ratio of AuSn (110) to Au_5Sn (113) for the annealed sample is higher than the ratio for the as-deposited sample. This means a larger percentage of AuSn phase exists in the annealed sample.

A TEM cross section image of the deposit near the deposit/wafer interface after annealing is shown in Fig. 5.5. EDX spectra of corresponding grains are also included in Fig. 5.5. This further confirms that the phase structure of the annealed sample in Fig. 5.5 consists of AuSn and Au_5Sn.

5.3.2 Reproducibility test

5.3.2.1 Test (I)

Since a relatively low gold content is used in the bath, the number of wafer pieces the bath can plate is important from a practical view. Fig. 5.6 shows how the deposit composition changes with the plating area. The figure indicates that the samples between #1 and #9 have approximately the same composition, ~39±3at% Sn, while starting with sample #10, the deposit composition significantly decreases from 34 to 18 at% Sn. Sample #9 corresponds to a total plated area 3.4 cm^2. Pulse plating conditions were utilized, with 3 ms of ON time and 7 ms of OFF time. For a current density of 2.8 mA/cm^2 for 1 hr, the typical thickness for the deposit is 3.5 μm.

The curve in Fig. 5.6 is not a very smooth curve. The reason for this may be that the actual plating condition is not exactly the same for every sample, because of the measurement errors in plating area and peak current.

It is found that after the first nine wafers have been plated, the Sn content in the deposit begins to drop. Two questions come to mind. Why does the composition change with plating time? Why does the tin content in the deposits drop instead of increase with plating time? One reason could be a change in the gold and tin content as a result of consumption of these metal ions. Chemical analysis was done to try to monitor the change of the gold ion/tin ion content ratio in the bath after plating a wafer. The gold content and tin content in the bath were checked by atomic absorption spectroscopy (AAS). The results show that the gold content decreases with plating time, while an opposite tendency was found for tin content. The tendency for tin content is not reasonable, since an insoluble anode was used for plating. This means AAS analysis is not suitable for tin content analysis.

The percentage of gold in the bath consumed after plating the first nine samples can be approximately calculated by assuming the density of the deposit is equal to the theoretical value of an equilibrium gold-tin alloy consisting of Au_5Sn and AuSn phases. The total volume of the deposit V is the product of the total plated area of the first nine samples, 3.7cm^2, and the average thickness of the deposits, which is assumed to be

3.5μm. Since the average composition of the first nine samples is Au-39at%Sn (or Au-28wt%Sn), the volume percentage of Au_5Sn and AuSn in the deposits is calculated to be ~14% and ~86%, respectively. Then the density ρ_d of the deposits can be calculated based on the atomic percentage and the density values of these two phases, it is ~13.2 g/cm^3. If g_{Au} is the total weight of the gold added in the bath before plating, the percentage of gold consumed after plating the first nine samples is $(V \times \rho_d \times wt\%Au_{deposit})/g_{Au}$, The result is ~20wt% while the percentage of the tin consumed after the first nine samples is only about 8wt%. From this calculation, it is noted that the gold content has significantly changed because of plating while the percentage of tin consumed by plating is relatively low.

From the literature, the explanation for the decreasing tin content with plating time is that tin is consumed faster than gold because of the formation of Sn-rich agglomerates [Holbrom 98]. This explanation is reasonable only for the situation where a large current density close to the limiting current density is used. For the case studied here, the selected current density is only 1.6 mA/cm^2, which is significantly less than the limiting current density, ~ $4mA/cm^2$. The change in deposit composition with plating time may be related to the content change of the supporting chemicals, e.g. ammonium citrate and sulfite.

Since a total plated area of 3.7 cm^2 with constant composition and a thickness of 3.5μm can be obtained from a bath of 30mL Solution S4-1, if the bath is scaled up to 2 L of the same solution, about 12 2-inch blank wafers can be plated with deposits of constant composition, Au-39at%Sn and thickness of 3.5μm.

5.3.2.2 Test (II)

For the second reproducibility test, Au-Sn was continually plated in a single solution to a thickness of ~26μm. Deposit composition was checked in the SEM by EDX analysis.

Surface composition analysis of the resultant deposit at 5 points yielded the following compositions: 10.4at% Sn, 11.1at% Sn, 11.4at% Sn, 10.6at%Sn, and 10.7at% Sn (average composition of Au-10.8at% Sn). Thickness as measured by FESEM on cross sections were 27.5, 26.6, 25.8, 25.2, and 24.7 μm (average thickness of 26.0 μm). SEM top views of the deposit are shown in Fig. 5.7. The surface morphology is fairly coarse.

Image at higher magnification show that the large features consist of numerous microcrystals. Gold rich deposits generally exhibits very smooth and fine microstructures. The rough features of this deposit is due to the thickness of the deposit and the long plating time.

Polished and cleaved cross section images examined in the FESEM are shown in Fig. 5.8. It is clear from the cleaved images that grain grow during the plating is in a columnar manner. Near the deposit/wafer interface, the grains are very fine and gradually become coarser with increasing deposit thickness. The fracture mode of the deposit near the interface is brittle in nature, while the fracture mode becomes more ductile with increasing thickness. Delamination of the deposit from the wafer occurred along the interface. This may take place when the sample is cleaved. A closer examination by FESEM indicates that delamination occurs between the adhesion layer, Ti layer, and the semiconductor wafer, InP. The adhesion between the deposit and the gold layer of the metallization is superior because of the rapid interdiffusion between the electrodeposit and the gold layer. Gold from the metallization is incorporated in the deposit.

BSE images of polished cross sections of the deposit are shown in Fig. 5.9. The phase contrast shown in the BSE images is much more prominent than that in the SE images (Fig. 5.8(a)). EDX analysis of the white areas in these BSE images yield Sn concentrations from 15at% to 24at%, while the composition for the dark areas ranges from 30at% to 45at% in Sn content. The actual composition value at a certain spot depends on how big the size of the interaction volume of the electron beam used with the sample and how the phases, which are presumably Au_5Sn (white areas) and AuSn (dark areas), are distributed in the deposit laterally and in the depth direction. The BSE images show two-layer structure of the deposit. The inner layer near the interface is ~ 23μm thick and a mixed layer of white and dark areas. The outer layer is ~ 2μm thick and consists only of white contrast areas. Therefore, it can be estimated that in the range of thickness less than ~ 23μm the composition should be fairly constant in the range of 30at% - 45at% in Sn content and in the outer layer the composition changes towards a gold rich direction. In addition to the phase distribution, the columnar manner of grain growth in the deposit is clearly evident.

Composition depth profiles at 4 locations (Fig. 5.10) of the deposit were done along the thickness direction. In Fig. 5.10, a very high contrast was used in order to give a clear view of the locations where the depth profiles were measured, resulting in poor-quality pictures. The results are tabulated in Table 5.1 and plotted in Fig. 5.11. The reason why a 2.25μm interval was chosen for the depth profile measurement is because of the consideration on the size of the interaction volume of the electron beam used in EDX analysis with the deposit. Monte Carlo simulations were performed using the software, MoCarBulk, for pure gold, pure tin and AuSn compound at the conditions of 20 keV and zero tilting. For AuSn, its atomic number was assumed as the average of the atomic numbers of gold and tin, while its atomic weight was also assumed as the average value of the atomic weights of gold and tin. The results of Monte Carlo simulations are listed in Table 5.2. Since the lateral and depth range of the interaction volume is related to the average atomic number, the higher tin content in the deposit will result in a larger lateral and depth range of the interaction volume. The composition determination of the deposits in Fig. 5.11 shows that the deposit obtained in this reproducibility test has lower Sn content than for AuSn, therefore, the lateral and depth size of the interaction volume of the electron beam used with the deposit must be less than the ranges with AuSn. This means the lateral size of the interaction volume for the deposit is less than 1.7μm.

From the curves in Fig. 5.11, it can be seen the depth profiles for Series 1, 2 and 3 are quite similar, while Series 4 is significantly different. Tin content, for Series 1, 2 and 3, initially increases with increasing thickness, forms a plateau from ~2 to 22 μm, and then drops to less than 15at%Sn at thicknesses greater than 22μm. For Series 4, the tin content drops to 20at% at a thickness of ~ 9 μm. Observation of the BSE images of the cross sections for regions corresponding to Series 1, 2, and 3 shows a two-layered deposit structure along thickness. Therefore the curve shape with a composition plateau for Series 1, 2 and 3 should be representative. For Series 4 the composition profile passes through a large Au_5Sn columnar grain, which is shown as a white strip starting at ~ 9 μm from the interface and growing outwards along the thickness direction. Therefore, the shape of the composition curve vs. thickness actually depends on the position of the profile. One way of eliminating this problem is through digital compositional mapping of the cross section of the deposit over an area instead of a line profile. In this way, the

lateral average composition at a specific distance from the interface can be obtained by simply averaging all the composition values obtained.

It is meaningful to make an estimation from this test on how many 2-inch wafers could be plated without significant composition change. The result in this part shows that with 50mL of Solution S4-1, a 1.46cm^2 wafer can be plated with a 23μm thick deposit with approximately constant composition. Assuming the solution in the bath is scaled up to 2L and 2-inch blank wafers are to be plated with constant composition and solder thickness of 3.5 μm, 19 such wafers can be plated with the gold-tin alloy. This number is greater than 12 wafers, which was obtained in Reproducibility Test (I). This is because a larger volume of solution was used in Test (II) than in Test (I).

The result of the reproducibility test gives a guide to when the bath should be replenished. The reproducibility property of the bath depends on the bath stability and bath chemistry.

5.4 Conclusions

In this chapter, annealing tests at 350°C were performed for a deposit with a composition of Au-32.4at%Sn for phase analysis purposes and two reproducibility tests were conducted to assess the repeatability of the plating bath.

The annealed deposit has a typical hyper-eutectic microstructure which consists of some dark areas of AuSn and Au_5Sn/AuSn eutectic. Pores appear in the annealed deposit. XRD spectra of the as-deposited and annealed deposits are very similar except that the peak intensity of AuSn (110) is increased in the annealed deposit.

In Reproducibility Test (I), with 30 mL of Solution S4-1, nine wafers with average area of ~ 0.4cm^2 were plated with gold-tin deposits with approximately constant composition of about Au-39at%Sn and a thickness of 3.5 μm. If the solution is scaled up to 2L, 12 pieces of 2-inch blank wafers could be plated with constant composition of about Au-39at%Sn and a thickness of 3.5 μm.

In Reproducibility Test (II), with 50 mL of Solution S4-1, a 1.46cm^2 wafer was plated with a 23 μm thick gold-tin deposit with approximately constant composition of about Au-38at%Sn. When the thickness of the deposit was greater than 23 μm, the tin content in the deposit decreased rapidly with increasing thickness. If the solution is scaled up to 2L, 19 pieces of 2-inch blank wafers could be plated with constant composition of about Au-38at%Sn and a thickness of 3.5 μm.

Table 5.1 Compositional depth profile results for 4 different locations in reproducibility test (II).

Points	P1	P2	P3	P4	P5	P6	P7	P8	P9	P10	P11	P12	P13
D* (μm)	0.5	2.8	5.0	7.3	9.5	11.8	14.0	16.3	18.5	20.8	23.0	25.3	27.5
Series1	37.4	42.2	40.0	38.0	41.8	43.2	40.0	38.6	40.9	41.6	38.9	23.9	12.5
Series2	40.1	40.7	33.2	35.7	33.6	41.7	43.2	42.2	42.5	41.0	14.1	12.9	
Series3	27.8	36.9	41.9	43.0	44.0	44.5	41.8	31.1	34.7	39.5	43.8	31.8	13.4
Series4	36.4	42.9	33.9	32.7	21.4	21.1	24.0	15.2	13.9	14.0	15.4	14.0	13.7

D* is the distance from the point checked to the deposit-wafer interface.

Table 5.2 Results for Monte Carlo simulations*.

	Atomic number	Atomic weight	Density (g/cm^3)	Lateral size of the interaction volume (μm)	Depth size of the interaction volume (μm)
Au	79	196.97	19.30	1.0	0.6
AuSn	64	157.83	11.74	1.7	1.0
Sn	50	118.69	5.77	2.8	1.8

* The conditions used for the simulations are 20 keV and zero tilting.

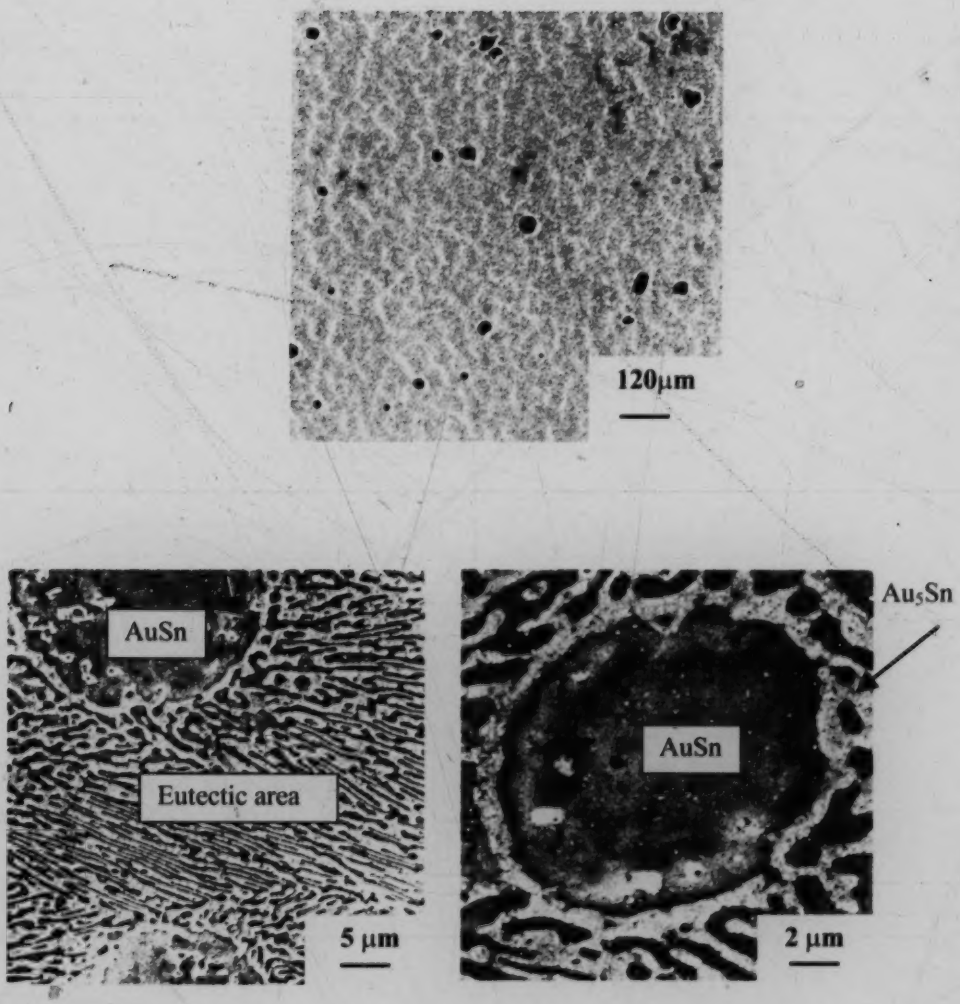

Fig. 5.1 SE images of a deposit of Au-32.4at% Sn annealed at 350°C for 2 min.

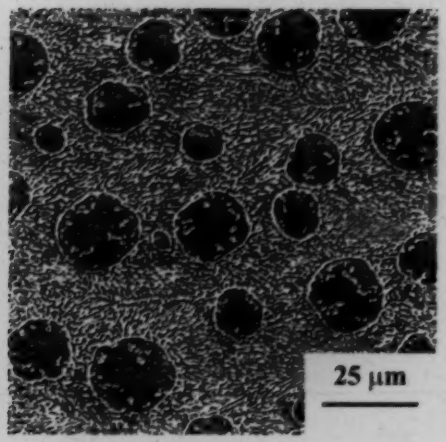

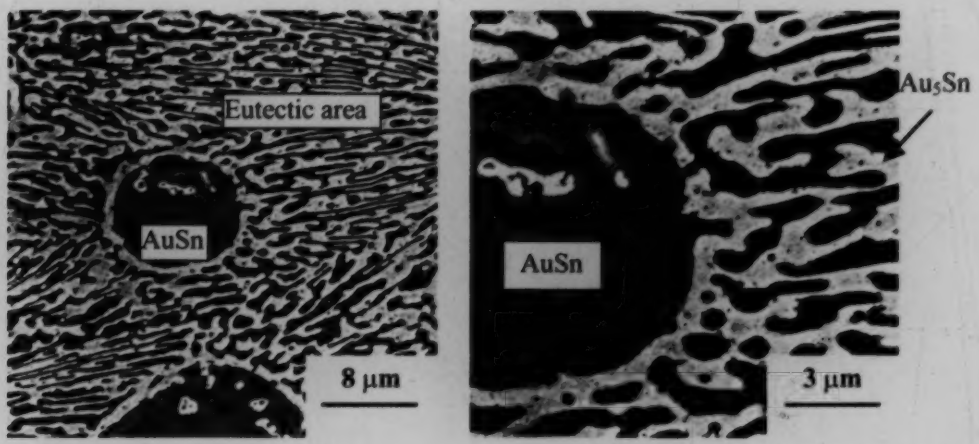

Fig. 5.2 BSE images of the annealed sample at 350°C for 2 min.

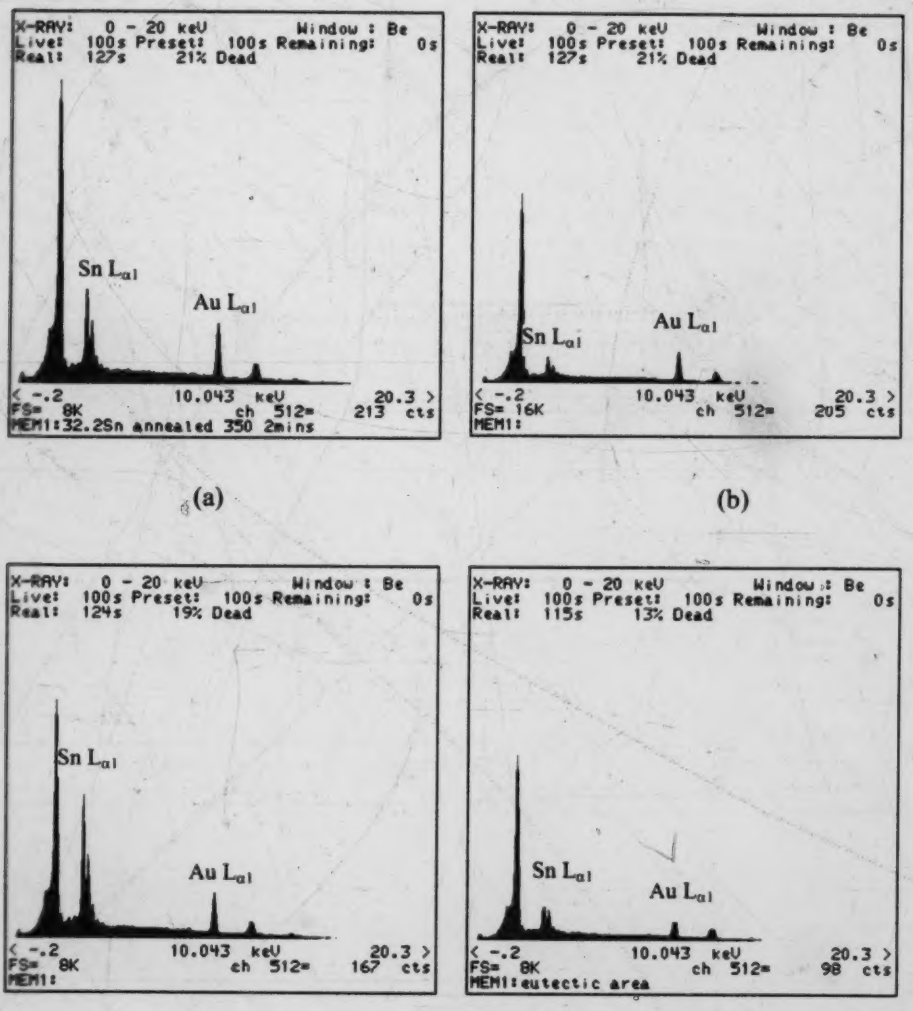

Fig. 5.3 Representative EDX spectra for (a) overall sample, (b) light contrast areas, (c) dark contrast areas and (d) eutectic areas of a sample annealed at 350°C for 2 min.

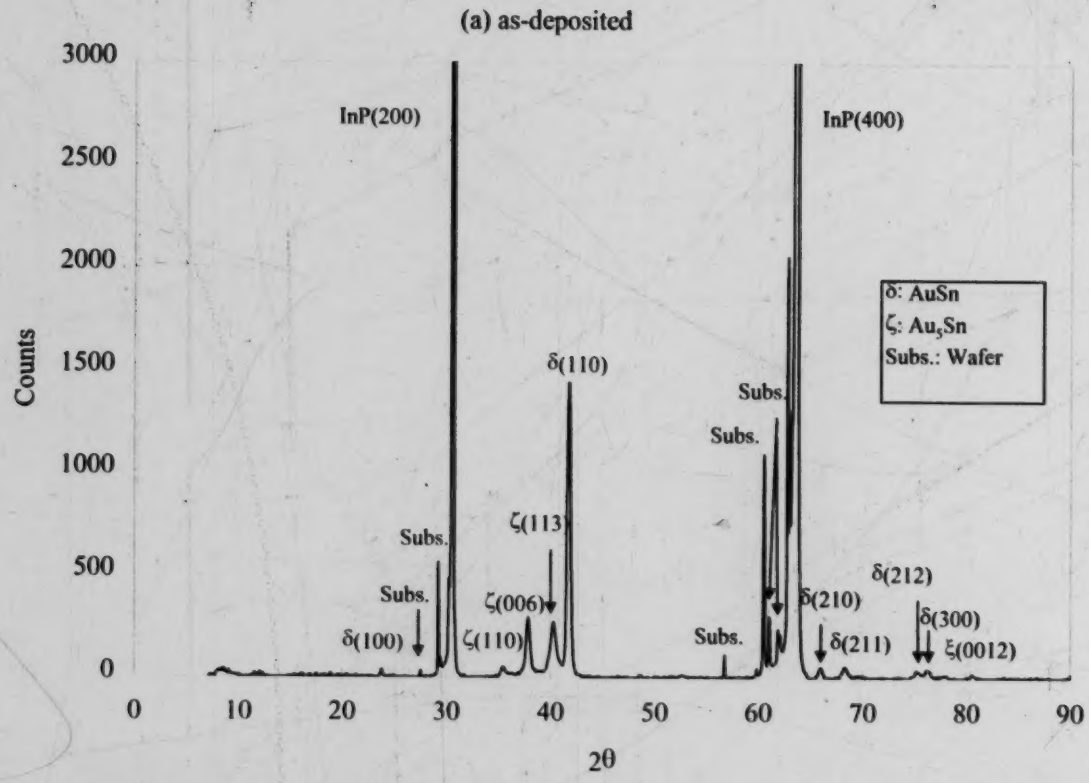

Fig. 5.4 XRD spectra of (a) as-deposited sample, (b) sample annealed at 350°C for 2 min, and (c) InP wafer with 25nm Mo/25nm Au metallization (to be continued).

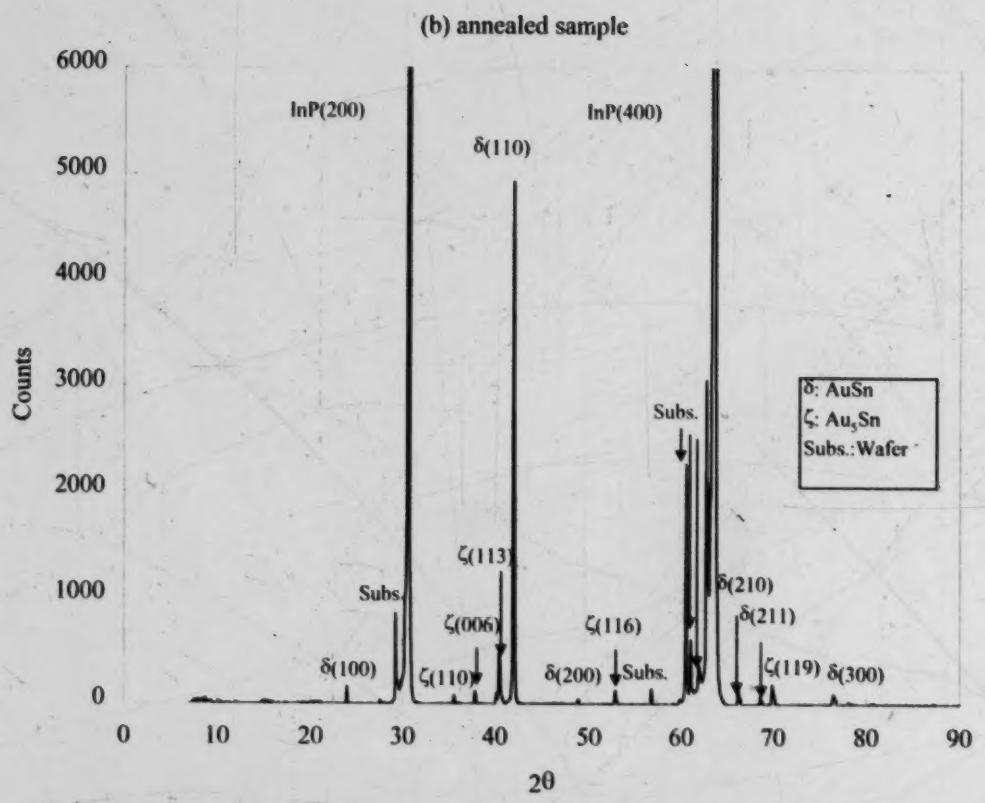

Fig. 5.4 XRD spectra of (a) as-deposited sample, (b) sample annealed at 350°C for 2 min, and (c) InP wafer with 25nm Mo/25nm Au metallization (to be continued).

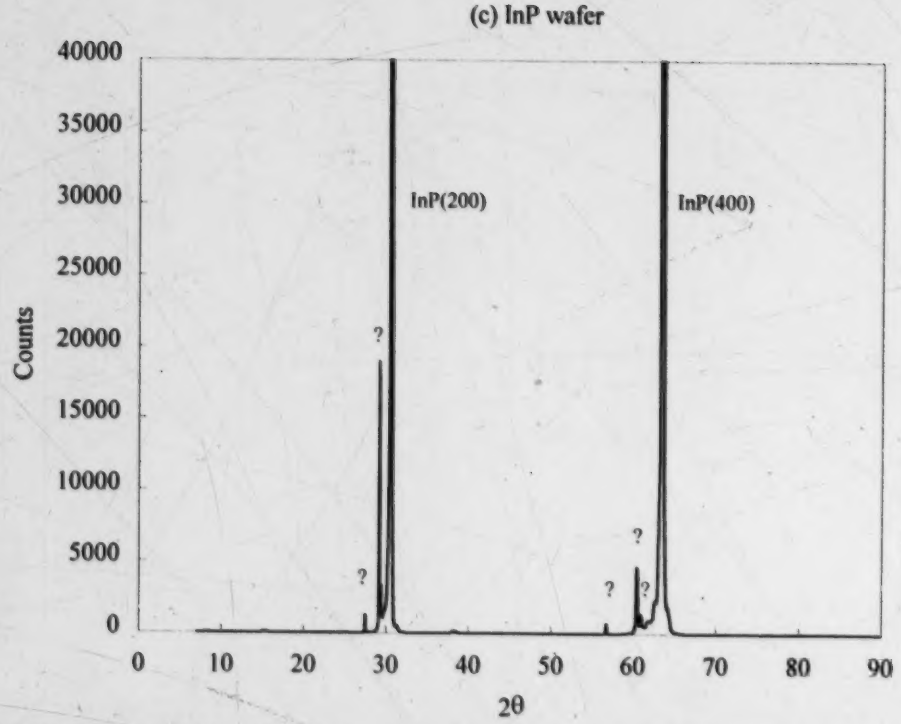

Fig. 5.4 XRD spectra of (a) as-deposited sample, (b) sample annealed at 350°C for 2 min, and (c) InP wafer with 25nm Mo/25nm Au metallization.

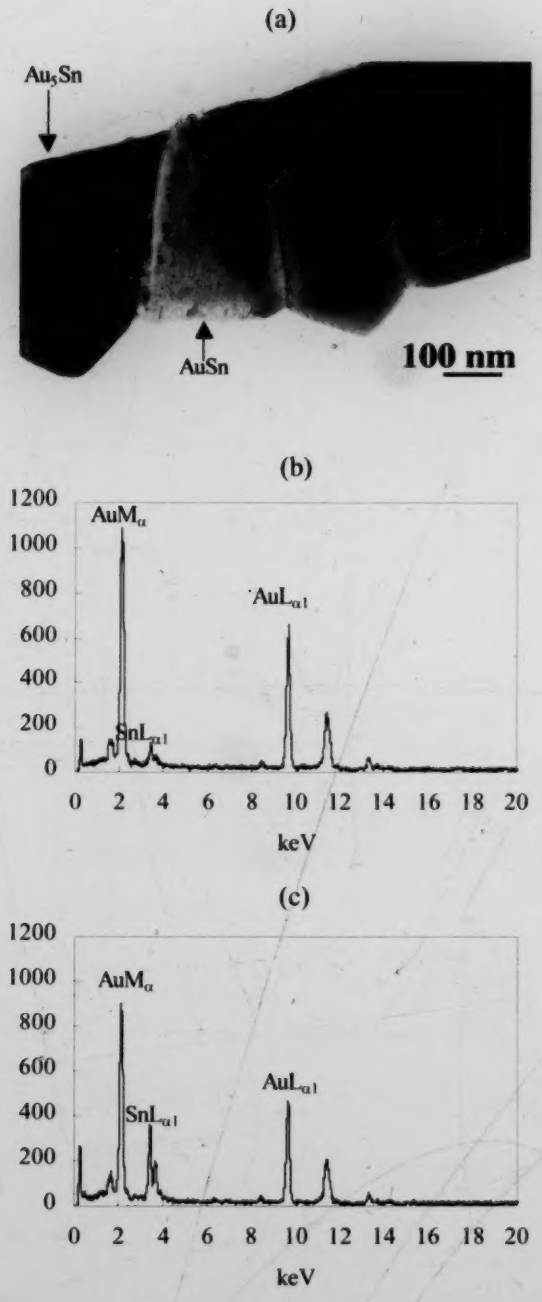

Fig. 5.5 TEM cross section image (a) of the annealed deposit at 350°C for 2 min and EDX spectra for the Au_5Sn (b) and AuSn phases (c).

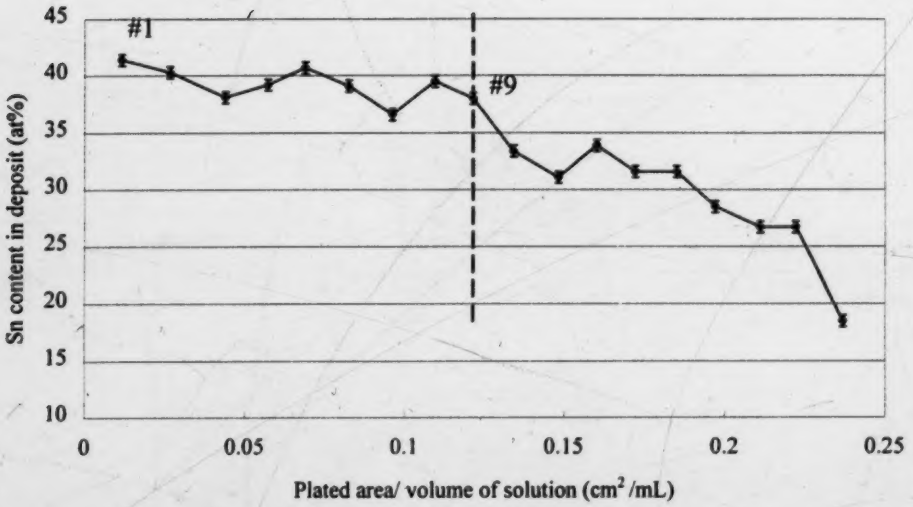

Fig. 5.6 Deposit composition vs. plated area for the sample in Reproducibility Test (I). The error bar corresponds to the standard deviation for the composition measurements at three different locations of each sample.

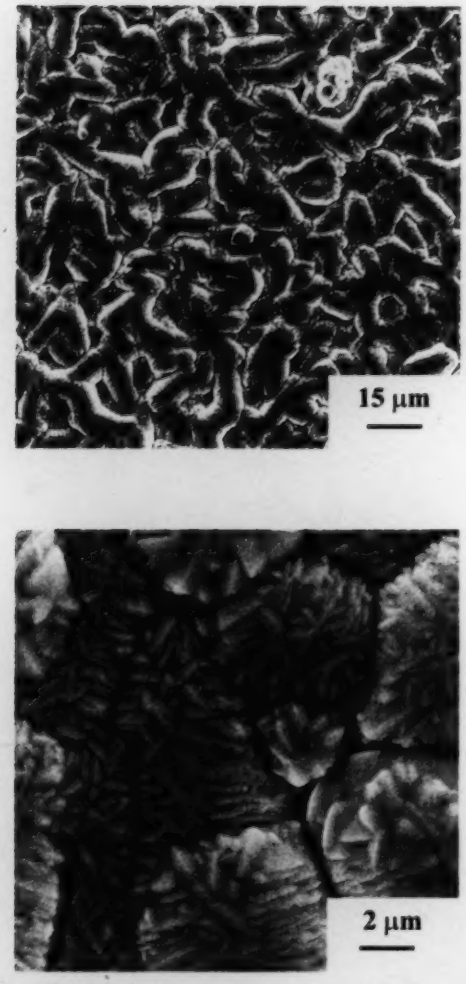

Fig. 5.7 SEM top views of the deposit in Reproducibility Test (II).

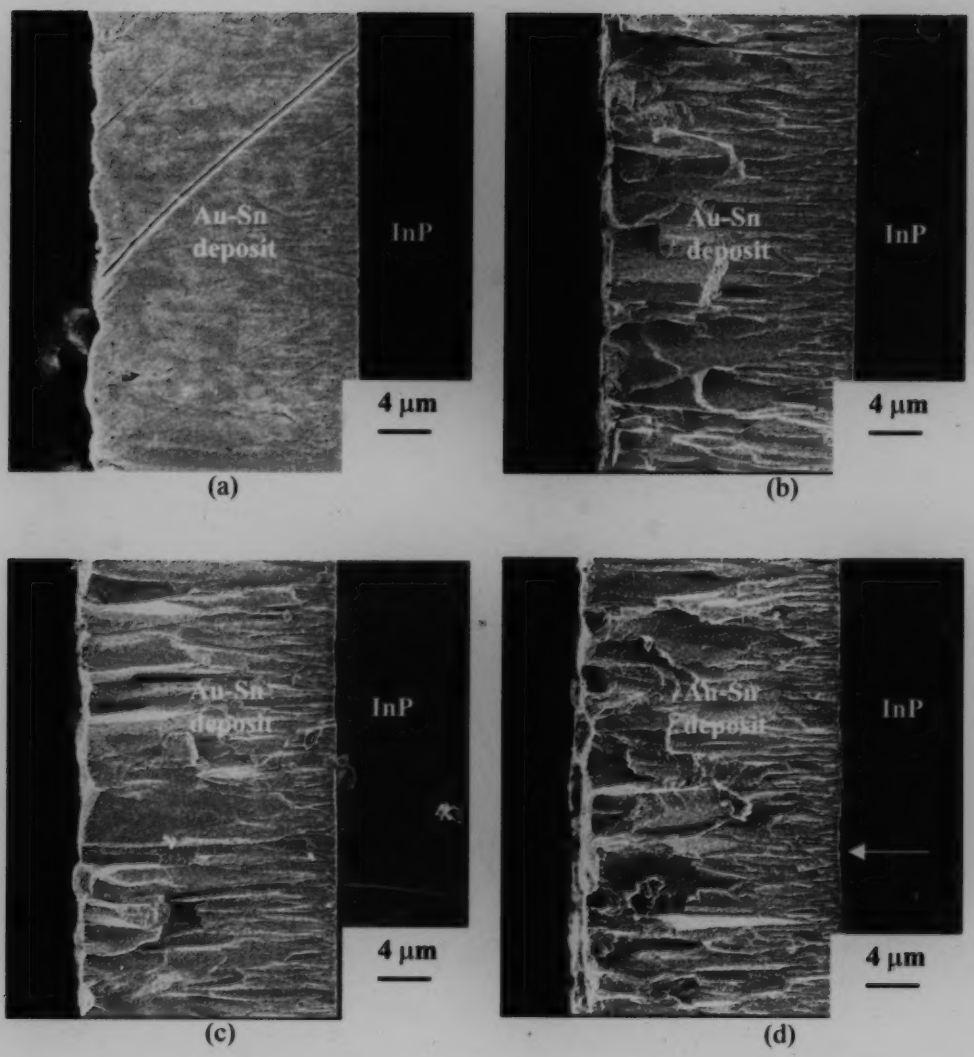

Fig. 5.8 FESEM images of (a) polished and (b), (c) and (d) cleaved cross section images of the deposit in Reproducibility Test (II). The arrow in (d) shows where delamination has occurred.

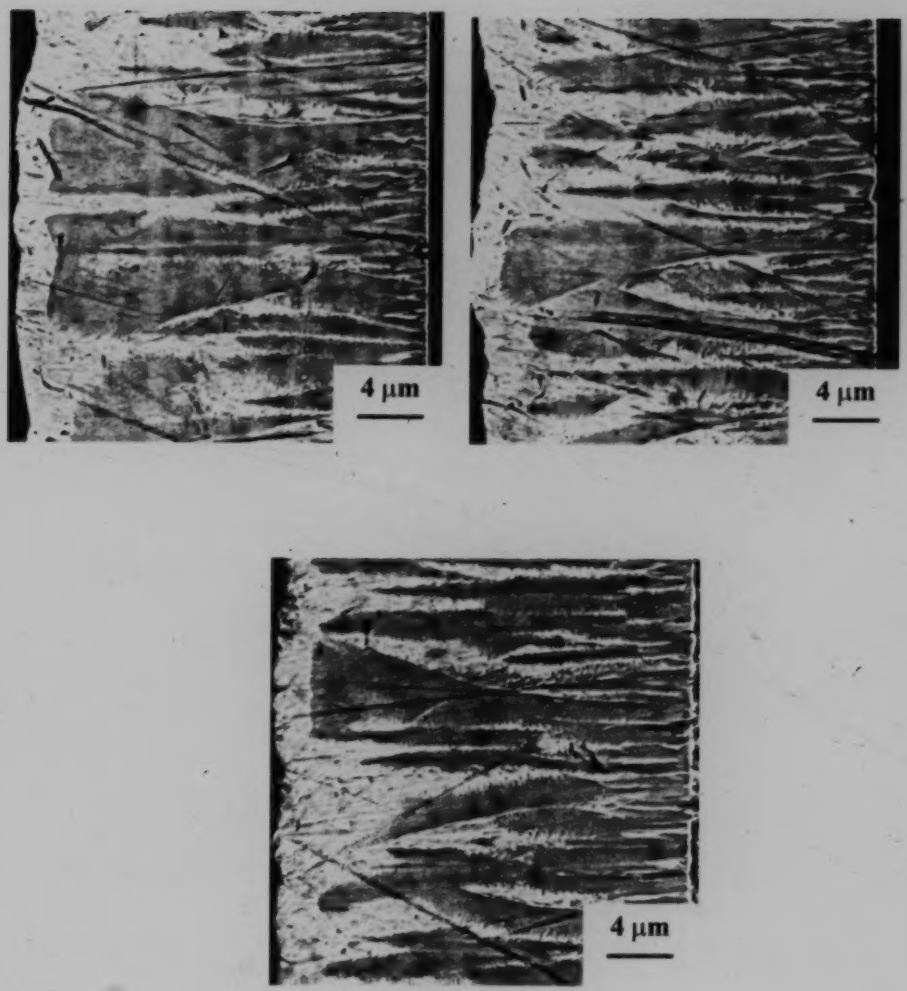

Fig. 5.9 BSE images of several selected polished cross section segments of the deposit in Reproducibility Test (II). The InP substrate is to the right of the deposit.

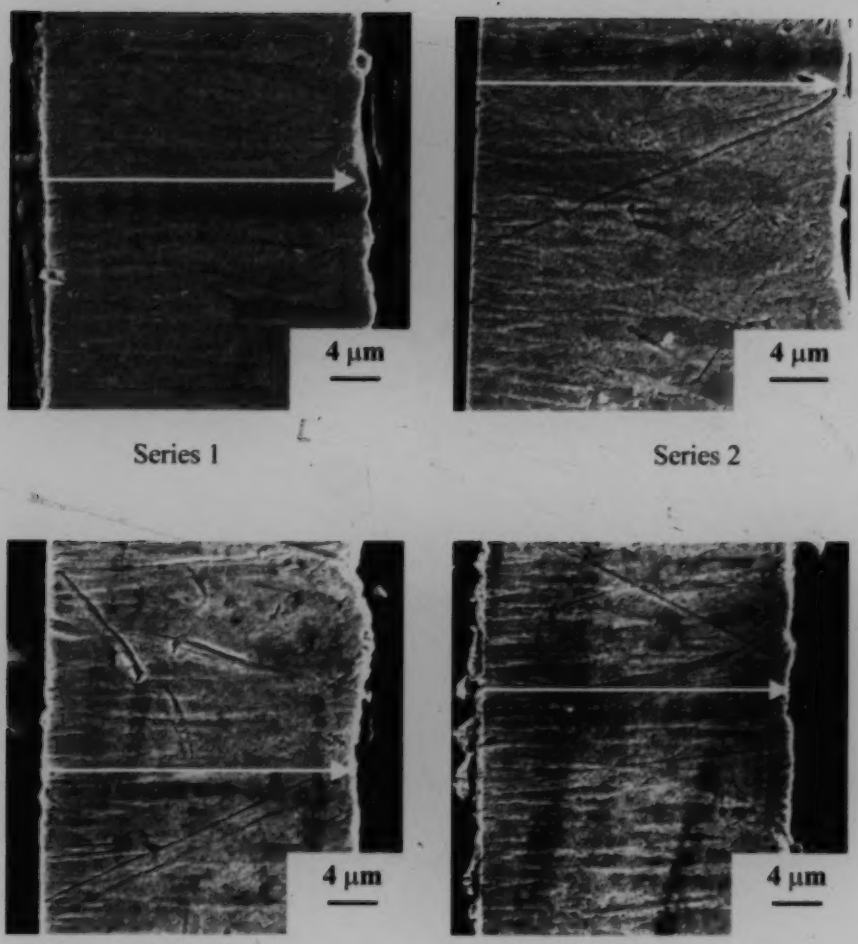

Fig. 5.10 Locations of 4 compositional depth profiles in the polished cross section of the deposit for Reproducibility Test (II). The InP substrate is to the left of the deposit.

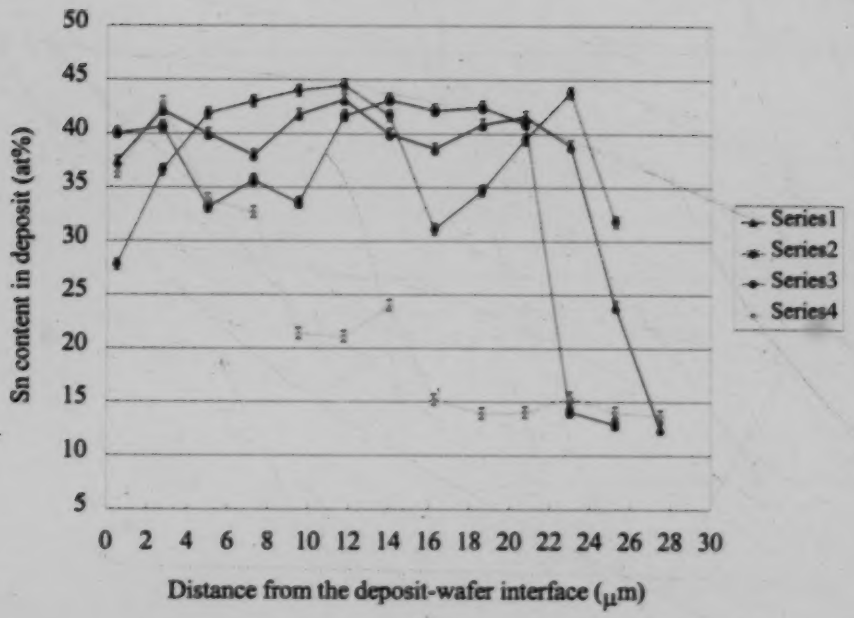

Fig. 5.11 Composition vs. distance from the deposit-wafer interface for the sample regions shown in Fig. 5.10. The error bar is statistical error of Sn content in EDS analysis.

Chapter 6

Conclusions and Recommendations

6.1 Conclusions

A relatively stable gold-tin plating system has been developed. This is a non-cyanide weak-acid system with ammonium citrate as a buffering agent for hydrogen ions and tin ions, chloride-ammonium citrate-sodium sulfite as a mixed complexing agent for gold, and L-ascorbic acid as an inhibitor of tin hydrolysis. The bath stability depends on the total content of gold salt and tin salt, additives such as sodium sulfite, peptone and ethylene diamine, and the way the solution is prepared and stored.

The study on the polarization behavior of a gold coated wafer cathode in Sn solutions, gold solutions and gold-tin solutions shows that addition of ammonium citrate in Sn solutions suppresses tin plating, while addition of sodium sulfite enhances tin plating. The shape of the curves for Sn solutions with sulfite undergoes a substantial change from one-wave curves to two-wave curves. Sodium sulfite suppresses gold plating substantially. The curve for a gold-tin solution and the summed curve for the corresponding gold solution and tin solution are very similar in shape. Therefore, it is inferred that the gold and tin plating processes are independent processes in gold-tin alloy plating.

The causticity test shows that the InP and GaAs wafer is not subject to significant corrosion in Solution S6 studied since no weight loss and no corrosion pits were detected for InP and GaAs wafers after soaking in Solution S6 for 48 hrs.

DC plating and PC plating of gold-tin alloys in the developed chloride-sulfite solutions were carried out and compared. PC deposits have consistently higher Sn content than DC deposits. At relatively low average current densities, i.e. less than 2.4 mA/cm^2, the grain sizes of the PC deposits are similar to that of the DC deposits, while at higher average current densities, i.e., greater than 2.4 mA/cm^2, PC deposits have a much finer structure and smoother surface.

When the average current density and cycle period are held constant, the deposit composition vs. ON time curve has a plateau. The deposit obtained at 2 ms of ON time has the finest structure and smoothest surface. When the peak current density and OFF time are held constant, the deposit composition curve vs. ON time also has a plateau. The microstructure of the deposit depends on the deposit composition. When the deposit is gold-rich compared with the eutectic composition, the deposits are bright and shiny and have a very fine grain structure. When the deposit compositions are similar, e.g., for the deposits obtained at 2 ms to 4 ms ON times, the grain structures are finer for shorter ON times. The deposit at long ON times, e.g., 4ms, has a microstructure characteristic of DC deposits. XRD phase analysis shows that the electrodeposits are consistently crystalline. The phase structure is close to the equilibrium phase structure of the gold-tin binary system. Au_5Sn and AuSn are present in the deposits and these phases exhibit preferred orientation which changes with the ON time.

When the peak current density and ON time are held constant, the Sn content in the deposits first increases with increasing OFF time and then reaches a plateau. At very short OFF times, e.g., 3 - 4 ms, the grains are very coarse. No microstructural difference between the deposits obtained at OFF times of 6 to 9.9ms is found in the deposits.

The study of effect of selected electrolyte parameters shows higher Sn content in the bath results in a higher tin content in the deposits, and higher total content of gold and tin salts in the bath results in a lower tin content in the deposits.

Annealing tests at 350°C were performed for a deposit with a composition of Au-32.4at%Sn for phase analysis purposes and two reproducibility tests were conducted to assess the repeatability of the plating bath.

Annealing tests were performed for a Au-32.3at%Sn deposit. The annealed deposit has a typical hyper-eutectic microstructure. XRD spectra of the as-deposited deposit and annealed deposit are very similar except that the peak intensity of AuSn (110) is increased in the annealed deposit.

Two reproducibility tests were done and it is estimated that if the bath is scaled up to 2L, more than 10 pieces of 2-inch blank wafers could be plated with constant composition of about Au-39at%Sn and a thickness of 3.5 μm.

6.2 Recommendations

The additives such as peptone and ethylene diamine have proven to be able to improve the bath stability. The study on the effect of these additives on polarization behavior of gold-tin bath and on deposit composition and microstructure needs to be completed.

It is inferred in the thesis that Sn ions in the bath are complexed by NH_3 dissolved in the bath from ammonium citrate. However, no information has been found from the literature about Sn-NH_3 complex. This needs to be confirmed by chemical analysis.

For PC plating of Au-Sn alloy, a proper combination of plating parameters and gold- and tin- content ratio in the bath leads to deposits with the desired composition, fine structure and low impurity content. A wider range of PC plating parameters including peak current density, average current density, ON time, OFF time and duty cycle and PRC, combined with a wider range of gold- and tin- content ratios, should be tried for this purpose. Different electrolyte conditions that can be tried include temperature, pH, agitation condition, and additives. Cathodic potential response to a transient current step on the order of millisecond needs to be measured to determine the cathodic potential, which can be combined with the polarization behavior of the bath to explain the relationship between deposit composition and current density used.

In reproducibility tests, chemical analysis of gold and tin contents in the bath should be combined with deposit compositional analysis to give a more convincing explanation of the tendency of deposit composition vs. plating time or the total plated area. AAS or gravimetry can be used for gold-content analysis, while tin content can be determined by iodometric titration. The chemical analysis of sulfite content in the bath with plating time will give information on how fast the sulfite is consumed and it can be determined whether the sharp change in deposit composition relates to the change in sulfite content.

From a practical point of view, electroplating of Au-Sn solder needs to be carried out on a patterned wafer surface other than a blank wafer. The lifetime of the bath needs to be examined during practical operations.

REFERENCES

[Andricacos 98] P. C. Andricacos, *The Electrochemical Society Interface*, (Spring 1998) 23.

[Brenner 63] A. Brenner, *Electrodeposition of Alloys*, Academic Press, New York (1963) p.2-28.

[Buene 80-1] L. Buene, H. Falkenberg-arell, and J. Tafto, *Thin Solid Films* **65,** (1980) 247.

[Buene 80-2] L. Buene, H. Falkenberg-arell, J. Gjonnes and J. Tafto, *Thin Solid Films* **67,** (1980) 95.

[Catonne 84] J. C. Catonne, J. D. Jehanno and J. Royon, *Proceedings - Interfinish 84, 11th World Congress on Metal Finishing*, Jerusalem, Isr., (1984) p.191.

[Chang 81] W. Chang and K. Li, 'Concise handbook of analytical chemistry', Beijing University Publishing House, 1981, p.121.

[Chassaing 89] E. Chassaing, K. Vu Quang and R. Wiart, *J. Appl. Electrochem.* **19,** (1989) 839.

[Cheh 71] H. Y. Cheh, *J. Electrochem. Soc.* **118,** (1971) 1132.

[Cheh 86] H. Y. Cheh, Chap.2 in *Theory and Practice of Pulse Plating*, ed. J. Puipe and F. Leaman, American Electroplates and Surface Finishers Society, (1986) p.13.

[Chen 88] S. Chen, K. Yin, and R. E. White, *J. Electrochem. Soc.: Sci. & Technol.* **135,** (1988) 2193.

[Cheng 83] T. Cheng and H. Y. Cheh, *Meeting of the Electrochemical Society*, Washington, DC, Abstract 248, (Oct. 1983)

[Christie 94] I. R. Christie and B. P. Cameron, *Gold Bull.* **27,** (1994) 12.

[Deshmukh 92] R. D. Deshmukh, M. F. Brady, R. A. Roll, L. A. King, J. Shmulovich and D. R. Zolnowski, *IEPS*, Austin, (1992)

[Dohle 96] G. R. Dohle, J. J. Callahan, K. P. Martin and T. J. Drabik, *IEEE Trans. Comp. Packaging, and Manuf. Tehnol., Part B*, **19,** (1996) 57.

[Dossenbach 86] O. Dossenbach, Chap.6 in *Theory and Practice of Pulse Plating*, ed. J. Puipe and F. Leaman, American Electroplates and Surface Finishers Society, (1986) p.73.

[Duffek 73] E. F. Duffek, in "*Plating in the Electronics Industry*" *4th Symposium*, Indianapolis, (1973) p.194.

[Duva 70] R. Duva and P. J. Raleigh, *U.S. Pat.* 3,520,875(1970).

[Elsner 1845] J. Elsner, *Prakt. Chem.*, **35**, (1845) 361.

[Frey 95] T. Frey and W. Hempel, *DE* 4406434, (1995).

[Gemmler 94] A. Gemmler, W. Keller, H. Richter and K. Ruess, *Plating and Surface Finishing*, (August 1994) p.52.

[Gileadi 93] E. Gileadi, Chapter 1~15, in *'Electrode Kinetics for Chemists, chemical Engingeers, and Materials Scientists'*, VCH Publishers, Inc., (1993) p.1.

[Gorbunova 69] K. M. Gorbunova and Yu. M. Polukarov, Chapter 2, in '*Electrodeposition of Metals and Alloys*', ed. N. E. Khomutov, IPST Press Binding: Wiener Bindery Ltd., Jerusalem, (1969) p.28.

[Gregersen 81] D. Gregersen, L. Buene, T. Finstad, O. Lonsjo, and T. Olsen, *Thin Solid Films* **78**, (1981) 95.

[Holmbom 98] G. Holmbom, J. A. Abys, H. K. Straschil and M. Svensson, *Plating & Surface Finishing* **85**, (1998) 66.

[Honma 95] H. Honma and K. Hagiwara, *J. Electrochem. Soc.* **144**, (1995) 3469.

[Hugsted 82] B. Hugsted, L. Buene, T. Finstad, O. Lonsjo and T. Olsen, *Thin Solid Films* **98**, (1982) 81.

[Hunziker 96] W. Hunziker, W. Voyt and H. Melchior, *Proceeding of 1996 IEEE 46th Electronic Components and Technology Conference*, Orlando, Florida, (May 1996) p.8.

[Ibl 80] N. Ibl, *Surface Technology*, **10**, (1980) 81.

[Ivey 97] D. G. Ivey, Microstructural Characterization of Au/Sn Solder for Packaging in Optoelectronic Applications, *Micron*, (accepted in Sept. 1997).

[Johnson 91] P. O. Johnson and M. Wolverton, *Intl. J. Hybrid Microelectron.* **14**, (1991) 96.

[Jones 82] H. Jones, *Inst. Metallurgists Monograph,* No. 8, London, (1982).

[Kallmayer 95-1] C. Kallmayer, D. Lin, J. Kloeser, H. Oppermann, E. Zakel and H. Reichl, *1995 IEEE/CPMT Int'l Electronics Manufacturing Technology Symposium,* (1995) p.20.

[Kallmayer 95-2] C. Kallmayer, D. Lin, H. Oppermann, J. Kloeser, S. Werb, E. Zakel and H. Reichl, *10th European Microelectronics Conference,* (1995) p.440.

[Kallymayer 95-3] C. Kallymayer, H. Oppermann, J. Kloeser, E. Zakel and H. Reichl, Proc. ITAP, (1995).

[Kato 95] M. Kato, Y. Yazawa, and Y. Okinaka, *International Technical Conference Proceedings,* American Electroplaters and surface Finishers Society, (1995) p.813.

[Katz 94-1] A. Katz, C. H. Lee and K. L. Tai, *Mater. Chem. Phys.* **37**, (1994) 303.

[Katz 94-2] A. Katz, F. Baiocchi, E. Lane, C. H. Lee, C. Hall, J. Doting, C. Grijsbach and K. Harris, *J. Appl. Phys.* 75, (1994)

[Knodler 86] A. Knodler, Chap.9, in *Theory and Practice of Pulse Plating*, ed. J. Puipe and F. Leaman, American Electroplates and Surface Finishers Society, (1986) p.119.

[Koulke 74] D. G. Foulke, Chap. 7, in *Gold Plating Technology*, ed. F. H. Reid and W. Goldie, Electrchemical Publications Limited, (1974) p.52.

[Kubota 83] N. Kubota, T. Horikoshi and E. Sato, *J. Met. Fin. Soc. Japan* **34**, (1983) 37.

[Kubota 84] N. Kubota, T. Horikoshi and E. Sato, *Plating and Surface Finishing*, (March 1984) 46.

[Kuhn 95] W. Kuhn, W. Zilske and A. –G. Degussa, *Ger. DE 4,406,434*, Aug. 10 1995.

[Landolt 86] D. Landolt, Chap.5 in *Theory and Practice of Pulse Plating*, ed. J. Puipe and F. Leaman, American Electroplates and Surface

Finishers Society, (1986) p.55.

[Landolt 94] D. Landolt, *Electrochimica Acta* **39**, (1994) 1075.

[Laude 80] P. Laude, E. Marka and F. Zuntini, *U. S. Patent 4,192,723* (1980).

[Lee 91] C. C. Lee, C. Y. Wang and G. S. Matijasevic, *IEEE Trans. Components, Hybrids, and Manufacturing Technol.* **14**, (1991) 407.

[Lee 92] C. C. Lee and C. Y. Wang, *Thin Solid Films*, **208**, (1992) 202.

[Lee 94] C. H. Lee, K. L. Tai, D. D. Bacon, C. Doherty and A. Katz, *Semicond. Sci. Technol.* **9**, (1994) 379.

[Li 97] Y. G. Li and A. Lasia, *J. Electrochem. Soc.* **144**, (1997) 1979.

[Marinkovic 88] Z. Marinkovic and V. Simic, *Thin Solid Films* **156**, (1988) 105.

[Mason 74] D. R. Mason, A. Blair, and P. Wilkinson, *Trans. Inst. Met. Finish.* **52**, (1974) 143.

[Mathias 90] M. F. Mathias and T. W. Chapman, *J. Electrochem. Soc.* **137**, (1990) 102.

[Matijasevic 90] G. S. Matijasevic, C. Y. Wang and C. C. Lee, *IEEE Trans. Comp. Hybrids and Manuf. Technol.* **13**, (1990) 1128.

[Matijasevic 93] G. S. Matijasevic, C. C. Lee and C. Y. Wang, *Thin Solid Films*, **223**, (1993) 276.

[Matsumoto 86] S. Matsumoto and Y. Inomata, *JP 61 15,992 [86 15,992]*, (Jan. 24,1986).

[Meyer 69] A. Meyer, S. Losi, and F. Zuntini, *Proc. Fachtagung. Galvanotechnik*, Leipzig (1970); Swiss Pat., 506,828 (1969).

[Mil 77] 'Test Methods and Procedures for Microelectronics', *MIL-STD 883*, United States Department of Defense, Washington, DC, 1977.

[Morrissey 93] R. J. Morrissey, *Plating and Surface Finishing*, (April 1993) p.75.

[Morrissey 94] R. J. Morrissey and R. I. Cranston, *US Patent 5,277,790*, (Jan. 11, 1994).

[Nakahara 80] S. Nakahara and R. J. McCoy, *Thin Solid Films* **72**, (1980) 457.

[Nicol 76-1] M. J. Nicol and E. Schalch, *Report no. 1848*, National Institute for Metallurgy, Johannesburg, (1976).

[Nicol 76-2] M. J. Nicol and E. Schalch, *Report no. 1844*, National Institute for Metallurgy, Johannesburg, (1976).

[Nishiguchi 90] M. Nishiguchi, N. Goto and H. Mishizawa, *Proc. IEEE Int. Electronics Manufacturing Technology Symp.*, Washington, DC, Oct. 1990

[Oddo 27] B. Odde and Q. Mingoia, *Gazz. Chim. Ital.* **57** (1927), p.820.

[Osaka 97] T. Osaka, A. Kodera, T. Misato, T. Homma, Y. Okinada and O. Yoshioka, *J. Electrochem. Soc.* **144**, (1997) 3462.

[Page 74] T. R. Page, *Met. Finish. J.*, **19** (1973), 274-279, 304-308, 338-345 and **20** (1974), 4-9, 29, 33-36, 62-65, 87-90, 119, 122-125.

[Paoli 75] T. L. Paoli, *IEEE Quantum Electron*, QE-11, (1995) 498.

[Pittroff 95] W. Pittroff, T. Reiche, J. Barnikow, A. Klein, U. Merkel, K. Vogel and J. Wurfl, *Appl. Phys. Lett.* 67, (1995) 2367.

[Pletcher 90] D. Pletcher and F. C. Walsh, Chapter 1 and 8, in 'Industrial Electrochemistry', Chapman and Hall Ltd., (1990) p.1.

[Plumbridge 96] W. J. Plumbridge, *J. Mater. Sci.* **31** (1996) 2501.

[Puippe 86-1] J. C. Puippe, Chap.1 in *Theory and Practice of Pulse Plating*, ed. J. Puipe and F. Leaman, American Electroplates and Surface Finishers Society, (1986) p.1.

[Puippe 86-2] J. C. Puippe, Chap.3 in *Theory and Practice of Pulse Plating*, ed. J. Puipe and F. Leaman, American Electroplates and Surface Finishers Society, (1986) p.17.

[Puippe 86-3] J. C. Puippe, Chap.4 in *Theory and Practice of Pulse Plating*, ed. J. Puipe and F. Leaman, American Electroplates and Surface Finishers Society, (1986) p.41.

[Raub 37] E. Raub and K. Bihlmaier, *Galvanische Weissgolniederschlage, Mitt. Forschungsinst. Probieramts. Edelmetalle staatl. Hoheren Fachschule Schwab. Gmund*, **11** (1937) 59.

[Rinker 63] C. E. Rinker and R. Duva, *U.S. Pat., 3,104,212*(1963).

[Ruffoni 88] A. Ruffoni and D. Landolt, *Electrochimica Acta* **33**, (1988) 1281.

[Sanchez 97] H. Sanchez, P. Ozil, E. Chainet, B. Nguyen and Y. Meas, *J.*

Electrochem. Soc. **144**, (1997) 2004.

[Sasake 92] J. Sasaki, Y. Kaneyama, H. Honmon, M. Itoh and Y. Uji, Proc. *IEEE LEOS Annual Meeting*, (1992) p.260.

[Schlodder 86] F. R. Schlodder, H. H. Beyer and W. G. Zilske, *Gold 100, Proceedings of the Symposium on the Industrial Uses of Gold,* Johannesburg, SAIMM, **3**, (1986), p.21.

[Schloetter 32] M. Schloetter, *U.S. Pat., 1,857,644*(1932).

[Schloetter 36] M. Schloetter, *Ger. Pat., 608,268*(1936).

[Schlotter 85] I. M. Schlotter, in *'Analytical Handbook'*, edition 4, (May 1985), p.131.

[Schultz 98] H. Schultz and M. Pritzker, *J. Electrochem. Soc.*, **145**, (1998) 2033.

[Sel-Rex 71] Sel-Rex Corporation, *British Patent, 1,221,862*(1971).

[Smith 62] T. P. Smith, *U. S. Patent 3,057,789* (1962).

[Socha 75] J. Socha, S. Safarzynski and T. Zak, *J. Less-conmmon Met.* **43** (1975), p.283.

[Sonu 93] C. H. Sonu and T. J. Okeefe, *Plating and Surface Finishing*, (May 1993) p.141.

[Stanley 87] G. G. Stanley, Chapter 15, in '*The Extractive Metallurgy of Gold in South Africa*', Volume 2, The sough African Institute of Mining and Metallurgy, (1987), p.842.

[Sun 98] W. Sun and D. G. Ivey, *Spring meeting of Materials Research Society*, San Francisco, CA, (April 1998).

[Switzer 98] J. A. Switzer, *The electrochemical Society Interface*, (Spring 1998) 23.

[Tan 93] A. C. Tan, Chapter 8, 9 and 10, in '*Tin and Solder Plating in the Semiconductor Industry*', Chapman & Hall, (1993) p.197.

[Tan 96] Y. Tan and Y. C. Lee, *Proceeding of 1996 IEEE 46th Electronic Components and Technology Conference*, Orlando, Florida, (1996) p.27.

[Tanabe 83] Y. Tanabe, N. Hasegawa and M. Odaka, *J. Met. Soc. Jpn.* **34**,

(1983) 8.

[Traut 90] J. Traut, J. Wright and J. Williams, *Plat. and Surf. Fin.* **77**, (1990) 49.

[Verbrugge 85] M. W. Verbrugge and C. W. Tobias, *J. Electrochem. Soc.: Sci. & Technol.* **132**, (1985) 1298.

[Wada 91] O. Wada and T. Kumai, *Appl. Phys. Lett.* **58** (1991) 908.

[Wada 92] O. Wada, *Mat. Res. Soc. Symp. Proc.* **260** (1992) 713.

[Wagner 38] C. Wager and W. Traud, *Z. Elektrochem.* **44**, (1938) 391.

[Winand 91] R. Winand, *J. Appl. Electrochem.* **21**, (1991) 377.

[Winand 94] R. Winand, *Electrochimica Acta* **39**, (1994) 1091.

[Zakel 92-1] E. Zakel et al, *Proc. Elec. Comp. Technol. Conf.*, San Diego, (1992) p.360.

[Zakel 92-2] E. Zakel, J. Simon, G. Azdasht, and H. Teichl, *Soldering & Surface Mount Technology* **12**, (1992) 27.

[Zakel 94-1] E. Zakel, J. Gwiasda, J. Kloeser, J. Eldring, G. Engelmann, and H. Reichl, *Proceedings of the IEEE/CPMT International Electronics Manufacturing Technology (IEMT) Symposium VI*, IEEE Pidcataway, NJ, USA, (1994) p.177.

[Zakel 94-2] E. Zakel, G. Azdasht, and H. Reichl, *IEEE Transactions on Advanced Packaging*, Japan, (Nov, 1994).

[Zakel 95-1] E. Zakel and H. Reichl, Chapter 15, in '*Flip-Chip Technologies*', ed. J. Lau, McGraw Hill, (1995) p.415.

[Zakel 95-2] E. Zakel, R. Aschenbrenner, J. Gwiasda, G. Azdasht, A. Ostmann, J. Eldring, and H. Reichl, *Proceedings of the Technical Program: NEPCON WEST'95*, Vol.2, Reed Exhibition Co., Norwalk, CT, USA, (1995) p.909.

[Zuntini 74] F. Zuntini, G. Aliprandini, M. J. Gioria, A. Meyer and S. Losi, *U.S. Patent 3,787,463* (1974).

Appendix A

Selected X-ray Diffraction Data for Au, Au_5Sn, AuSn, $AuSn_2$, $AuSn_4$, Sn, InP, Si, Ti, and Mo

04-0784: QM:Star d: I:Diffractometer

Gold, syn
Au

Radiation : CuKa1 Lambda: 1.54056 Filter: Ni
Calibration: d-CutOff: I/Ic(RIR):
Ref: Swanson, Tatge.
Natl. Bur. Stand. (U.S.), Circ. 539, 1 33 (1953)

System: Cubic(Powder Diffraction) S.G.: Fm3m (225) Z= 4
Cell Parameters= 4.079 4.079 4.079 90.00 90.00 90.00 mp= 1062.4
Ref: Ibid.

Dx= 19.283 Dm= 19.300 Mwt= 196.97 Vol(RC)= 16.96 F(9)=128.5(.0078,9)

ea= nwB= .366 ey= Sign: 2V=
Ref: Winchell.
Elements of Optical Mineralogy 17

Yellow metallic. Sample purified at NBS laboratory and is about 99.997% Au. Spectrographic analysis in %: Si 0.001, Ca 0.001, Ag 0.001(?). Pattern at 26 C. Merck Index, 8th Ed., p. 503. Opaque mineral optical data on specimen from unspecified locality: RR#2Re=71.6, Disp.=16, VHN#1#0#0=53-58, Color values=.384, .391, 72.7, Ref.: IMA Commission on Ore Microscopy QDP.

9 Reflections. Radiation: CU_1.540598. Strong Lines: 2.36/X 2.04/5 1.23/4 1.44/3 0.94/2 0.83/2 0.91/2 1.18/1 1.02/1

#	d(A)	I(fix)	I(var)	h	k	l	2-Theta	Theta	1/(2d)
1>	2.3550	100	100	1	1	1	38.185	19.092	0.21231
2>	2.0390	52	60	2	0	0	44.393	22.196	0.24522
3>	1.4420	32	52	2	2	0	64.578	32.289	0.34674
4>	1.2300	36	69	3	1	1	77.549	38.775	0.40650
5>	1.1774	12	24	2	2	2	81.724	40.862	0.42466
6>	1.0196	6	13	4	0	0	98.137	49.068	0.49039
7>	0.9358	23	57	3	3	1	110.802	55.401	0.53430
8>	0.9120	22	56	4	2	0	115.264	57.632	0.54825
9>	0.8325	23	65	4	2	2	135.422	67.711	0.60060

Appendix A

Selected X-ray Diffraction Data for Au, Au_5Sn, AuSn, $AuSn_2$, $AuSn_4$, Sn, InP, Si, Ti, and Mo

31-0568: QM:Calculated Pattern d:Calculated I:Calculated

Gold Tin
Au5 Sn

Rhombohedral cell: a=5.6097, $GA=53.98.

Radiation : CuKa Lambda: 1.54188 Filter:
Calibration: d-CutOff: I/Ic(RIR): 11.496
Ref: Calvert, L., National Research Council of Canada, Ottawa, Canada.
ICDD Grant-in-Aid

System: Rhombohedral(Powder Diffraction) S.G.: R3 (146) Z= 3
Cell Parameters= 5.092 5.092 14.333 90.00 90.00 120.00 mp=
Ref: Osada, K. et al.
Trans. Jpn. Inst. Met., 15 256 (1974)
Dx= 17.081 Dm= Mwt= 1103.52 Vol(RC)= 107.28 F(2S)=24.4(.0106,97)

ea= nwB= ey= Sign: 2V=
Ref:

25 Reflections. Radiation: CU_1.540598. Strong Lines: 2.25/X 2.39/3 2.55/3 1.35/2 1.25/2 1.74/1 1.47/1 1.23/1 0.94/1

#	d(A)	I(fix)	I(var)	h	k	l	2-Theta	Theta	1/(2d)
1>	4.2110	2	1	1	0	1	21.080	10.540	0.11874
2>	3.7540	1	1	0	1	2	23.682	11.841	0.13319
3>	2.5461	25	22	1	1	0	35.221	17.610	0.19638
4>	2.3890	27	25	0	0	6	37.621	18.810	0.20929
5>	2.2468	100	100	1	1	3	40.100	20.050	0.22254
6>	1.7422	14	18	1	1	6	52.481	26.241	0.28699
7>	1.4701	14	21	3	0	0	63.199	31.599	0.34011
8>	1.3501	16	26	1	1	9	69.577	34.789	0.37034
9>	1.2729	2	3	2	2	0	74.480	37.240	0.39280
10>	1.2520	15	27	3	0	6	75.941	37.970	0.39936
11>	1.2301	11	20	2	2	3	77.542	38.771	0.40647
12>	1.1944	2	3	0	0	12	80.320	40.160	0.41862
13>	1.1234	3	6	2	2	6	86.579	43.290	0.44508
14>	1.0813	2	4	1	1	12	90.858	45.429	0.46241
15>	0.9944	6	13	2	2	9	101.544	50.772	0.50282
16>	0.9622	2	4	4	1	0	106.367	53.184	0.51964
17>	0.9434	11	26	4	1	3	109.475	54.737	0.53000
18>	0.9270	7	17	3	0	12	112.395	56.197	0.53937
19>	0.8945	5	12	1	1	15	118.892	59.446	0.55897
20>	0.8924	6	15	4	1	6	119.350	59.675	0.56029
21>	0.8710	2	5	2	2	12	124.352	62.176	0.57405
22>	0.8487	3	8	3	3	0	130.358	65.179	0.58914
23>	0:8236	9	24	4	1	9	138.548	69.274	0.60709
24>	0.7996	6	16	3	3	6	148.882	74.441	0.62531
25>	0.7963	1	2	0	0	18	150.636	75.318	0.62790

Appendix A

Selected X-ray Diffraction Data for Au, Au_5Sn, AuSn, $AuSn_2$, $AuSn_4$, Sn, InP, Si, Ti, and Mo

08-0463: QM:Indexed d: I:Diffractometer

Gold Tin
Au Sn

Radiation : CuKa1 Lambda: 1.5405 Filter: Ni
Calibration: d-CutOff: I/Ic(RIR):
Ref: Natl. Bur. Stand. (U.S.), Circ. 539, 7 19 (1957)

System: Hexagonal(Powder Diffraction) S.G.: P63/mmc (194) Z= 2
Cell Parameters= 4.323 4.323 5.517 90.00 90.00 120.00 mp=
Ref: Ibid.

Dx= 11.741 Dm= Mwt= 315.66 Vol(RC)= 89.29 F(30)=23.7(0.035,36)

ea= nwB= ey= Sign: 2V=
Ref:

Gray metallic. Sample prepared at the NBS. Spectroscopic analysis showed <0.1% Pd; <0.01% Cu; <0.001% Ag, Fe, Si. Pattern made at 25 C.

40 Reflections. Radiation: CU_1.540598. Strong Lines: 2.22/X 2.16/7 3.74/5 3.09/5 1.55/3 1.26/2 1.16/1 1.77/1 1.65/1

#	d(A)	I(fix)	I(var)	h	k	l	2-Theta	Theta	1/(2d)
1>	3.7400	50	29	1	0	0	23.772	11.886	0.13369
2>	3.0900	45	32	1	0	1	28.871	14.435	0.16181
3>	2.2220	100	100	1	0	2	40.567	20.284	0.22502
4>	2.1610	65	66	1	1	0	41.765	20.883	0.23137
5>	1.8700	8	9	2	0	0	48.652	24.326	0.26738
6>	1.7720	10	12	2	0	1	51.533	25.767	0.28217
7>	1.7020	4	5	1	1	2	53.819	26.910	0.29377
8>	1.6520	10	13	1	0	3	55.587	27.793	0.30266
9>	1.5490	25	35	2	0	2	59.641	29.821	0.32279
10>	1.4150	10	15	2	1	0	65.965	32.982	0.35336
11>	1.3705	8	13	2	1	1	68.396	34.198	0.36483
12>	1.3120	4	6	2	0	3	71.906	35.953	0.38110
13>	1.2950	6	10	1	0	4	73.000	36.500	0.38610
14>	1.2592	20	35	2	1	2	75.430	37.715	0.39708
15>	1.2475	8	14	3	0	0	76.264	38.132	0.40080
16>	1.1637	14	26	1	1	4	82.896	41.448	0.42966
17>	1.1372	1	2	3	0	2	85.276	42.638	0.43968
18>	1.1220	1	2	2	1	3	86.714	43.357	0.44563
19>	1.1112	2	4	2	0	4	87.770	43.885	0.44996
20>	1.0808	4	8	2	2	0	90.912	45.456	0.46262
21>	1.0594	1	2	1	0	5	93.289	46.645	0.47197
22>	1.0382	1	2	3	1	0	95.797	47.898	0.48160
23>	1.0204	2	4	3	1	1	98.033	49.017	0.49000
24>	1.0063	2	4	2	2	2	99.899	49.949	0.49687
25>	0.9882	2	4	2	1	4	102.429	51.215	0.50597
26>	0.9720	6	13	3	1	2	104.837	52.419	0.51440
27>	0.9509	1	2	2	0	5	108.206	54.103	0.52582
28>	0.9361	1	2	4	0	0	110.748	55.374	0.53413
29>	0.9258	4	9	3	0	4	112.617	56.308	0.54007
30>	0.9042	2	5	3	1	3	116.841	58.420	0.55297
31>	0.8938	6	15	1	0	6	119.044	59.522	0.55941
32>	0.8863	4	10	4	0	2	120.713	60.356	0.56414
33>	0.8706	2	5	2	1	5	124.452	62.226	0.57432
34>	0.8587	2	5	3	2	0	127.547	63.773	0.58228
35>	0.8509	8	20	2	2	4	129.721	64.860	0.58761
36>	0.8486	4	10	3	2	1	130.387	65.193	0.58921
37>	0.8342	2	5	4	0	3	134.856	67.428	0.59938
38>	0.8298	2	5	3	1	4	136.341	68.171	0.60255
39>	0.8259	4	10	2	0	6	137.712	68.856	0.60540
40>	0.8200	8	21	3	2	2	139.898	69.949	0.60976

Appendix A

Selected X-ray Diffraction Data for Au, Au_5Sn, AuSn, $AuSn_2$, $AuSn_4$, Sn, InP, Si, Ti, and Mo

20-0440: ON:Calculated Pattern d:Calculated I:Calculated

Gold Tin
Au Sn2

Radiation : CuKa1 Lambda: 1.5405 Filter:
Calibration: d-CutOff: I/Ic(RIR):
Ref: Calvert, Larson, National Research Council of Canada, Ottawa, Canada.
ICDD Grant-in-Aid (1976)

System: Orthorhombic(Powder Diffraction) S.G.: Pbca (61) Z= 8
Cell Parameters= 7.037 11.788 6.908 90.00 90.00 90.00 mp=
Ref: Schubert.
Z. Metallkd., 50 146 (1959)
Dx= 10.069 Dm= Mwt= 434.35 Vol(RC)= 573.03 F(30)=999.9(.0007,35)

ea= nwB= ey= Sign: 2V=
Ref:

59 Reflections. Radiation: CU_1.540598. Strong Lines: 4.55/X 2.06/X 2.77/7 2.13/7 3.10/7 2.95/6 2.71/5 2.62/5 2.05/5

#	d(A)	I(fix)	I(var)	h	k	l	2-Theta	Theta	1/(2d)	#	d(A)	I(fix)	I(var)	h	k	l	2-Theta	Theta	1/(2d)
1>	4.5480	100	45	1	1	1	19.502	9.751	0.10994	31>	1.9647	6	6	0	0	6	46.167	23.083	0.25449
2>	4.4860	1	1	1	0	2	19.784	9.892	0.11151	32>	1.9586	1	1	0	2	5	46.319	23.159	0.25526
3>	3.7810	40	22	1	1	2	23.510	11.755	0.13226	33>	1.9336	8	8	1	3	3	46.953	23.477	0.25859
4>	3.5190	1	1	0	2	0	25.289	12.644	0.14209	34>	1.9147	7	7	2	3	1	47.445	23.723	0.26114
5>	3.4540	30	18	2	0	0	25.773	12.886	0.14476	35>	1.9119	25	27	3	1	3	47.519	23.759	0.26152
6>	3.3720	9	5	0	2	1	26.410	13.205	0.14828	36>	1.8907	4	4	2	2	4	48.085	24.043	0.26445
7>	3.1010	65	43	2	1	0	28.766	14.383	0.16124	37>	1.8897	1	1	1	0	6	48.112	24.056	0.26459
8>	3.0210	40	27	0	2	2	29.545	14.772	0.16551	38>	1.8843	3	3	1	2	5	48.259	24.129	0.26535
9>	2.9986	40	27	2	1	1	29.771	14.885	0.16674	39>	1.8767	1	1	2	1	5	48.467	24.233	0.26643
10>	2.9800	1	1	2	0	2	29.961	14.980	0.16779	40>	1.8432	14	15	2	3	2	49.406	24.703	0.27127
11>	2.9470	55	38	0	0	4	30.304	15.152	0.16966	41>	1.8314	5	5	3	2	2	49.746	24.873	0.27302
12>	2.7680	70	52	1	2	2	32.316	16.158	0.18064	42>	1.8251	6	6	1	1	6	49.929	24.965	0.27396
13>	2.7441	4	3	2	1	2	32.605	16.303	0.18221	43>	1.8145	3	3	3	0	4	50.241	25.121	0.27556
14>	2.7106	50	38	1	0	4	33.020	16.510	0.18446	44>	1.7737	3	3	1	3	4	51.480	25.740	0.28190
15>	2.6212	50	39	0	2	3	34.180	17.090	0.19075	45>	1.7570	20	23	3	1	4	52.006	26.003	0.28458
16>	2.5295	4	3	1	1	4	35.459	17.730	0.19767	46>	1.7400	1	1	0	4	1	52.553	26.276	0.28736
17>	2.4648	9	7	2	2	0	36.422	18.211	0.20286	47>	1.7154	9	11	0	2	6	53.365	26.683	0.29148
18>	2.4507	3	2	1	2	3	36.639	18.320	0.20402	48>	1.7077	1	1	2	0	6	53.625	26.813	0.29279
19>	2.4361	10	8	2	1	3	36.858	18.449	0.20541	49>	1.7037	2	2	2	2	5	53.761	26.881	0.29348
20>	2.4127	30	25	2	2	1	37.237	18.619	0.20724	50>	1.6772	1	1	4	1	0	54.681	27.340	0.29812
21>	2.2740	2	1	2	2	2	39.600	19.800	0.21988	51>	1.6648	2	2	1	2	6	55.123	27.561	0.30034
22>	2.2419	20	18	2	0	4	40.192	20.096	0.22303	52>	1.6605	1	1	4	1	1	55.278	27.639	0.30111
23>	2.1827	10	9	1	3	1	41.331	20.665	0.22907	53>	1.6596	6	7	2	1	6	55.310	27.655	0.30128
24>	2.1517	35	33	3	1	1	41.954	20.977	0.23237	54>	1.6573	2	2	4	0	2	55.393	27.697	0.30170
25>	2.1448	3	3	3	0	2	42.096	21.048	0.23312	55>	1.6377	3	3	1	4	2	56.115	28.057	0.30531
26>	2.1361	6	5	2	1	4	42.275	21.138	0.23407	56>	1.6275	1	1	3	3	1	56.498	28.249	0.30722
27>	2.1269	70	68	1	1	5	42.467	21.234	0.23508	57>	1.6207	1	1	2	3	4	56.756	28.378	0.30851
28>	2.0880	35	34	2	2	3	43.298	21.649	0.23946	58>	1.6132	1	1	4	1	2	57.044	28.522	0.30994
29>	2.0784	100	100	1	3	2	43.508	21.754	0.24057	59>	1.6127	1	1	3	2	4	57.063	28.532	0.31004
30>	2.0516	50	50	3	1	2	44.106	22.053	0.24371										

Appendix A

Selected X-ray Diffraction Data for Au, Au_5Sn, AuSn, $AuSn_2$, $AuSn_4$, Sn, InP, Si, Ti, and Mo

20-0441: QM:Calculated Pattern d:Calculated I:Calculated

Gold Tin
Au Sn4

Radiation : CuKa1 Lambda: 1.5405 Filter:
Calibration: d-CutOff: I/Ic(RIR):
Ref: Calvert, Larson, National Research Council of Canada, Ottawa, Canada.
ICDD Grant-in-Aid (1976)

System: Orthorhombic(Powder Diffraction) S.G.: Cc2a (41) Z= 4
Cell Parameters= 6.484 11.599 6.446 90.00 90.00 90.00 mp=
Ref: Schubert, Roeler.
Z. Metallkd., 41 298 (1950)
Dx= 9.203 Dm= Mwt= 671.73 Vol(RC)= 242.40 F(30)=999.9(.0005,45)

ea= nwB= ey= Sign: 2V=
Ref:

59 Reflections. Radiation: CU_1.540598. Strong Lines: 2.59/X 2.95/8 5.80/7 2.80/7 2.16/5 4.25/4 2.02/4 2.01/4 2.31/4

#	d(A)	I(fix)	I(var)	h	k	l	2-Theta	Theta	1/(2d)
1>	5.8000	65	29	0	0	2	15.264	7.632	0.08621
2>	4.2510	40	24	1	1	1	20.870	10.435	0.11756
3>	3.2420	3	2	0	2	0	27.490	13.745	0.15423
4>	3.2230	3	2	2	0	0	27.655	13.828	0.15513
5>	2.9521	80	70	1	1	3	30.251	15.125	0.16937
6>	2.8997	25	22	0	0	4	30.811	15.405	0.17243
7>	2.8298	18	16	0	2	2	31.592	15.796	0.17669
8>	2.8172	18	16	2	0	2	31.737	15.868	0.17748
9>	2.8007	65	60	2	1	1	31.929	15.964	0.17853
10>	2.5912	100	100	1	2	3	34.588	17.294	0.19296
11>	2.3128	35	39	2	1	3	38.909	19.455	0.21619
12>	2.2857	30	34	2	2	0	39.389	19.695	0.21875
13>	2.1613	45	54	0	2	4	41.759	20.880	0.23134
14>	2.1557	45	54	2	0	4	41.873	20.936	0.23194
15>	2.1265	16	19	2	2	2	42.475	21.238	0.23513
16>	2.0687	25	31	1	1	5	43.722	21.861	0.24170
17>	2.0180	40	51	1	3	1	44.880	22.440	0.24777
18>	2.0088	40	51	3	1	1	45.097	22.548	0.24890
19>	1.9332	3	4	0	0	6	46.964	23.482	0.25864
20>	1.8081	14	20	2	1	5	50.431	25.216	0.27653
21>	1.6604	3	4	0	2	6	55.281	27.641	0.30113
22>	1.6578	3	4	2	0	6	55.375	27.688	0.30160
23>	1.6079	18	29	1	2	6	57.250	28.625	0.31096
24>	1.5612	2	3	0	4	2	59.129	29.564	0.32027
25>	1.5578	2	3	1	1	7	59.271	29.635	0.32097
26>	1.5527	2	3	4	0	2	59.485	29.743	0.32202
27>	1.5499	10	16	4	1	1	59.603	29.802	0.32260
28>	1.5173	18	30	1	4	2	61.018	30.509	0.32953
29>	1.5108	2	3	3	3	1	61.309	30.655	0.33095
30>	1.4760	4	7	2	2	6	62.917	31.459	0.33875
31>	1.4499	20	35	0	0	8	64.184	32.092	0.34485
32>	1.4482	4	7	2	4	0	64.268	32.134	0.34526
33>	1.4431	4	7	4	2	0	64.523	32.261	0.34648
34>	1.4370	6	10	2	1	7	64.830	32.415	0.34795
35>	1.4177	25	45	3	3	3	65.823	32.912	0.35268
36>	1.4149	6	11	0	4	4	65.970	32.985	0.35338
37>	1.4086	6	11	4	0	4	66.303	33.151	0.35496
38>	1.4050	3	5	2	4	2	66.495	33.247	0.35587
39>	1.4004	3	5	4	2	2	66.742	33.371	0.35704
40>	1.2968	5	10	4	1	5	72.883	36.441	0.38556
41>	1.2956	1	2	2	4	4	72.961	36.481	0.38592
42>	1.2919	1	2	4	2	4	73.204	36.602	0.38703
43>	1.2885	7	14	1	3	7	73.429	36.714	0.38805
44>	1.2861	7	14	3	1	7	73.588	36.794	0.38877
45>	1.2736	16	32	3	3	5	74.432	37.216	0.39259
46>	1.2421	1	2	0	4	6	76.655	38.328	0.40256
47>	1.2404	1	2	1	1	9	76.780	38.390	0.40310
48>	1.2378	1	2	4	0	6	76.970	38.485	0.40394
49>	1.2243	6	12	2	2	8	77.979	38.989	0.40840
50>	1.2197	8	17	1	4	6	78.329	39.164	0.40994
51>	1.2077	4	8	1	5	3	79.259	39.630	0.41401
52>	1.2018	4	8	5	1	3	79.726	39.863	0.41604
53>	1.1966	2	4	2	5	1	80.143	40.071	0.41785
54>	1.1768	3	6	2	1	9	81.776	40.887	0.42488
55>	1.1732	4	8	5	2	2	82.079	41.040	0.42618
56>	1.1590	1	2	2	4	6	83.307	41.653	0.43141
57>	1.1564	1	2	4	2	6	83.536	41.768	0.43238
58>	1.1487	2	4	2	5	3	84.224	42.112	0.43527
59>	1.1428	1	2	4	4	0	84.760	42.380	0.43752

Appendix A

Selected X-ray Diffraction Data for Au, Au_5Sn, AuSn, $AuSn_2$, $AuSn_4$, Sn, InP, Si, Ti, and Mo

18-1380: QM:Star d: I:

Tin
Sn

Pattern at 39 kbar, 308-320 C.

Radiation : CuKa Lambda: 1.5418 Filter:
Calibration: d-CutOff: I/Ic(RIR):
Ref: Barnett et al.
Science, 141 1041 (1963)

System: Tetragonal (Powder Diffraction) S.G.: I4/mmm (139) Z= 2
Cell Parameters= 3.811 3.811 3.483 90.00 90.00 90.00 mp=
Ref: Ibid.

Dx= 7.792 Dm= Mwt= 118.69 Vol(RC)= 25.29 F(7)=89.9(.0111,7)

ea= nwB= ey= Sign: 2V=
Ref:

7 Reflections. Radiation: CU_1.540598. Strong Lines: 2.57/X 2.70/5 1.91/4 1.53/3 1.74/1 1.46/1 1.35/1 0.00/1 0.00/1

#	d(A)	I(fix)	I(var)	h	k	l	2-Theta	Theta	1/(2d)
1>	2.6950	50	47	1	1	0	33.216	16.608	0.18553
2>	2.5710	100	100	1	0	1	34.868	17.434	0.19448
3>	1.9060	40	54	2	0	0	47.675	23.838	0.26233
4>	1.7410	10	14	0	0	2	52.520	26.260	0.28719
5>	1.5310	30	50	2	1	1	60.415	30.208	0.32658
6>	1.4630	5	8	1	1	2	63.541	31.771	0.34176
7>	1.3470	5	9	2	2	0	69.760	34.880	0.37120

Appendix A

Selected X-ray Diffraction Data for Au, Au_5Sn, AuSn, $AuSn_2$, $AuSn_4$, Sn, InP, Si, Ti, and Mo

04-0673: QM:Star d: I:Diffractometer

Tin, syn
Sn

Radiation : CuKa1 Lambda: 1.54056 Filter: Ni
Calibration: d-CutOff: I/Ic(RIR): 1.966
Ref: Swanson, Tatge.
Natl. Bur. Stand. (U.S.), Circ. 539, 1 24 (1953)

System: Tetragonal(Powder Diffraction) S.G.: I41/amd (141) Z= 4
Cell Parameters= 5.831 5.831 3.182 90.00 90.00 90.00 mp= 231.8°
Ref: Ibid.

Dx= 7.287 Dm= Mwt= 118.69 Vol(RC)= 54.09 F(29)=70.3(.0125,33)

ea= nwB= ey= Sign: 2V=
Ref:

Space group given by Mark, Polanyi, \ITZ. Phys.\RG, \BP18\RG 75-96 (1925). Sample was furnished by Johnson Matthey Company, Ltd. and annealed 12 hours at 160 C. Analysis (%): Pb 0.0012, Sb 0.001, Fe 0.00027, Cu 0.0002, As 0.0002, Bi 0.00012, S 0.0003, Sn 99.997 (by difference), other form $GA-Sn (cubic). Pattern at 26 C. Merck Index, 8th Ed., p. 1053. Silver-white. Color from \ITDana's System of Mineralogy, 7th Ed.\RG, 485.

29 Reflections. Radiation: CU_1.540598. Strong Lines: 2.92/X 2.79/9 2.02/7 2.06/3 1.48/2 1.44/2 1.21/2 1.66/2 1.30/2

#	d(A)	I(fix)	I(var)	h	k	l	2-Theta	Theta	1/(2d)
1>	2.9150	100	93	2	0	0	30.645	15.323	0.17153
2>	2.7930	90	87	1	0	1	32.019	16.009	0.17902
3>	2.0620	34	45	2	2	0	43.872	21.936	0.24248
4>	2.0170	74	100	2	1	1	44.903	22.452	0.24789
5>	1.6590	17	28	3	0	1	55.332	27.666	0.30139
6>	1.4840	23	42	1	1	2	62.540	31.270	0.33693
7>	1.4580	13	24	4	0	0	63.785	31.892	0.34294
8>	1.4420	20	37	3	2	1	64.578	32.289	0.34674
9>	1.3040	15	31	4	2	0	72.416	36.208	0.38344
10>	1.2920	15	31	4	1	1	73.197	36.599	0.38700
11>	1.2050	20	45	3	1	2	79.472	39.736	0.41494
12>	1.0950	13	32	4	3	1	89.412	44.706	0.45662
13>	1.0434	3	7	1	0	3	95.167	47.583	0.47920
14>	1.0401	5	13	3	3	2	95.565	47.783	0.48072
15>	1.0309	2	5	4	4	0	96.699	48.349	0.48501
16>	1.0252	5	13	5	2	1	97.417	48.709	0.48771
17>	0.9824	5	13	2	1	3	103.275	51.637	0.50896
18>	0.9718	2	5	6	0	0	104.868	52.434	0.51451
19>	0.9310	3	8	3	0	3	111.663	55.831	0.53706
20>	0.9286	13	38	5	1	2	112.100	56.050	0.53844
21>	0.9219	5	14	6	2	0	113.348	56.674	0.54236
22>	0.9178	5	14	6	1	1	114.130	57.065	0.54478
23>	0.8868	4	12	3	2	3	120.599	60.300	0.56383
24>	0.8755	2	6	5	4	1	123.246	61.623	0.57110
25>	0.8485	4	12	4	1	3	130.416	65.208	0.58928
26>	0.8466	10	32	5	3	2	130.976	65.488	0.59060
27>	0.8386	4	13	6	3	1	133.431	66.716	0.59623
28>	0.8086	6	20	6	4	0	144.589	72.295	0.61835
29>	0.8058	3	10	7	0	1	145.859	72.929	0.62050

Appendix A

Selected X-ray Diffraction Data for Au, Au_5Sn, AuSn, $AuSn_2$, $AuSn_4$, Sn, InP, Si, Ti, and Mo

05-0390: QM:Star d: I:Diffractometer

Tin
Sn

Radiation : CuKa1 Lambda: 1.5405 Filter: Ni
Calibration: d-CutOff: I/Ic(RIR):
Ref: Swanson, Fuyat.
Natl. Bur. Stand. (U.S.), Circ. 539, 2 12 (1953)

System: Cubic(Powder Diffraction) S.G.: Fd3m (227) Z= 8
Cell Parameters= 6.489 6.489 6.489 90.00 90.00 90.00 mp=
Ref: Ibid.

Dx= 5.771 Dm= Mwt= 118.69 Vol(RC)= 68.31 F(15)=53.6(.0156,18)

ea= nwB= ey= Sign: 2V=
Ref:

Gray. Sample was made from NBS Melting Point Standard 42D by seeding it with small quantity of $GA-Sn. Spectroscopic analysis: <0.01% Cu, Fe, Pb. Sample was refrigerated at 10 C until just before use. X-ray pattern at 25 C. Merck Index, 8th Ed., p. 1053.

15 Reflections. Radiation: CU_1.540598. Strong Lines: 3.75/X 2.29/8 1.96/5 1.33/2 1.49/2 0.87/1 1.62/1 0.85/1 1.25/1

#	d(A)	I(fix)	I(var)	h	k	l	2-Theta	Theta	1/(2d)
1>	3.7510	100	73	1	1	1	23.701	11.850	0.13330
2>	2.2940	83	100	2	2	0	39.241	19.620	0.21796
3>	1.9560	53	74	3	1	1	46.384	23.192	0.25562
4>	1.6220	12	20	4	0	0	56.707	28.353	0.30826
5>	1.4890	20	37	3	3	1	62.306	31.153	0.33580
6>	1.3250	21	43	4	2	2	71.092	35.546	0.37736
7>	1.2490	11	24	5	1	1	76.156	38.078	0.40032
8>	1.1470	6	14	4	4	0	84.378	42.189	0.43592
9>	1.0968	10	25	5	3	1	89.226	44.613	0.45587
10>	1.0260	9	24	6	2	0	97.316	48.658	0.48733
11>	0.9895	4	11	5	3	3	102.242	51.121	0.50531
12>	0.9365	3	8	4	4	4	110.678	55.339	0.53390
13>	0.9087	7	21	5	5	1	115.923	57.962	0.55024
14>	0.8671	13	41	6	4	2	125.336	62.668	0.57663
15>	0.8450	12	39	7	3	1	131.454	65.727	0.59172

Appendix A

Selected X-ray Diffraction Data for Au, Au_5Sn, AuSn, $AuSn_2$, $AuSn_4$, Sn, InP, Si, Ti, and Mo

19-1365: QM:Indexed d: I:

Tin
Sn

Pattern taken at 98 kbar.

Radiation : CuKa Lambda: 1.5405 Filter:
Calibration: d-CutOff: I/Ic(RIR):
Ref: Barnett et al.
J. Appl. Phys., 37 875 (1966)

System: Tetragonal(Powder Diffraction) S.G.: I4/mmm (139) Z= 2
Cell Parameters= 3.700 3.700 3.370 90.00 90.00 90.00 mp=
Ref: Ibid.

Dx= 8.544 Dm= Mwt= 118.69 Vol(RC)= 23.07 F(8)=17.6(0.057,8)

ea= nwB= ey= Sign: 2V=
Ref:

8 Reflections. Radiation: CU_1.540598. Strong Lines: 2.49/X 2.62/6 1.48/4 1.85/2 1.42/2 1.31/1 1.24/1 1.68/1 0.00/1

#	d(A)	I(fix)	I(var)	h	k	l	2-Theta	Theta	1/(2d)	#	d(A)	I(fix)	I(var)	h	k	l	2-Theta	Theta	1/(2d)
1>	2.6160	55	52	1	1	0	34.250	17.125	0.19113	5>	1.4840	35	58	2	1	1	62.540	31.270	0.33693
2>	2.4920	100	100	1	0	1	36.011	18.006	0.20064	6>	1.4160	15	26	1	1	2	65.912	32.956	0.35311
3>	1.8490	20	27	2	0	0	49.241	24.620	0.27042	7>	1.3090	10	19	2	2	0	72.096	36.048	0.38197
4>	1.6810	5	7	0	0	2	54.547	27.274	0.29744	8>	1.2440	10	20	2	0	2	76.517	38.259	0.40193

Appendix A

Selected X-ray Diffraction Data for Au, Au_5Sn, AuSn, $AuSn_2$, $AuSn_4$, Sn, InP, Si, Ti, and Mo

32-0452: QM:Star d: I:Diffractometer

Indium Phosphide
In P

Radiation : CuKa1 Lambda: 1.5406 Filter: Ni
Calibration: Internal(Si) d-CutOff: I/Ic(RIR):
Ref: Gong, P., Polytechnic Institute of New York, Brooklyn, New York, USA.
ICDD Grant-in-Aid (1981)

System: Cubic(Powder Diffraction) S.G.: F-43m (216) Z= 4
Cell Parameters= 5.869 5.869 5.869 90.00 90.00 90.00 mp=
Ref: Ibid.

Dx= 4.790 Dm= Mwt= 145.79 Vol(RC)= 50.54 F(19)=54.7(.0183,19)

ea= nwB= ey= Sign: 2V=
Ref:

Black. To replace 13-232.

19 Reflections. Radiation: CU_1.540598. Strong Lines: 3.39/X 2.07/5 2.94/4 1.77/4 1.13/2 0.99/2 0.82/2 1.69/1 1.47/1

#	d(A)	I(fix)	I(var)	h	k	l	2-Theta	Theta	1/(2d)
1>	3.3880	100	100	1	1	1	26.283	13.142	0.14758
2>	2.9350	35	40	2	0	0	30.431	15.216	0.17036
3>	2.0740	50	81	2	2	0	43.605	21.802	0.24108
4>	1.7692	35	67	3	1	1	51.621	25.810	0.28261
5>	1.6941	10	20	2	2	2	54.091	27.045	0.29514
6>	1.4668	10	23	4	0	0	63.358	31.679	0.34088
7>	1.3463	10	25	3	3	1	69.802	34.901	0.37139
8>	1.3122	8	20	4	2	0	71.893	35.946	0.38104
9>	1.1979	10	28	4	2	2	80.038	40.019	0.41740
10>	1.1294	15	45	5	1	1	86.007	43.003	0.44271
11>	1.0373	6	19	4	4	0	95.907	47.953	0.48202
12>	0.9922	15	51	5	3	1	101.856	50.928	0.50393
13>	0.9783	6	20	6	0	0	103.884	51.942	0.51109
14>	0.9279	8	29	6	2	0	112.229	56.114	0.53885
15>	0.8951	8	30	5	3	3	118.762	59.381	0.55860
16>	0.8849	2	7	6	2	2	121.032	60.516	0.56504
17>	0.8471	3	12	4	4	4	130.828	65.414	0.59025
18>	0.8220	15	61	5	5	1	139.141	69.571	0.60827
19>	0.8140	10	41	6	4	0	142.281	71.140	0.61425

Appendix A

Selected X-ray Diffraction Data for Au, Au_5Sn, AuSn, $AuSn_2$, $AuSn_4$, Sn, InP, Si, Ti, and Mo

27-1402: QM:Star d:Diffractometer I:Diffractometer

Silicon, syn [NR]
Si

Radiation : CuKa1 Lambda: 1.5405981 Filter:
Calibration: Internal(W) d-CutOff: I/Ic(RIR): 4.70
Ref: Natl. Bur. Stand. (U.S.) Monogr. 25, 13 35 (1976)

System: Cubic(Powder Diffraction) S.G.: Fd3m (227) Z= 8
Cell Parameters= 5.431 5.431 5.431 90.00 90.00 90.00 mp=
Ref: Ibid.

Dx= 2.329 Dm= Mwt= 28.09 Vol(RC)= 40.05 F(11)=408.4(.0021,13)

ea= nwB= ey= Sign: 2V=
Ref:

Pattern at 25(1) C. This sample is NBS Standard Reference Material No. 640. Reflections calculated from precision measurement of a#0. a#0 uncorrected for refraction. To replace 5-565 and 26-1481. Gray

11 Reflections. Radiation: CU_1.540598. Strong Lines: 3.14/X 1.92/6 1.64/3 1.11/1 1.25/1 0.86/1 0.92/1 1.36/1 1.05/1

#	d(A)	I(fix)	I(var)	h	k	l	2-Theta	Theta	1/(2d)
1>	3.1355	100	100	1	1	1	28.443	14.221	0.15946
2>	1.9201	55	89	2	2	0	47.303	23.652	0.26040
3>	1.6375	30	57	3	1	1	56.122	28.061	0.30534
4>	1.3577	6	13	4	0	0	69.132	34.566	0.36827
5>	1.2459	11	27	3	3	1	76.379	38.190	0.40132
6>	1.1086	12	34	4	2	2	88.029	44.014	0.45102
7>	1.0452	6	18	5	1	1	94.951	47.475	0.47838
8>	0.9600	3	9	4	4	0	106.719	53.359	0.52083
9>	0.9180	7	23	5	3	1	114.092	57.046	0.54466
10>	0.8587	8	29	6	2	0	127.547	63.773	0.58228
11>	0.8282	3	11	5	3	3	136.897	68.449	0.60372

Appendix A

Selected X-ray Diffraction Data for Au, Au_5Sn, AuSn, $AuSn_2$, $AuSn_4$, Sn, InP, Si, Ti, and Mo

05-0682: QM:Indexed d: I:Diffractometer

Titanium
Ti

Radiation : CuKa1 Lambda: 1.5405 Filter: Ni
Calibration: d-CutOff: I/Ic(RIR): 1.820
Ref: Swanson, Fuyat.
Natl. Bur. Stand. (U.S.), Circ. 539, 3 4 (1954)

System: Hexagonal(Powder Diffraction) S.G.: P63/mmc (194) Z= 2
Cell Parameters= 2.950 2.950 4.686 90.00 90.00 120.00 mp=
Ref: Ibid.

Dx= 4.504 Dm= Mwt= 47.90 Vol(RC)= 35.32 F(21)=20.4(0.045,23)

ea= nwB= ey= Sign: 2V=
Ref:

Dark gray. Sample from New Jersey Zinc Company. Prepared by the iodide process. Spectroscopic analysis: 0.02% Al; 0.012% Fe, Mn; 0.006% Mo; 0.004% N; 0.0025% Mg; 0.002% Cu. X-ray pattern at 25 C. Merck Index, 8th Ed., p. 1054.

21 Reflections. Radiation: CU_1.540598. Strong Lines: 2.24/X 2.56/3 2.34/3 1.73/2 1.48/2 1.33/2 1.25/2 1.23/1 0.82/1

#	d(A)	I(fix)	I(var)	h	k	l	2-Theta	Theta	1/(2d)
1>	2.5570	30	26	1	0	0	35.066	17.533	0.19554
2>	2.3420	26	25	0	0	2	38.405	19.202	0.21349
3>	2.2440	100	100	1	0	1	40.153	20.076	0.22282
4>	1.7260	19	24	1	0	2	53.012	26.506	0.28969
5>	1.4750	17	25	1	1	0	62.965	31.482	0.33898
6>	1.3320	16	27	1	0	3	70.662	35.331	0.37538
7>	1.2760	2	3	2	0	0	74.268	37.134	0.39185
8>	1.2470	16	28	1	1	2	76.300	38.150	0.40096
9>	1.2330	13	23	2	0	1	77.326	38.663	0.40551
10>	1.1708	2	3	0	0	4	82.284	41.142	0.42706
11>	1.1220	2	4	2	0	2	86.714	43.357	0.44563
12>	1.0653	3	6	1	0	4	92.619	46.310	0.46935
13>	0.9895	6	13	2	0	3	102.242	51.121	0.50531
14>	0.9458	11	26	2	1	1	109.064	54.532	0.52865
15>	0.9175	10	24	1	1	4	114.188	57.094	0.54496
16>	0.8927	4	10	2	1	2	119.285	59.642	0.56010
17>	0.8796	4	10	1	0	5	122.265	61.132	0.56844
18>	0.8634	2	5	2	0	4	126.294	63.147	0.57911
19>	0.8514	4	10	3	0	0	129.578	64.789	0.58727
20>	0.8211	12	32	2	1	3	139.480	69.740	0.60894
21>	0.8005	9	25	3	0	2	148.423	74.211	0.62461

Appendix A

Selected X-ray Diffraction Data for Au, Au_5Sn, AuSn, $AuSn_2$, $AuSn_4$, Sn, InP, Si, Ti, and Mo

42-1120: QM:Star d:Diffractometer I:Diffractometer

Molybdenum Mo	Sample from Johnson Matthey, AESAR 10030, Lot G11A06. Black. To replace 4-809.
Radiation : CuKa1 Lambda: 1.5405988 Filter: Graph Calibration: Internal(Al2O3) d-CutOff: 3.0 I/Ic(RIR): 7.379 Ref: Schreiner, W., Intelligent Controls Inc., Amawalk, New York, USA. ICDD Grant-in-Aid (1991)	
System: Cubic() S.G.: Im3m (229) Z= 2 Cell Parameters= 3.147 3.147 3.147 90.00 90.00 90.00 mp= Ref: Swanson, Tatge. Natl. Bur. Stand. (U.S.), Circ. 539, 1 20 (1953) Dx= 10.221 Dm= Mwt= 95.94 Vol(RC)= 15.59 F(7)=79.7(.0126,7)	
ea= nwB= ey= Sign: 2V= Ref:	

7 Reflections. Radiation: CU_1.540598. Strong Lines: 2.22/X 1.28/3 1.57/2 0.84/2 1.00/1 1.11/1 0.91/1 0.00/1 0.00/1

#	d(A)	I(fix)	I(var)	h	k	l	2-Theta	Theta	1/(2d)
1>	2.2247	100	100	1	1	0	40.516	20.258	0.22475
2>	1.5738	16	22	2	0	0	58.609	29.305	0.31770
3>	1.2847	31	53	2	1	1	73.684	36.842	0.38921
4>	1.1129	9	18	2	2	0	87.598	43.799	0.44926
5>	0.9953	14	31	3	1	0	101.413	50.706	0.50234
6>	0.9085	3	7	2	2	2	115.969	57.984	0.55037
7>	0.8411	24	63	3	2	1	132.647	66.323	0.59446